ITT ELECTRON TUBE DIVISION

A DIVISION OF INTERNATIONAL TELEPHONE AND TELEGRAPH CORPORATION

FINAL REPORT

DEVELOPMENT OF ELECTRONICALLY TUNABLE

CONVERTERS IN THE MILLIMETER WAVE RANGE

CONTRACT NASw-790

for period

July 16, 1963 - November 16, 1964

Prepared for

Lunar and Planetary Programs
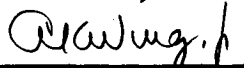Office of Space Sciences
Washington 25, D. C.

Prepared by: _____
Dr. R. J. Kenyon, Senior Member, Technical Staff

Approved by: _____
A. W. McEwan, Laboratory Director

_____
A. K. Wing, Jr., Vice-President, Engineering

I T T   E L E C T R O N   T U B E   D I V I S I O N

A Division of International Telephone and Telegraph Corporation

ELECTRON TUBE LABORATORY
P. O. Box 100
Easton, Pennsylvania

ABSTRACT

This contract for the development of electronically tunable converters in the millimeter wave range was divided into four tasks. Task A involved an investigation of the conversion gain of a single circuit converter as a function of intermediate-frequency. A detailed theoretical analysis, with extensive computer results, was performed. This theoretical investigation was supplemented by an experimental program which verified the theory. A noise analysis, based on a simplified noise model, also was made. The results of this investigation have shown that the single circuit converter cannot be used as a receiver front end for low signal levels but can be useful in high level applications.

Task B was an experimental program to determine the characteristics of circular versions of the meander line. Four versions were investigated and the results showed that the plane meander line could be deformed without unduly impairing its properties. The results also showed that the theory of the plane meander line can be used as a guide to the design of modified circuits.

Task C was the design and construction of single circuit backward-wave tubes for operation in the 50 - 75 Gc/s frequency range. Two different designs were followed and one of the designs resulted in a tube which could be operated as either an amplifier or an oscillator. As an oscillator, the tube generated 10 mW minimum power out from 67 to 75 Gc/s with a maximum output of 33 mW at 69 Gc/s.

Task D was the design and construction of double circuit backward-wave converter tubes for operation in the 50 - 75 Gc/s

frequency range. No tubes were built but a low noise gun was designed and built. Gun tests are incomplete. A theoretical analysis of the double circuit converter, with extensive computer results, was performed. A noise analysis also was made and indicated that a noise figure of 20 db was possible for this frequency range. The double circuit converter can be useful as a receiver front end for low signal levels.

ACKNOWLEDGEMENT

TABLE OF CONTENTS

LIST OF ILLUSTRATIONS

LIST OF TABLES

1. INTRODUCTION

The overall aim of this program is to fabricate backward-wave converters for the millimeter region of the spectrum. The feasibility of these devices is based in part on previous experience that this laboratory has had with backward-wave devices for wideband receiver applications. Initial work in this field was done on contract AF30(602)-1545 which called for the development of electronically-swept receivers. These receivers, using a backward-wave amplifier as a preselector, a backward-wave oscillator as the local oscillator, and a crystal as the mixing element in a superheterodyne arrangement were capable of being electronically tuned over an octave in frequency. Amplifiers and oscillators were built for operation in two frequency bands, UHF (500 - 1000 Mc/s) and L (1 - 2 Gc/s).

This success led to further work on contract AF30(602)-2025 to develop a specific backward-wave converter in which the receiver elements are combined in a single vacuum envelope using a single electron beam, the beam also acting as the mixing element. This device is represented schematically in Figure 1. Converters were built in the UHF band, with the i-f at 60 Mc/s, and were capable of conversion gains (r-f power in to i-f power out) in excess of 20 db across the band. The success with these tubes led to the program that presently is being pursued.

As originally conceived, the present program was to be accomplished in four phases which may be summarized as follows:

Phase I - Feasibility study - converter theory and experimental studies of the converter components.
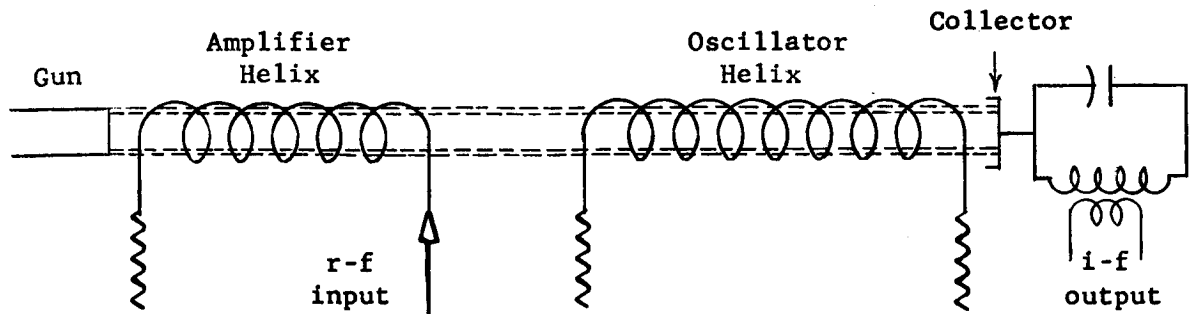
Figure 1. Backward-wave converter

Phase II - Experimental oscillator and amplifier tube fabrication.

Phase III - Semi-breadboard converter tube fabrication.

Phase IV - Final design converter tube fabrication and production.

The first phase of this work was undertaken for NASA on Contract NASw-430. Three main accomplishments were recorded during that contract. First, a theory for the backward-wave converter was evolved which correlated well with experimental data. Second, from a study of slow-wave circuits suitable for use in the millimeter region, a new circuit, the ridge-loaded meander line, emerged which appeared to be the most attractive for wideband performance in the millimeter region. Third, a new concept, the single circuit, backward-wave converter, in which one circuit acts as both amplifier and oscillator, was conceived. Preliminary studies of the single circuit converter indicated that it could be a useful millimeter wave device.

Conclusions drawn from the preliminary studies of the single circuit converter led to a revision in the program. The revision combined Phases II and III (above) into a single phase. It is this

combined phase which is the subject of this contract. The scope of this contract is an experimental program for the development of milli-meter wave, electronically tunable converters. The work program was scheduled in the contract into four tasks. The contract statements of these tasks are summarized as follows:

Task A

Investigate the effect that varying the intermediate-frequency has on the conversion gain of a single circuit converter.

Task B

Experimentally determine the characteristics of ridge-loaded, meander line circuits partially or totally wrapped into a circular con-figuration.

Task C

Design and construct three backward-wave tubes in the 50 to 75 Gc/s range, each of which is suitable for operation as an oscillator, amplifier, or single circuit converter.

Task D

Design and construct three double circuit experimental back-ward-wave converters for operation in the 50 - 75 Gc/s frequency range. This shall be accomplished after completion of Task C.

The first two tasks (A and B) were undertaken concurrently because they were independent of each other. It would have been pre-ferable if the start of Task C could have awaited the completion of Task B. Task C (and Task D) required long lead time items and had to be started as soon as preliminary results were available from Task B. Because Task C was started before all the results of Task B were avail-able and because of technical reasons which will be discussed later,

two of the four circuits which were being studied on Task B were selected for use in Task C tubes. Two designs, using the two circuits, were pursued concurrently. In the time available, it was possible to build and test, with some minor modifications, only first design tubes. Task D tubes, which were to be based on the final design Task C tubes, were not started.

Several theoretical studies, not required but pertinent to this work, were made because they could be done concurrently with required tasks. These were a space charge wave analysis of the double circuit converter and a noise analysis, based on a simplified noise model, both of the single circuit converter and of the double circuit converter.

The technical portion of this report is divided into four sections with one section devoted to each task. The next section (Section 2) describes the work done on Task A. The preliminary studies (performed on Contract NASw-430) indicated that the conversion gain of the single circuit converter could compare favorably to the double circuit converter. The single circuit converter has obvious advantages with respect to construction, size, and weight. However, the detailed analysis and measurements described in Section 2 show that the conversion gain does not come up to expectation; -40 db being the best measured value. Refinements might add another 10 db but this is still more than 50 db down from the best measured values with a double circuit converter. Low conversion gain also breeds high noise figure which further detracts from the performance. This is demonstrated by the noise analysis of the single circuit converter which is included at the end of Section 2.

Section 3 describes the work done on Task B. The work done on Contract NASw-430 showed that, because of broad bandwidth, relatively constant impedance over the band and constructional simplicity, the ridge-loaded meander line is an attractive millimeter wave device. The meander line is a plane structure and hence applicable to strip beams. These beams are much less desirable than cylindrical beams with respect to constructional detail, control, low-noise, etc. Thus, the present task of experimentally determining the characteristics of the meander line modified for cylindrical beam geometry was undertaken. Four circuits were studied. The differences among the four circuits and their development from plane geometry are shown in Figure 2. The first three types (Figures 2b, c and d) varied in their ratio of beam tunnel diameter to bar length while the fourth type (Figure 2e) is a half-circuit or semi-circular circuit whose beam tunnel diameter to bar length ratio is the same as that for Type III. Measurements were made by resonance techniques in both L and S bands. Impedance calcuations were made by zero-order perturbation theory but the accuracy was improved by corrections which accounted for the effect of a higher order mode and for field modifications due to the perturbation.

The effect of the beam tunnel on the circuit properties is only slight although there is a noticeable reduction in the impedance of the -2 space harmonic (that employed in the backward-wave converter) at the low frequency end of the band. The circuits with larger diameter beam tunnels showed strong anti-phase modes which were not apparent in the circuits with smaller tunnel diameters. The semi-circular circuit (Type IV) was also very free of spurious modes and, as was to be expected, had an interaction impedance which was very nearly the same as that of the plane meander line.
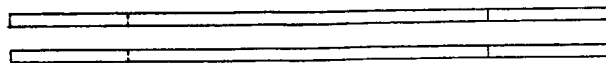
Plane meander lines
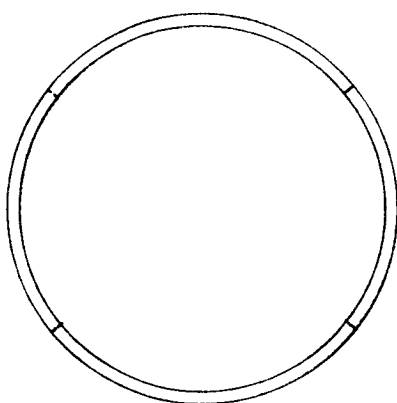
Type I
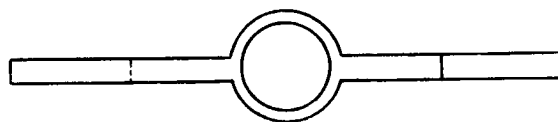
Type II
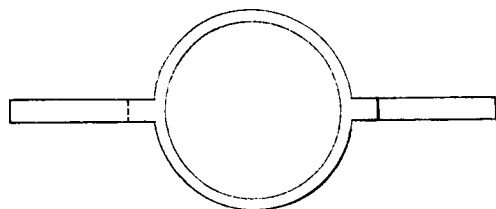
Type III

Type IV

Figure 2. End view of the plane meander line and four cylindrical geometry modifications. Mean bar length is the same for all circuits

Section 4 describes the work done on Task C. Tubes were built using Type III and Type IV circuits. Both amplified, the former also oscillated. Design considerations are discussed and the measurements made on the full-circular circuit tube are presented.

Section 5 describes the work done on Task D. The design of a double circuit backward-wave converter requires several features not present in the simpler single circuit converter. These features are discussed in this section. In addition, the design of a low-noise gun is presented. A space charge wave analysis, with computer results, and a noise analysis, based on a simple noise model, also are presented for the double circuit converter.

Finally, Section 6 presents the conclusions and recommendations for further work. Because we are convinced that the designs bascially are sound, we are continuing work on a modified Task C tube under an ITT internally funded program. Based on the expected success with these tubes and the results presented in this report, we recommend that work on millimeter wave double circuit converters be continued.

2. TASK A

2.1 Introduction

The single circuit, backward-wave converter (SCC) is a swept superheterodyne receiver front end in which a single slow-wave structure, operating in a backward-wave space harmonic, interacting with an electron beam, performs the function of the r-f amplifier, local oscillator, and mixer (Figure 3). Compared to a double circuit, backward-wave converter
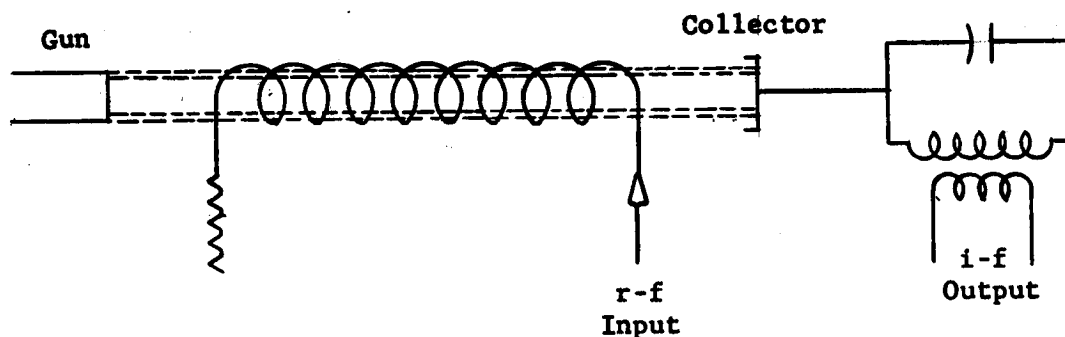
Figure 3. Single circuit converter

(DCC), such as that shown schematically in Figure 1, the SCC has several obvious advantages. It is easier to fabricate and build. It is shorter and, principally because a smaller magnet is needed, weighs less than the DCC. The DCC requires two swept voltages that must be tracked together. Since the SCC requires only one, the power supply complexity can be reduced significantly, thereby reducing the size and weight of a complete receiver package.

A theoretical study of the SCC was begun on Contract NASw-430. At the end of that contract, an equation for the i-f current magnitude had been derived and calculations based on a two-wave (high QC),

lossless theory had been made. A comparison made between the i-f currents of a SCC and a DCC indicated that the conversion gain of a SCC could exceed that of a DCC. Some disadvantages of the SCC were noted. These included poor image frequency rejection, higher noise figure, and less freedom for choosing the value of the i-f than with the DCC. A further and more detailed study of the SCC was required and was the basis for Task A.

Task A involved both a theoretical and an experimental program. Part of the theoretical program has been reported in the past, both in the final report on Contract NASw-430 and in the bimonthly reports on this contract. However, for the sake of completeness, the theory will be presented here in its entirety. The problem we wish to consider is: if a signal is injected into a SCC (see Figure 3) at frequency f_s while the device is oscillating at frequency f_o, what is the difference frequency current on the beam, i_d? The difference frequency, f_d, is given by $f_d = |f_s - f_o|$. If the real part of the effective i-f[+] load impedance is R_L, then the power out at the difference frequency is $(1/2)i_d^2 R_L$ and thus, the conversion gain may be determined. The solution is based on a first order nonlinear model for frequency conversion which has been investigated by DeGrasse. The DeGrasse equations in turn require the solutions for the space charge waves which are solved using coupled mode theory. The equations were programmed for computer solution and the results are presented as curves of a normalized difference frequency current as a function of normalized difference frequency. Also presented are curves of current as a function of circuit loss and as a function of QC.

[+]i-f and difference frequency, as used in this report, are synonymous.

The measurement program was performed on a vehicle designed to operate in S-band. The vehicle actually was a DCC but could be used as a SCC simply by keeping the first (amplifier) helix inoperative. In order to test the theory, the conversion gain was measured as a function of f_d with f_0 held constant. In addition, to make theoretical calculations for this specific experiment, a measurement of r-f gain as a function of f_s while the tube was oscillating at f_0 was required and was made.

2.2 Theoretical Investigation

For many practical purposes an electron beam can be regarded as having a linear characteristic, that is, the current and velocity at one point are linearly related to the current and velocity at another point. This relationship no longer applies when the a-c quantities are comparable with the d-c quantities. The non-linearity which then appears is responsible for saturation, frequency multiplication and mixing. If two signals of frequencies f_a and f_b are simultaneously impressed, then due to the non-linearities, $f_a \pm f_b$, $2f_a$, $2f_b$, $2f_a \pm f_b$, $f_a \pm 2f_b$, etc. frequencies also will be present. The phenomenon of frequency conversion was investigated by DeGrasse[1] assuming a first order non-linear model, that is, the signal at the frequency of interest is assumed to be proportional to the amplitude at the fundamental frequencies.

In the SCC we wish to extract the difference frequency term. DeGrasse has shown that the current and velocity at this frequency can be obtained in the following form

---

[1]All references are given in Section 7.

$$dv_d/dz = -j(\omega_{qd}/\omega_d)(i_d/I_o) - (2U_o)^{-1}(d/dz)(v_ov_s^*) -j(\omega_d/U_o)v_ov_s^* \quad (2-1)$$

$$di_d/dz = j(\omega_d/U_o^2)I_o - U_o + (2I_o)^{-1}(i_ov_s^* + v_oi_s^*) + v_ov_s/U_o \quad (2-2)$$

where i_d, v_d are the current and velocity respectively, at the difference radian frequency, ω_d. i_o, v_o and i_s, v_s are the corresponding quantities at the oscillator radian frequency ω_o and the signal radian frequency, ω_s, respectively. I_o and U_o are the d-c current and velocity, ω_{qd} is the reduced plasma radian frequency at ω_d, and * denotes the complex conjugate. i_o, v_o, i_s, and v_s may be related to the fast and slow space charge waves by the following relations.

$$i_o = \sqrt{2/W_o}\ (A_{fo} - A_{qo}) \quad (2-3)$$

$$v_o = (U_o/2V_o)\sqrt{2W_o}\ (A_{fo} + A_{qo}) \quad (2-4)$$

$$i_s = \sqrt{2/W_s}\ (A_{fs} - A_{qs}) \quad (2-5)$$

$$v_s = (U_o/2V_o)\sqrt{2W_s}\ (A_{fs} + A_{qs}) \quad (2-6)$$

with

$$W_o = 2V_o/k_oI_o \ , \ W_s = 2V_o/k_sI_o$$

$$k_o = \omega_o/\omega_{qo} \ , \ k_s = \omega_s/\omega_{qs}$$

where A_{fo} and A_{fs} denote the fast space charge waves at ω_o and ω_s respectively, A_{qo} and A_{qs} denote the slow space charge waves at ω_o and ω_s respectively, V_o is the d-c voltage, and ω_{qo} and ω_{qs} denote the reduced plasma radian frequency at ω_o and ω_s respectively.

At this point there is no difference between the SCC and the DCC. The difference arises in the derivation of the space charge waves.

The discussion of the DCC will be deferred until Section 5. The derivation of the space charge waves for the SCC is given in Appendix A. Also given in Appendix A is the solution for the SCC difference frequency current, i_{d1}. It may be written as (see Equation (A-16))

$$i_{d1} = \sqrt{P_s C I_o / V_o} \; H_1 \qquad (2\text{-}7)$$

where P_s is the input power to the circuit at f_s, C is Pierce's gain parameter and H_1 is a complicated function of the system parameters. H_1 is derived in Appendix A and, in general, is given by Equation (A-17). An approximate form of H_1 for cases when QC is high is given by Equation (A-19) while another approximation for H_1 for high QC and no loss is given by Equation (A-20).

The conversion gain for a SCC, g_1, is defined by

$$g_1 = (1/2) i_{d1}^2 R_L / P_s = (1/2) C (I_o / V_o) R_L H_1^2 \qquad (2\text{-}8)$$

or in db by

$$G_1 = 10 \log g_1 = 10 \log (1/2) C (I_o / V_o) R_L H_1^2 \qquad (2\text{-}9)$$

The variation of conversion gain with difference frequency can be seen in curves of normalized i-f current, H_1, as a function of normalized difference frequency, f_d / f_o. To this end, Equations (A-17) and (A-19) for H_1 were programmed for solutions on an electronic digital computer. Two values of QC were chosen: QC = 0.2 and 1; four values of the total circuit loss parameter were chosen: Ω = 0, 10, 20, and 30 db. The range of the difference frequency was taken as $0 \leq f_d / f_o \leq 0.1$. The value of ω_{qd} / ω_d was required for the calculations

and a value of 0.07^+ was determined with the aid of curves given by Branch and Mihran.[2]

The curves of H_1 as a function of f_d/f_o are presented in Figures 4 - 6. In the region $0.02 < f_d/f_o < 0.1$, H_1 goes through a series of maxima and minima. This is shown in Figure 4. The dashed curve represents the mean value of H_1 in this region. For all other curves (Figures 5 and 6), H_1 is smoothed out where a similar variation is encountered. In order that zero may be shown on a logarithmic axis, the first part of the f_d/f_o axis is shown broken so that the origin of this axis is zero, not 0.001 as it would be normally. This procedure is adopted in Figures 4 - 6.

Figure 7 shows the variation of H_1 as a function of Ω for f_d/f_o approaching zero. The curve labeled "Large QC" is the solution of Equation (A-19) for the two-wave theory, that is, the theory with the fast space charge wave neglected. It can be seen that the two-wave theory is a good approximation for $QC > 2$.

Figure 8 shows the variation of H_1, as a function of QC for f_d/f_o approaching zero. H_1 increases with QC until it saturates at the value given by the two-wave theory. This occurs at $QC \approx 1$ except for $\Omega = 0$.

A study of these curves leads to the conclusion that the conversion gain of a SCC increases either as the difference frequency decreases, as QC increases, or as the circuit loss decreases. The latter is a not unexpected result.

In order to show what these values mean with respect to the conversion gain of a millimeter device, a specific example is given.

$^+$The value of ω_{qd}/ω_d was not critical since reducing it from .07 to .0005 altered H_1 by less than a half of one percent.
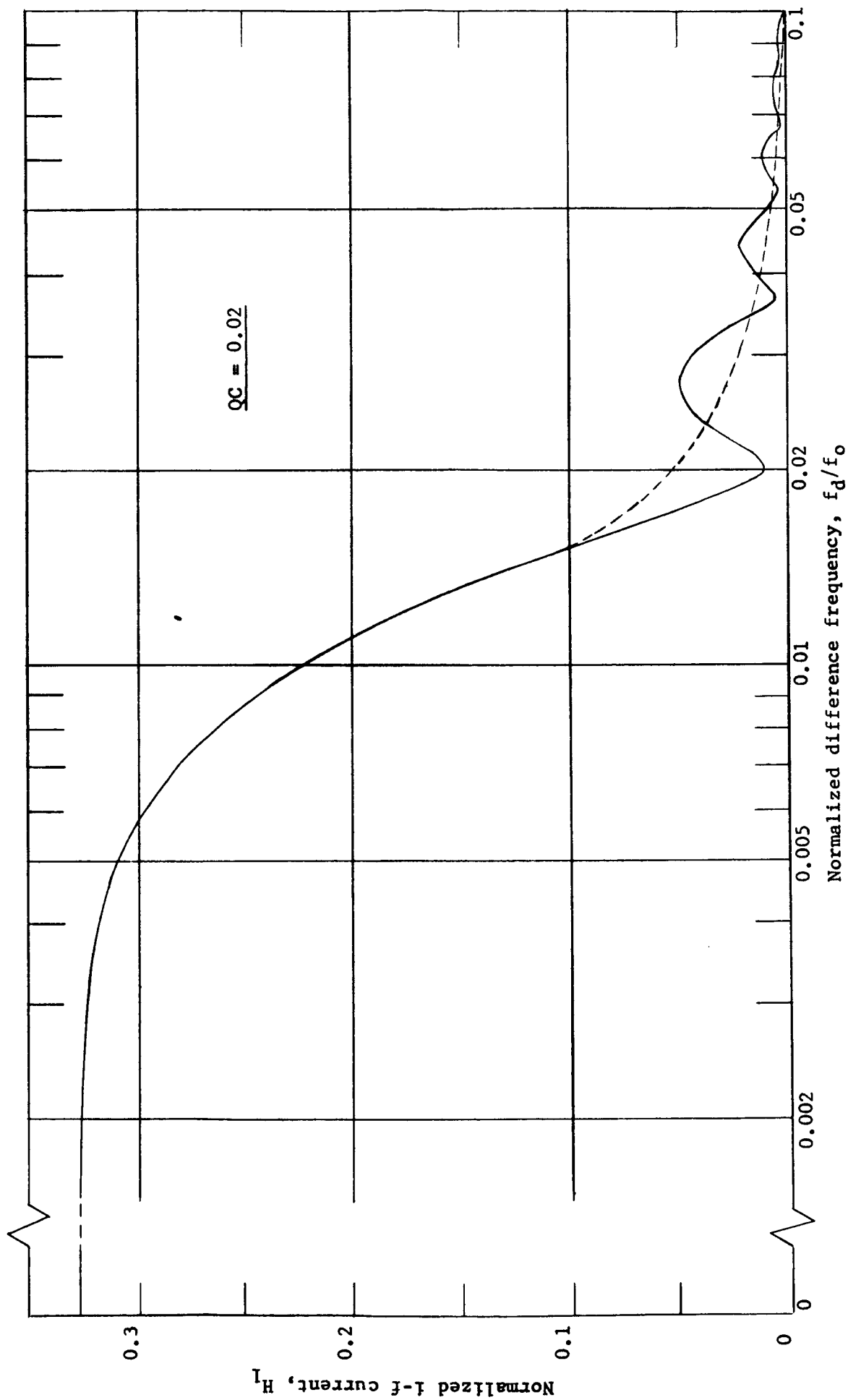
Figure 4. Normalized i-f current as a function of normalized difference frequency for QC = 0.02 and Ω = 0.
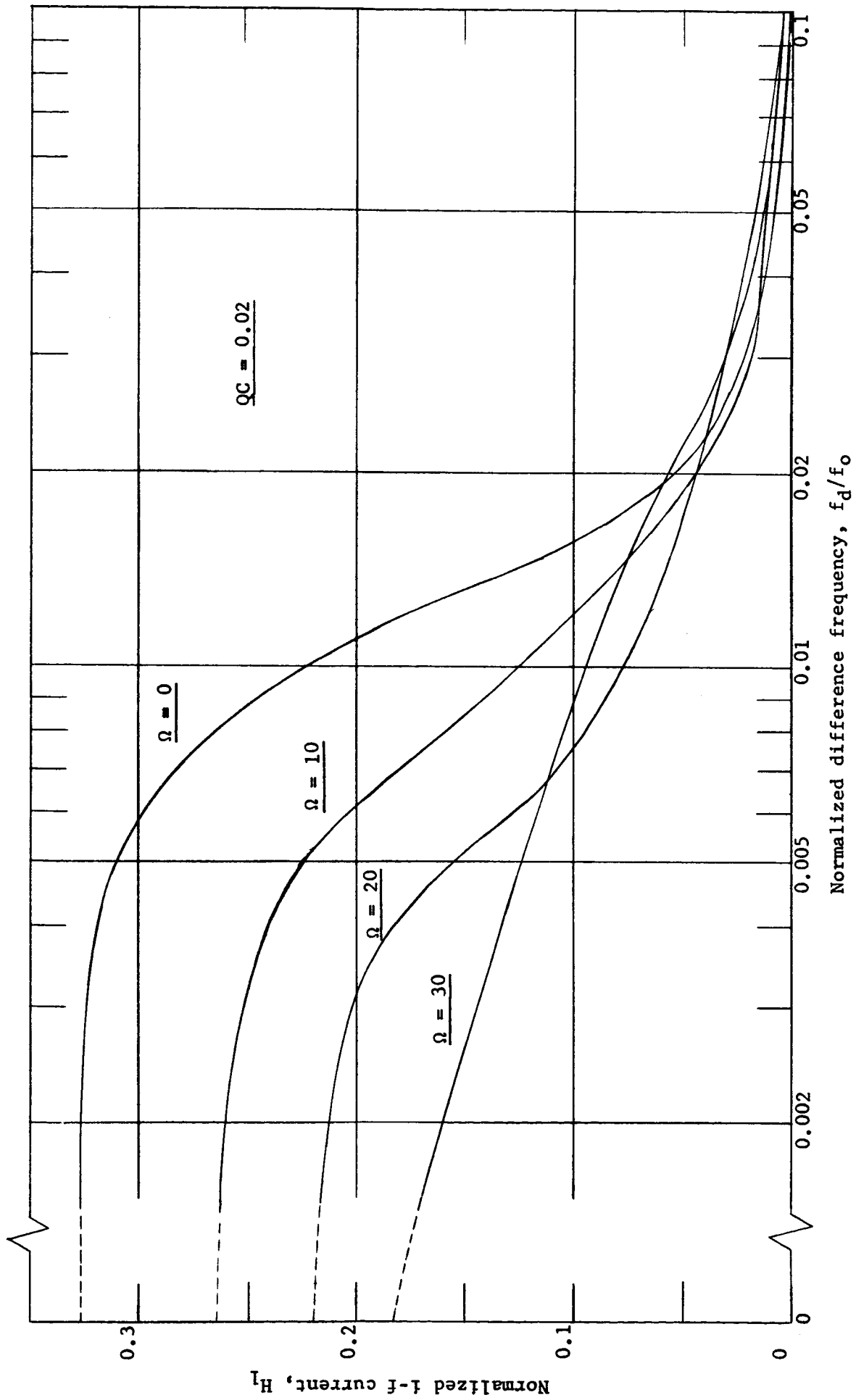
Figure 5. Normalized i-f current as a function of normalized difference frequency for QC = 0.02
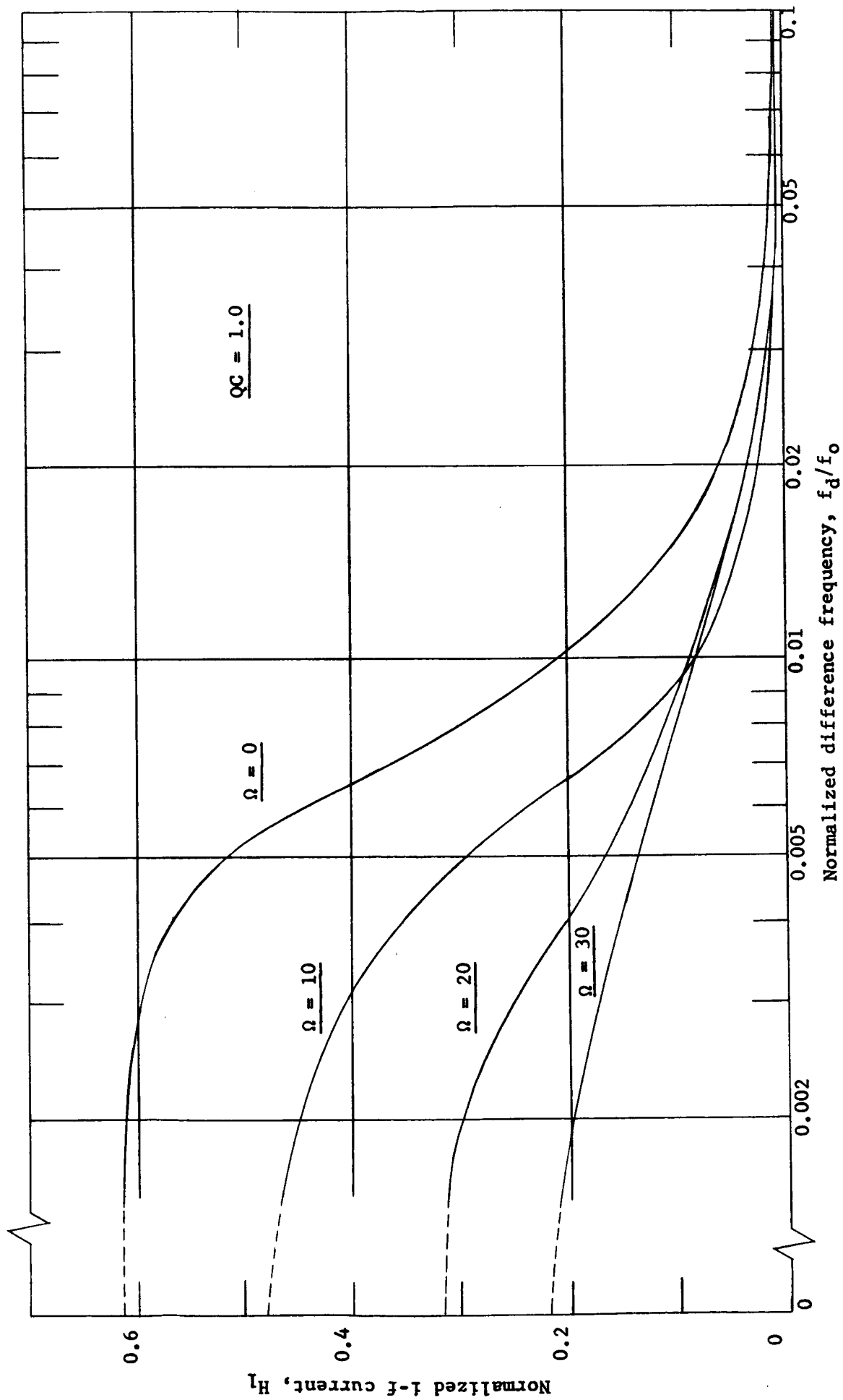
Figure 6. Normalized i-f current as a function of normalized difference frequency for QC = 1.0
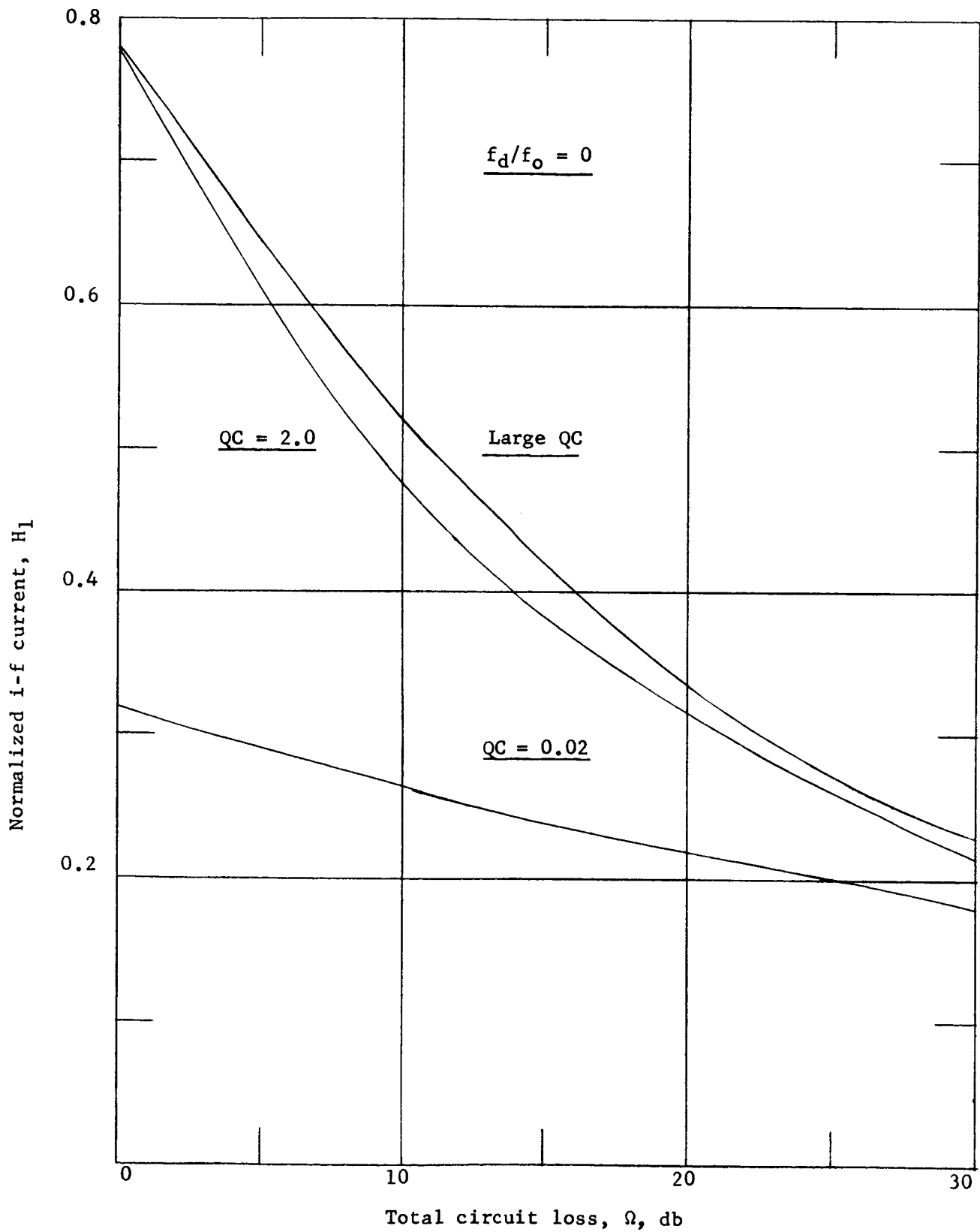
Figure 7. Normalized i-f current as a function of circuit loss
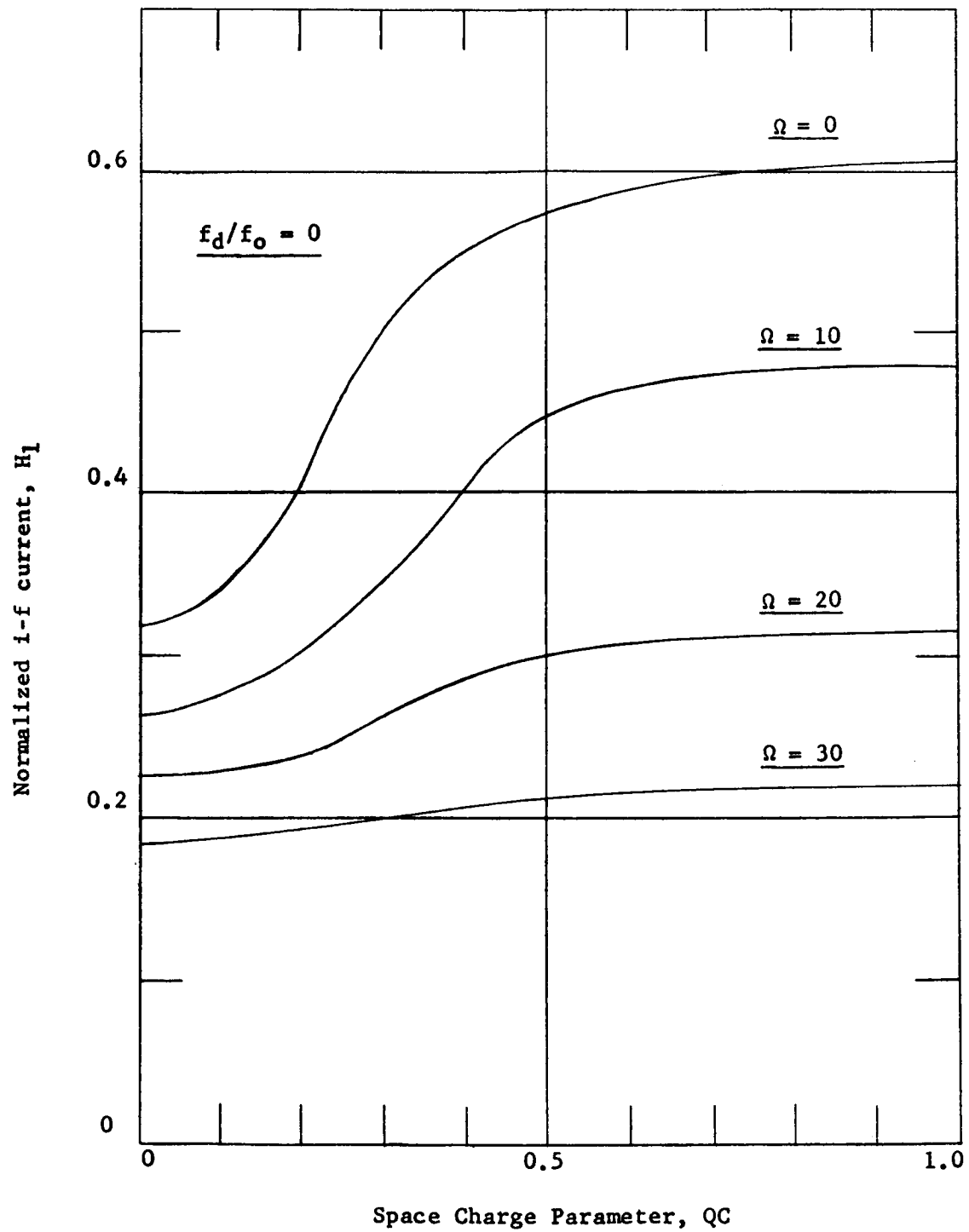
Figure 8. Normalized i-f current as a function of QC

A possible embodiment at these wavelengths is the ridge loaded meander line which leads to the following data:

$$\Omega = 10 \text{ db}$$

$$I_o = 2.95 \text{ mAmp.}$$

$$V_o = 1680 \text{ volts}$$

$$K_i = 0.692 \text{ ohms}$$

where K_i is the interaction impedance. At $f_o = 62$ Gc/s, these values give:

$$C = 0.006715$$

$$CN = 0.39$$

$$QC = 0.0253$$

Choosing $f_d = 2$ Gc/s ($f_s = 64$ Gc/s),

$$H_1 = 0.016$$

If the i-f signal is coupled out by using the beam to drive a resonant cavity which is operating into a matched load, the i-f power to the load, P_d is

$$P_d = (1/8) i_d^2 R_o$$

where R_o is the effective shunt resistance of the cavity as presented to the beam. For this case, the conversion gain in db is

$$G_1 = 10 \log (P_d / P_s)$$

$$= 10 \log \left[(CI_o / 8 V_o) H_1^2 R_o \right]$$

For a cavity shunt impedance of 1/2 megohm

$$G_1 \approx -67 \text{ db}$$

2.3 Experimental Program

A schematic representation of the experimental tube, F-2524, and its power supplies is shown in Figure 9. The specifications of the helices and beam are given in Table 1. A photograph of the tube

Amplifier Helix	: 9 t.p.i., 5.296 in. long (47-2/3 turns)
Drift Helix	: 9 t.p.i., 0.629 in. long (5-2/3 turns)
Oscillator Helix	: 8 t.p.i., 8.500 in. long (68 turns)
Helix Material (all helices)	: 0.050 in. wide x 0.010 in. thick molybdenum tape.
Helix Diameters (all helices)	: 0.361 in. I.D.; 0.381 in. O.D.
Beam Diameters	: 0.285 in. I.D.; 0.325 in. O.D.

Table 1. Helix and beam specifications for S-band backward-wave converter

is shown in Figure 10. For SCC operation, the voltage on the amplifier helix is kept low enough to keep it inoperative from an r-f standpoint. Both r-f terminals for the amplifier helix are terminated in matched loads. Thus, only the oscillator helix is used in this experiment.

The d-c operating parameters are held constant throughout the experiment. They are listed in Table 2. The value of the oscillator helix voltage is nominal; it is always adjusted such that $f_0 = 2700$ Mc/s.
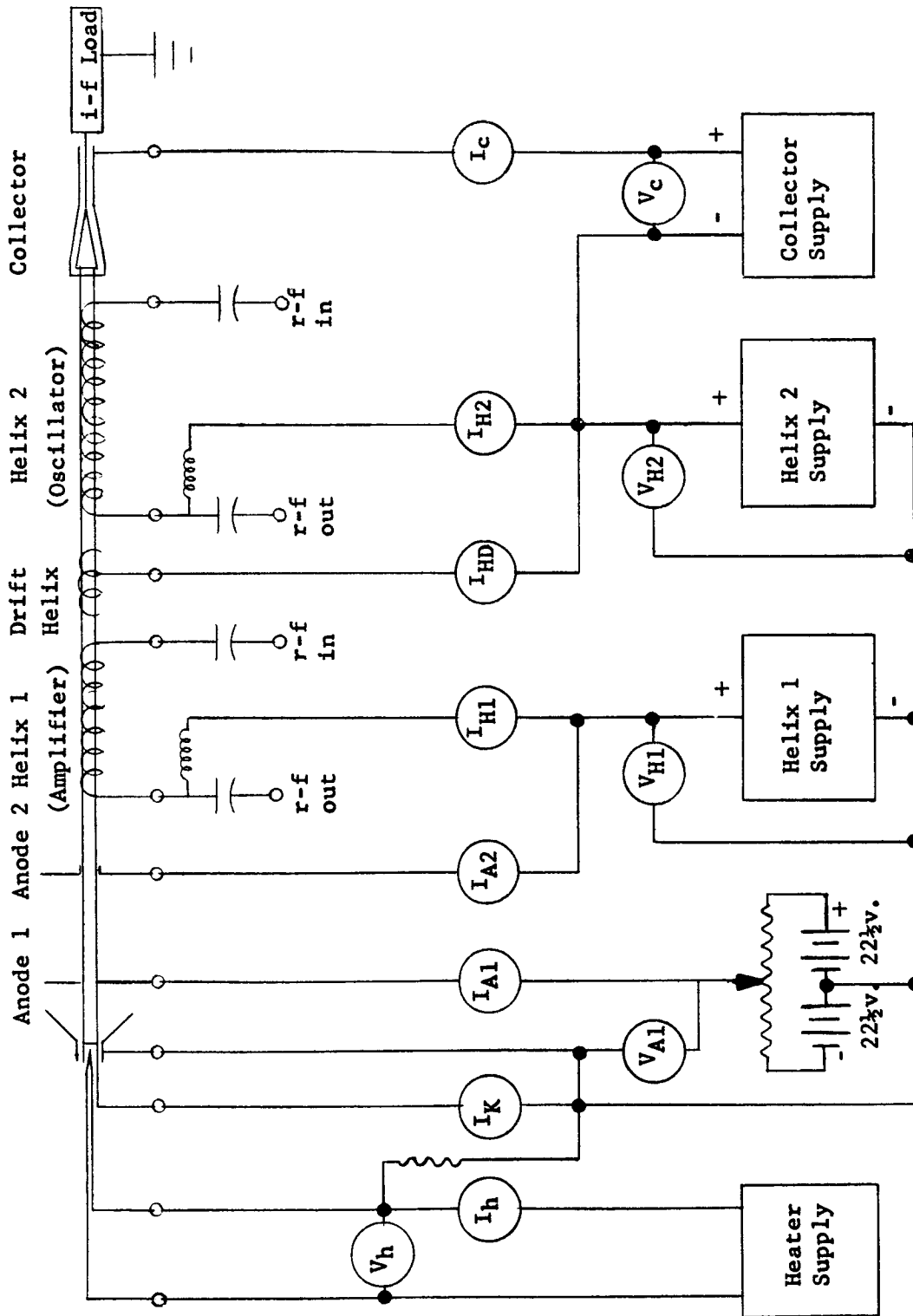
Figure 9. Schematic representation of S-band backward-wave converter and d-c circuit
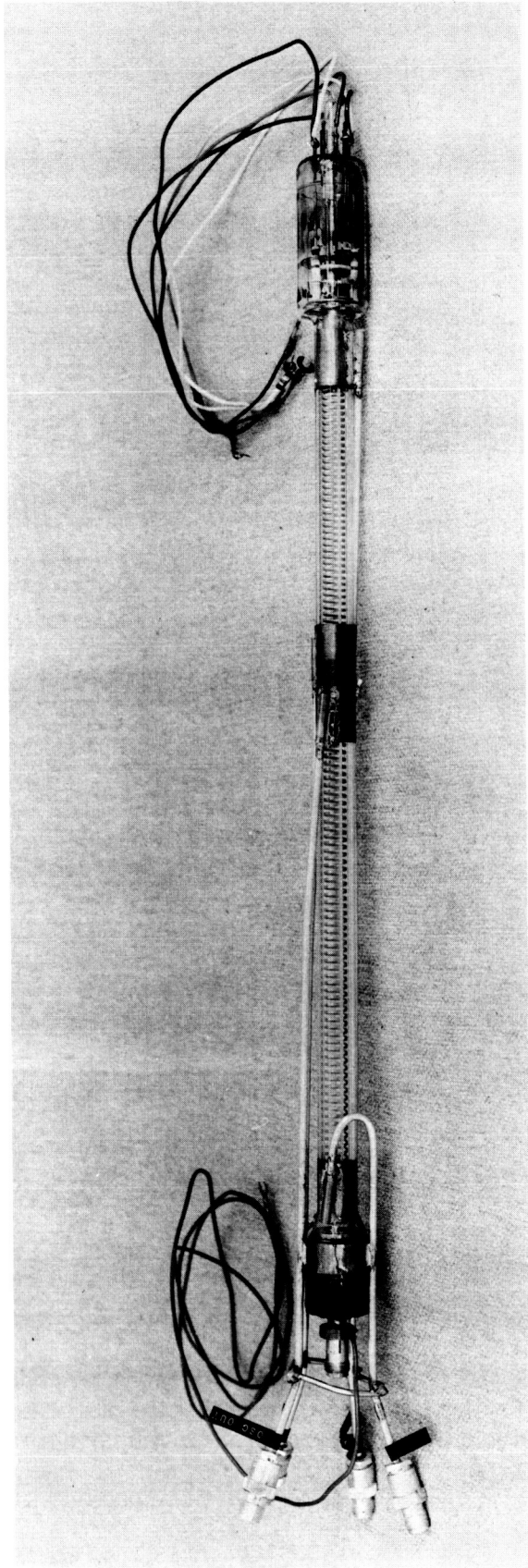
Figure 10. S-band backward-wave converter tube

V_h = 5.8 v.	V_{H1} = 200 v.	I_k = 2 ma.
I_h = 2.85 a.	$V_{H2} \approx$ 450 v.	$I_c \approx I_k$
	V_C = 200 v.	

Table 2. d-c operating parameters for SCC experiment

With the values from Tables 1 and 2, it is possible to determine the r-f parameters of the SCC. From the Stanford nomograph[3] the value of the -1 space harmonic impedance, K_{-1}, was determined to be

$$K_{-1} = 1.44 \ \Omega$$

Pierce's gain parameter, C, is given by

$$C = (K_{-1}I_o)/(4V_o) = 1.6 \times 10^{-6}$$

and therefore

$$C \approx 0.01$$

With the aid of curves given by Branch and Mihran[2], the plasma frequency reduction factor was determined to be 0.45 which in turn yields a value for QC of 0.3.

Basically, just two experiments were performed: backward-wave amplification in the presence of backward-wave oscillation as a function of signal frequency and SCC conversion gain as a function of difference frequency. Actually, a number of preliminary experiments were made to determine how refined the final forms of the experiments needed to be, but they will not be reported here. The experiments (in their final form) were performed several different times to assure that the data

were repeatable. The results presented in this section are a compilation of those data.

2.3.1 Amplifier Gain in the Presence of Oscillation

Figure 11 is a schematic diagram of the circuit used to measure amplifier gain in the presence of oscillation as a function of f_s (or f_d as f_o is held constant throughout the experiment). The experiment proceeds as follows: The SCC is turned on and the helix voltage adjusted to make $f = 2700$ Mc/s as measured by the frequency meter marked f_o. The HP oscillator is set to a frequency of interest (f_s). For values of f_s such that 2690 Mc/s $\leq f_s \leq$ 2710 Mc/s, the value of f_s is determined by using the spectrum calibrator marker on the spectrum analyzer to measure the difference between f_s and f_o. For values of f_s outside this range, the value of f_s is measured using the frequency meter marked f_s. (The frequency meter marked f_o was calibrated with the one marked f_s.) Then, with the coaxial switch in position 1, the sensitivity of the spectrum analyzer, which has been tuned to display f_s, and the power output of the HP oscillator are adjusted to give a convenient deflection at a reasonable power level. The analyzer deflection of f_s is noted. The reading of the calibrated output of the HP oscillator (in dbm) is recorded. The switch then is moved to position 2, the HP oscillator power output is readjusted to bring the analyzer deflection back to its original value, and this HP oscillator output reading is recorded. This position 2 procedure is repeated for position 3 and for positions 1, 2 and 3 with the SCC beam off. The analyzer sensitivity is never readjusted after its beam on-position 1 adjustment.
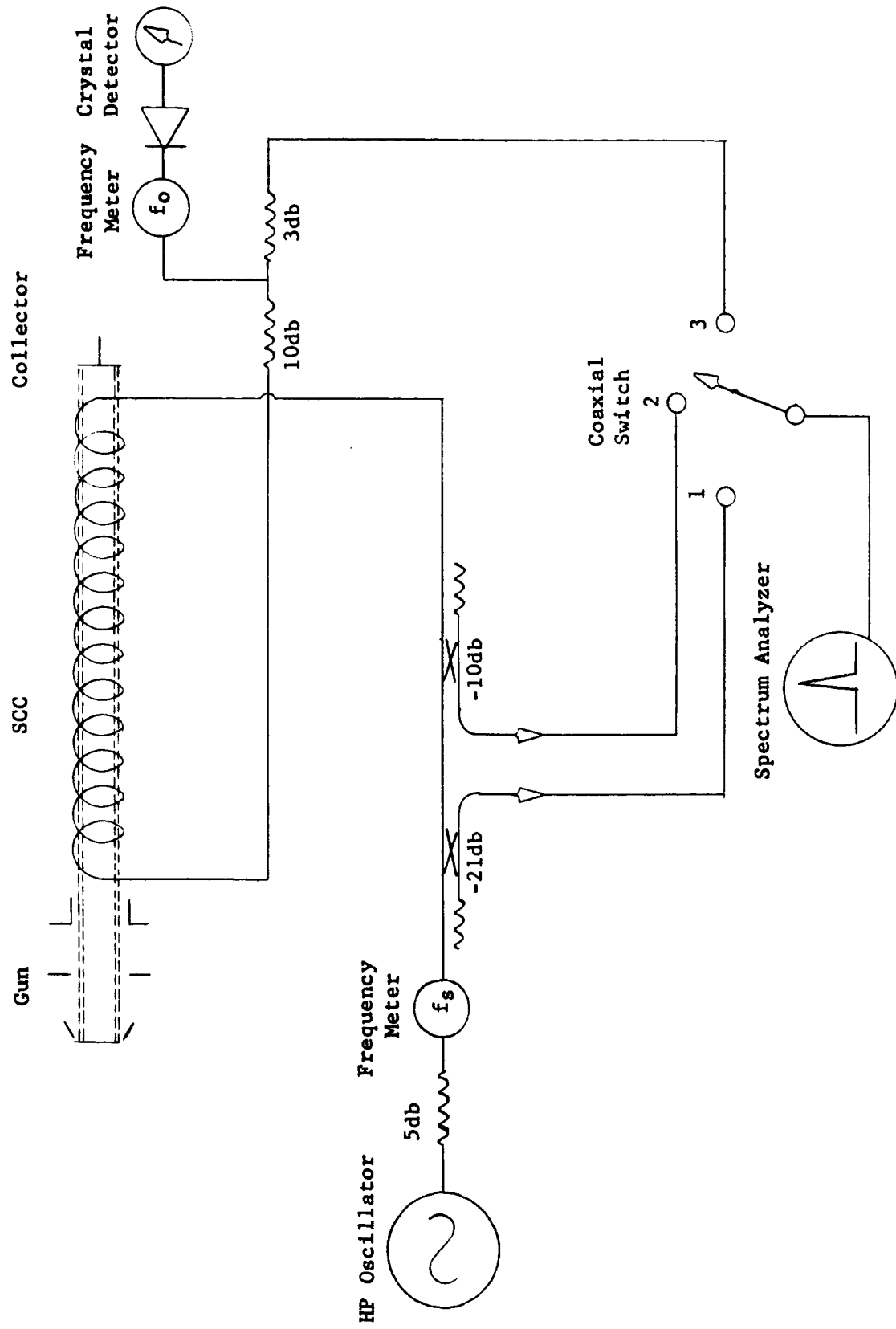
Figure 11. Schematic diagram for measurement of amplifier gain in the presence of oscillation

Thus, for each f_s, six readings of the HP oscillator calibrated output are recorded. They are labeled in the form "dbm_{Ai}" where the A is either H (hot), indicating the SCC beam on condition, or C (cold), indicating the SCC beam off condition, and i = 1, 2 or 3 indicating switch position 1, 2 or 3 respectively. The amplifier gain above cold loss (in db) in the presence of oscillation, G_s, is shown in Appendix B to be

$$G_s = (dbm_{C3} - dbm_{H3}) + (dbm_{H1} - dbm_{C1}) + 10 \log(T_C/T_H) \qquad (2\text{-}10)$$

where T_C and T_H are the input transmission coefficients to the SCC for the beam on and the beam off conditions respectively. T_C and T_H are determined from measured input SWR values. The derivation of T_C and T_H also is given in Appendix B.

A curve of G_s as a function of f_s is shown in Figure 12. The same measurement made on a millimeter SCC ($f_o = 70$ Gc/s) yields a nearly identical curve (see Section 4.4.2) indicating that the performance shown in Figure 12 is typical of this type of operation.

2.3.2 Conversion Gain

Figure 13 is a schematic diagram of the circuit used to measure normalized difference frequency current, H_1, as a function of f_d. This was done instead of a simple conversion gain measurement in order that correlation with the theory of Section 2.2 could more easily be made. Solving Equation (2-7) for H_1 yields

$$H_1 = \sqrt{V_o/P_s C I_o} \; i_{d1} \qquad (2\text{-}11)$$

V_o and I_o are given in Table 2 as 450 volts and 2 milliamperes respectively. C was determined to be 0.01. Therefore, for this
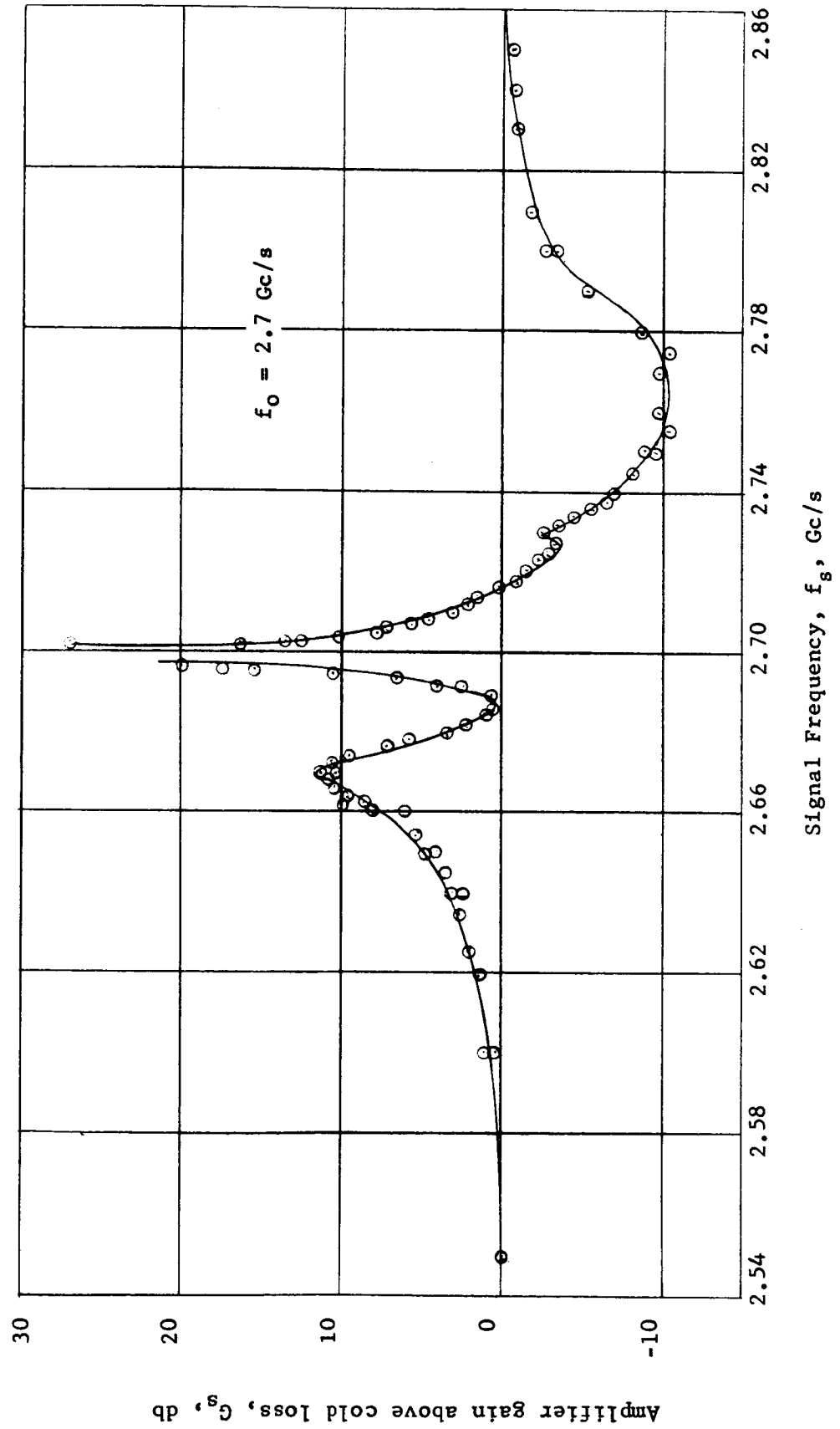
Figure 12. Amplifier gain in the presence of oscillation as a function of signal frequency for an S-band SCC
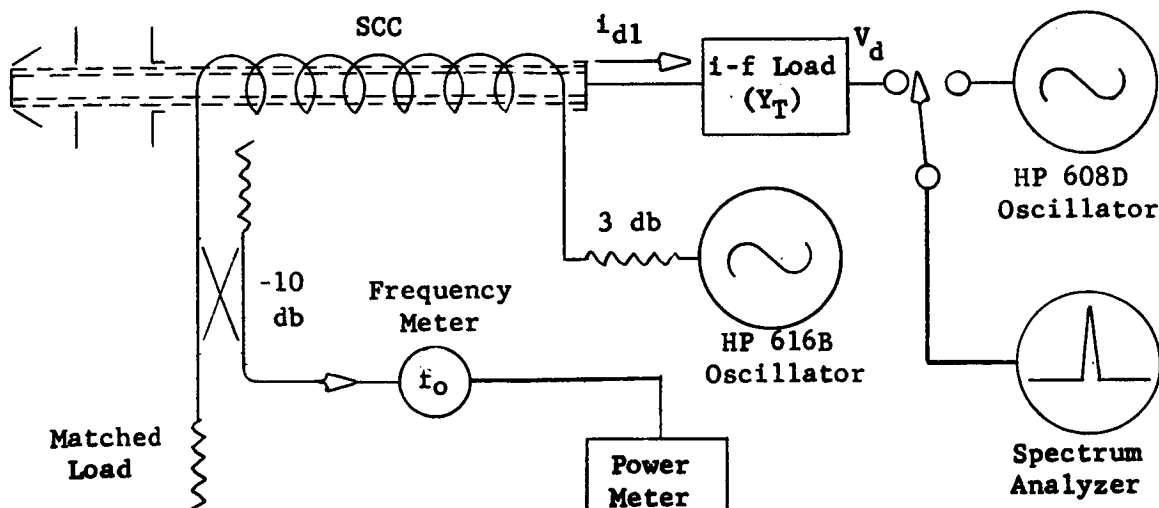
Figure 13. Schematic diagram for measurement of SCC i-f current.

experiment, Equation (2-11) may be rewritten as

$$H_1 = 4.75 \times 10^3 \ i_{d1} P_s^{-1/2} \qquad (2\text{-}11a)$$

The two quantities which are measured are V_s, the output

voltage of the HP 616B oscillator and V_d, the output voltage of the

i-f load. P_s and i_{d1} must be related to these quantities. P_s can be

related to V_s in the following fashion: the power out of the HP 616B

into a 50 Ω line is $V_s^2/50$. This power is reduced by the 3 db attenu-

ator and is further reduced by the hot input power transmission co-

efficient, T_H (see Appendix B). Thus

$$P_s = (V_s^2/50)(0.5)T_H = 0.01 \ T_H V_s^2 \qquad (2\text{-}12)$$

i_{d1} is related to V_d by the definition of the transfer admittance of

the i-f load, Y_T, that is

$$i_{d1} \triangleq \sqrt{2} \ Y_T V_d \qquad (2\text{-}13)$$

(The $\sqrt{2}$ appears because i_{d1} is a peak value while V_d is an rms value).

Substituting Equations (2-12) and (2-13) into Equation (2-11a) yields

$$H_1 = 6.7 \times 10^{-2} \, T_H^{-1/2} Y_T V_d / V_s \qquad (2\text{-}11b)$$

which relates the normalized i-f current, H_1, to experimentally determined quantities.

For each point on the H_1 versus f_d/f_o curve, it is necessary to measure six quantities: f_o, f_d, T_H, V_s, V_d, and Y_T. As before, f_o is measured with the frequency meter (Figure 13) and is kept constant at 2.70 Gc/s. V_s is the output voltage of the HP 616B oscillator. V_d and f_d are measured by comparison with the calibrated output (both in frequency and voltage) of the HP 608D oscillator. The value of T_H as a function of f_s ($= f_o \pm f_d$) is taken from the previous experiment of amplifier gain in the presence of oscillation. Y_T is determined from the effective i-f load impedance, R_L, which has been, both on this contract and the previous one (NASw-430), a very elusive quantity to evaluate. Actually, if purely resistive elements are used, R_L can be determined. However, its maximum value is limited, in general, to the characteristic impedance of the coaxial line, 50 Ω in this case. This is too low to give a measurable output signal over the whole range of f_d of interest. On the other hand, high values of R_L can be obtained by resonant circuitry such as shown in Figure 3, but now it is difficult either to calculate or to measure R_L. This means, of course, that Y_T cannot be evaluated and consequently, H_1 cannot be measured experimentally.

Figure 14 is a schematic representation of the i-f load (and collector) used to obviate these problems. The impedance looking to the right of R_1 is, for all practical purposes, an open circuit. Thus,
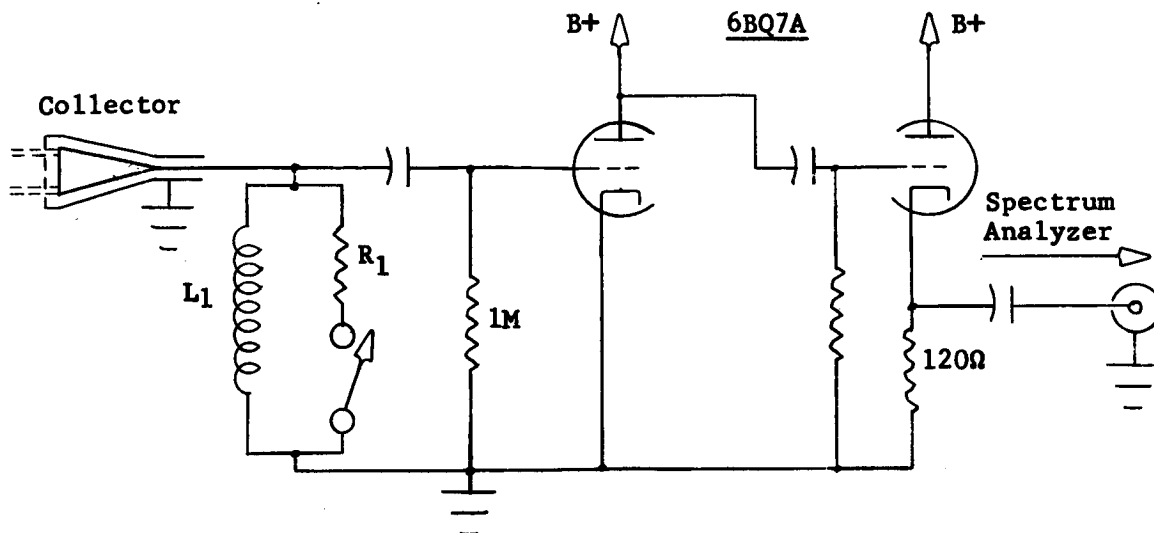
Figure 14. Schematic diagram of SCC collector and i-f load.

Figure 14 may be represented by the equivalent circuit shown in Figure 15 where C_g is the capacitance of the collector gap, C_d is the distributed capacitance of the collector and coaxial line, L_1 is an air core coil used to resonate the circuit at the f_d of interest, R_1 is a carbon resistor whose value is known and μ is the voltage gain of the two stage cathode follower output amplifier.
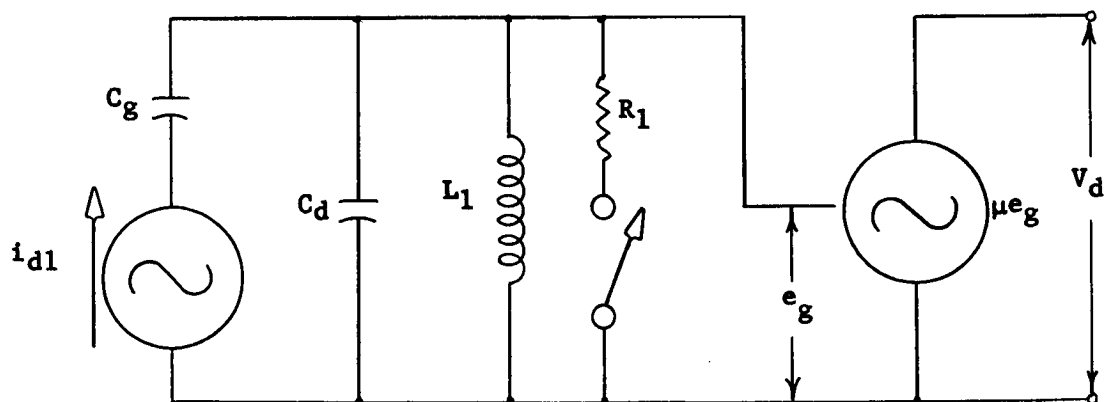
Figure 15. Equivalent circuit of Figure 14.

In practice, an air core coil was wound and f_d adjusted (by varying f_s) for resonance. This was done for each f_d. In this case, the equivalent circuit can be reduced further and is shown in Figure 16.
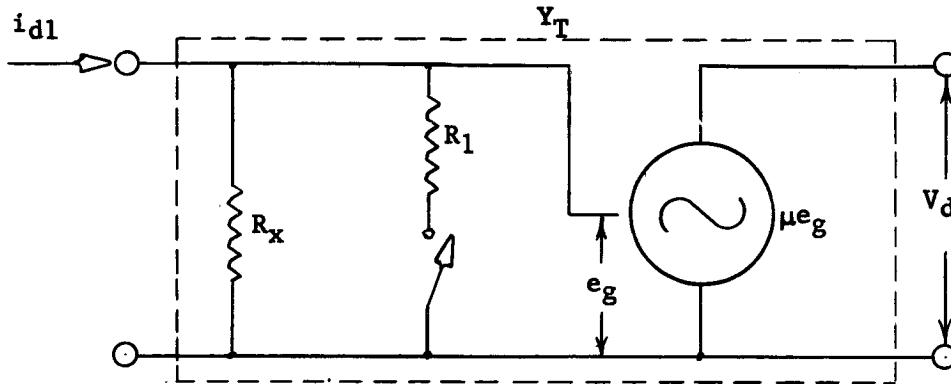
Figure 16. Equivalent circuit of Figure 15 at resonance.

The experiment (at each f_d) is done for two conditions, switch open and switch closed. With the switch open, the transfer admittance, Y_{TO}, is given by

$$Y_{TO} = (\mu R_x)^{-1} \qquad (2\text{-}14a)$$

and for the switch closed, Y_{TC} is given by

$$Y_{TC} = (R_x + R_1)/(\mu R_x R_1) \qquad (2\text{-}14b)$$

The experiment proceeds as follows:

1. With the switch open, f_s is adjusted to obtain the proper f_d for resonance.

2. The spectrum analyzer is calibrated with respect to V_d at f_d by the HP 608D oscillator.

3. V_s is adjusted to give a convenient analyzer deflection corresponding to V_d. This value of V_s is labeled V_{so}.

4. The switch is closed and V_s is increased so as to cause the same analyzer deflection as in step 3 above. This value of V_s is labeled V_{sc}.

5. μ is measured at this f_d using the HP 606D oscillator.

H_1 may now be calculated. Rearranging Equation (2-11b) slightly and writing it for the two conditions yields

$$V_{sc}H_1 = 6.7 \times 10^{-2}T_H^{-1/2}V_dY_{TC} \qquad (2\text{-}15a)$$

$$V_{so}H_1 = 6.7 \times 10^{-2}T_H^{-1/2}V_dY_{TO} \qquad (2\text{-}15b)$$

Subtracting Equation (2-15b) from (2-15a), substituting Equation (2-14a) and (2-14b) for Y_{TO} and Y_{TC} respectively, and solving for H_1 yields

$$H_1 = 6.2 \times 10^{-5} (\mu T_H^{1/2})^{-1}V_d/\Delta V_s \qquad (2\text{-}16)$$

where $\Delta V_s = V_{sc} - V_{so}$ and $R_1 = 1080\ \Omega$. Equation (2-16) gives the value of H_1 in terms of quantities that can be measured experimentally.

Figures 17 and 18 show the results of this experiment. Both theoretical and experimental H_1 are plotted as functions of f_d/f_o. The theoretical curves of H_1 do not appear similar to any of those in Figures 5 and 6 because the experimental amplifier gain curve (Figure 12) was used here rather than the assumed hyperbolic amplifier gain curve which was used to calculate the curves of Figures 5 and 6. The spread in the experimental data is the result of several measurements, using different values for V_d, at each f_d. The correlation is quite good.

Using Equation (2-9), we may calculate an experimental conversion gain. C, I_o, and V_o already have been given. The best value
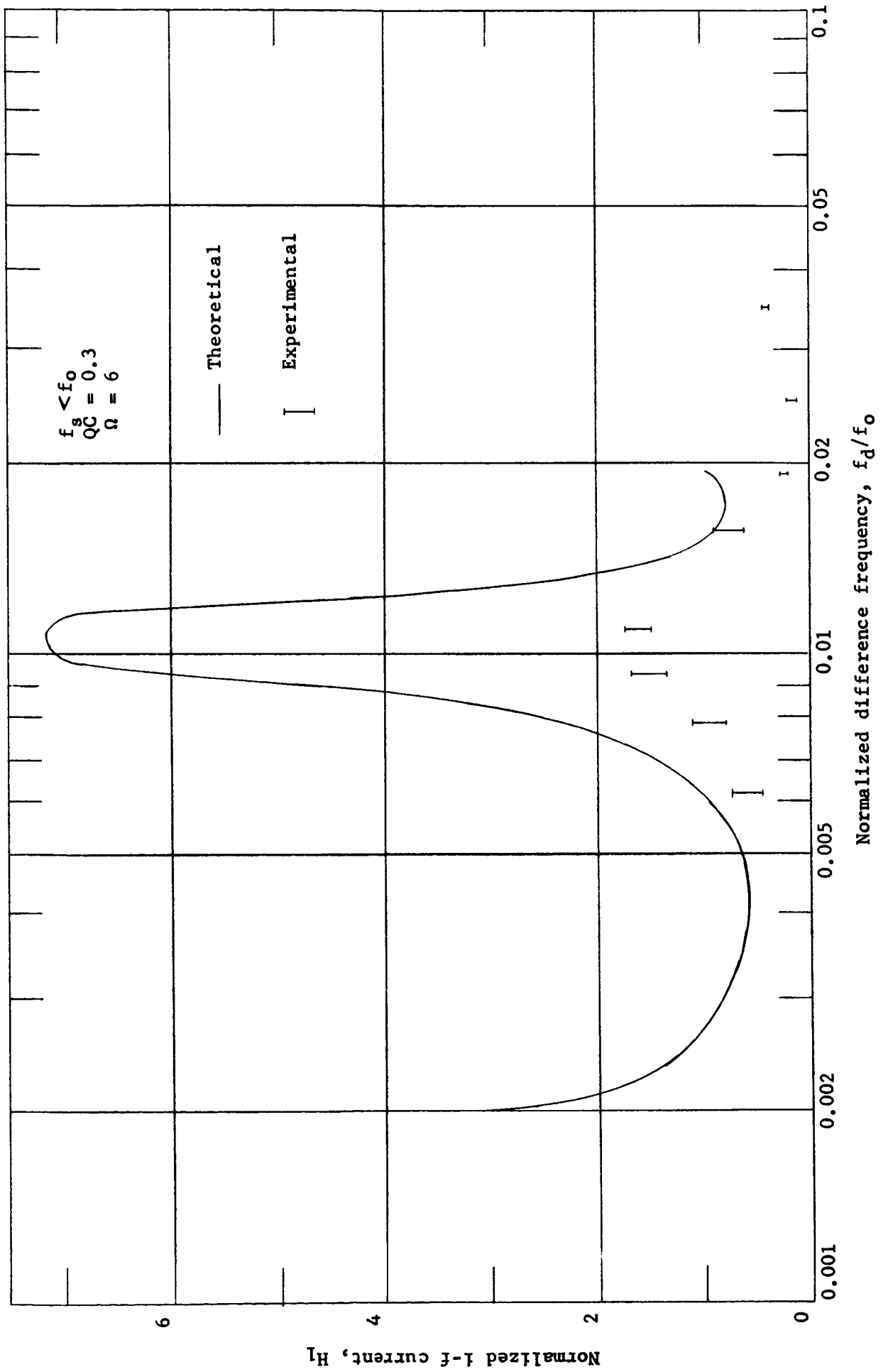
Figure 17. Comparison of theory with experiment for H_1 vs. f_d/f_o with $f_s < f_o$
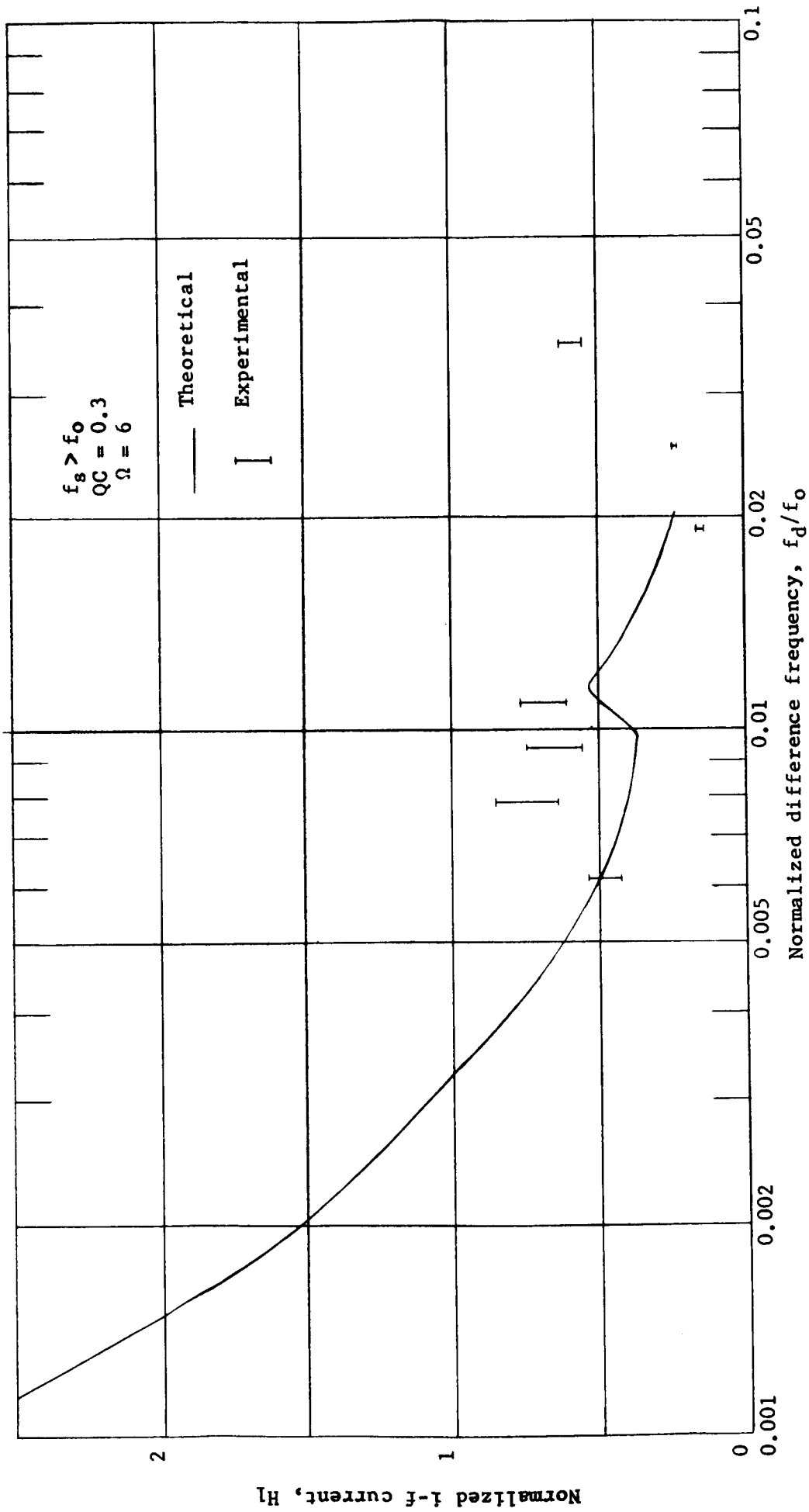
Figure 18. Comparison of theory with experiment for H_l vs. f_d/f_o with $f_s > f_o$

of H_1 occurs around 30 Mc/s for $f_s < f_o$ (Figure 17) and is about 1.7.
The data for this point indicate that R_L was 1.5 KΩ. Substituting
these values into Equation (2-9) results in a value of conversion gain
of -40 db.

2.4 Noise Theory

A consideration of the noise performance of backward-wave
converters was not required by the contract. However, it is an impor-
tant consideration to the overall performance of converters. A pre-
liminary discussion of noise was given in the final report on contract
NASw-430. The same noise model will be used here but we will carry
the derivation several steps further and find the noise figure of the
millimeter device used as an example at the end of Section 2.2.

Let N_s be the beam noise from the cathode at the signal fre-
quency, f_s, N_d be the beam noise from the cathode at the difference
frequency, f_d, and N_i be the standard input noise at the signal fre-
quency. Since the SCC does not have good image rejection, noise at
the image frequency, $2f_o - f_s$, must be considered. For reasonably low
values of f_d, this noise will be of the same order as the noise at f_s.
Thus, instead of N_s and N_i, we will consider $2N_s$ and $2N_i$.

The noise at the signal frequency (and image frequency),
$2N_s$ and $2N_o$ will appear at the output modified by the conversion gain
of the SCC, g_1. The i-f noise, N_d, will stream through unaffected by
the gain. Thus, the noise figure of the SCC, F_1, may be written

$$F_1 = (2N_s g_1 + 2N_i g_1 + N_d)/(2N_i g_1)$$

$$= 1 + N_s/N_i + N_d/(2N_i g_1) \qquad (2-17)$$

The first two terms of Equation (2-17) may be considered as the noise figure, F_A, of the device acting as an amplifier, that is,

$$F_1 = F_A + N_d/(2N_i g_1) \qquad (2\text{-}17a)$$

The noise at f_d essentially is shot noise and may be written as

$$N_d = \overline{i_{d1}^2} R_L \qquad (2\text{-}18)$$

where $\overline{i_{d1}^2}$ is given by van der Ziel[4] as

$$\overline{i_{d1}^2} = (0.644)(4)kT_c g_o \Delta f \qquad (2\text{-}19)$$

where k is Boltzmann's constant, T_c is the cathode temperature, g_o is the diode transconductance and Δf is the bandwidth. The standard noise input is

$$N_i = kT\Delta f \qquad (2\text{-}20)$$

where T is $270^\circ K$. Substituting Equations (2-18), (2-19), and (2-20) into Equation (2-17a) yields

$$F_1 = F_A + 1.29(T_c/T)(g_o R_L/g_1) \qquad (2\text{-}21)$$

Solving Equation (2-8) for R_L/g_1 and remembering that $g_o = (3/2)(I_o/V_{A1})$, where V_{A1} is the first anode voltage, Equation (2-21) may be written as

$$F_1 = F_A + 3.86(T_c/T)V_o/(V_{A1}CH_1^2) \qquad (2\text{-}21a)$$

If we add $T_c = 990^\circ C$ and $V_{A1} = 440$ v. to the values in the example at the end of section 2.2, we find that, even for noisy amplifiers, F_A is negligible compared to the last term of Equation (2-21a) and, for this example,

$$F_1 = 76 \text{ db}$$

It is possible to do better than this. For the S-band SCC of Section 2.3, $V_o = 450$ v., $V_{A1} = 20$ v., $C = 0.01$ and $H_1 \approx 2$ for $f_d \approx 30$ Mc/s (see Figure 17). With T_c still $990^\circ C$ and an amplifier noise figure, F_A, of 20 db

$$F_1 = 10^2 + 10^4 = 40 \text{ db}$$

Although the noise figure has improved significantly, it is still high enough so that the amplifier noise figure is unimportant to the overall noise figure.

3. TASK B

3.1 Introduction

Under contract NASw-430 many types of slow-wave structures were considered and an assessment made of their suitability for use in millimeter wave converters. The ridge loaded meander line and the Karp structure[5] were selected for special study because their constructional simplicity makes them particularly attractive for use at millimeter wavelengths. For each of these structures a Fletcher analysis[6] was carried out and a comprehensive set of computer results obtained. Measurements were made on cold-test models scaled up for operation in the 1500 Mc/s region and the results showed that the theory was capable of providing a reliable guide for the design of such structures. A comparison of dispersion and interaction impedance properties showed that the meander line has the advantage of broad bandwidth and reasonably constant impedance over the band. The Karp structure can have higher impedances but usually only over a relatively narrow band.

The planar stub-supported meander line was first analyzed by Ash and Studd[7] and it was shown that the structure is particularly suitable for wide band backward-wave applications. When the stucture is loaded with a conducting ridge the pass band is further increased but with a reduction in the interaction impedance. The analysis of the ridge loaded structure was presented in the 1st bi-monthly report of NASw-430 and a large number of design curves were given in the 2nd bi-monthly report.

For a given current density a strip beam seems the obvious choice for a tube employing the planar meander line. However, strip

beams are difficult to produce and it was suggested that advantage may
be taken of the advanced technology of circular beams by modifying the
planar meander line to provide a cylindrical beam tunnel.

Figure 19 (also see Type III, Figure 2) shows the basic modi-
fication to the planar meander line which makes it suitable for use
with a cylindrical electron beam. If the diameter of the beam tunnel
is small this modification does not have any marked effect on the cir-
cuit characteristics. (It should be noted that if the tunnel diameter
is made equal to the link separation the structure becomes the well
known stub-supported ring and bar structure.) A limiting case that
has been considered in some detail is that where the tunnel diameter
equals the bar length and is shown in Figures 20 - 22 (also see Type I,
Figure 2). Measurements were made on this structure during the earlier
stages of the contract when the possibilities of using a hollow beam
were being explored. It was found that the structure possesses a
strong anti-symmetric mode. Suitably placed absorbing strips may be
used to suppress this mode. This work was discontinued after the de-
cision to use a solid circular beam was made (see Section 4).

Two other structures suitable for solid beams were investi-
gated and are shown in Figures 23 and 24 (also see Type II and Type IV,
Figure 2). The latter structure (Type IV) can be fabricated from a
single sheet, thus easing constructional problems.

The detailed analysis of the various circular forms of meander
line would be prohibitively difficult and was not attempted. The theo-
retical results for the plane circuit were used as a guide to the initial
design work in the hope that the modifications to circular form would
not greatly change the characteristics.
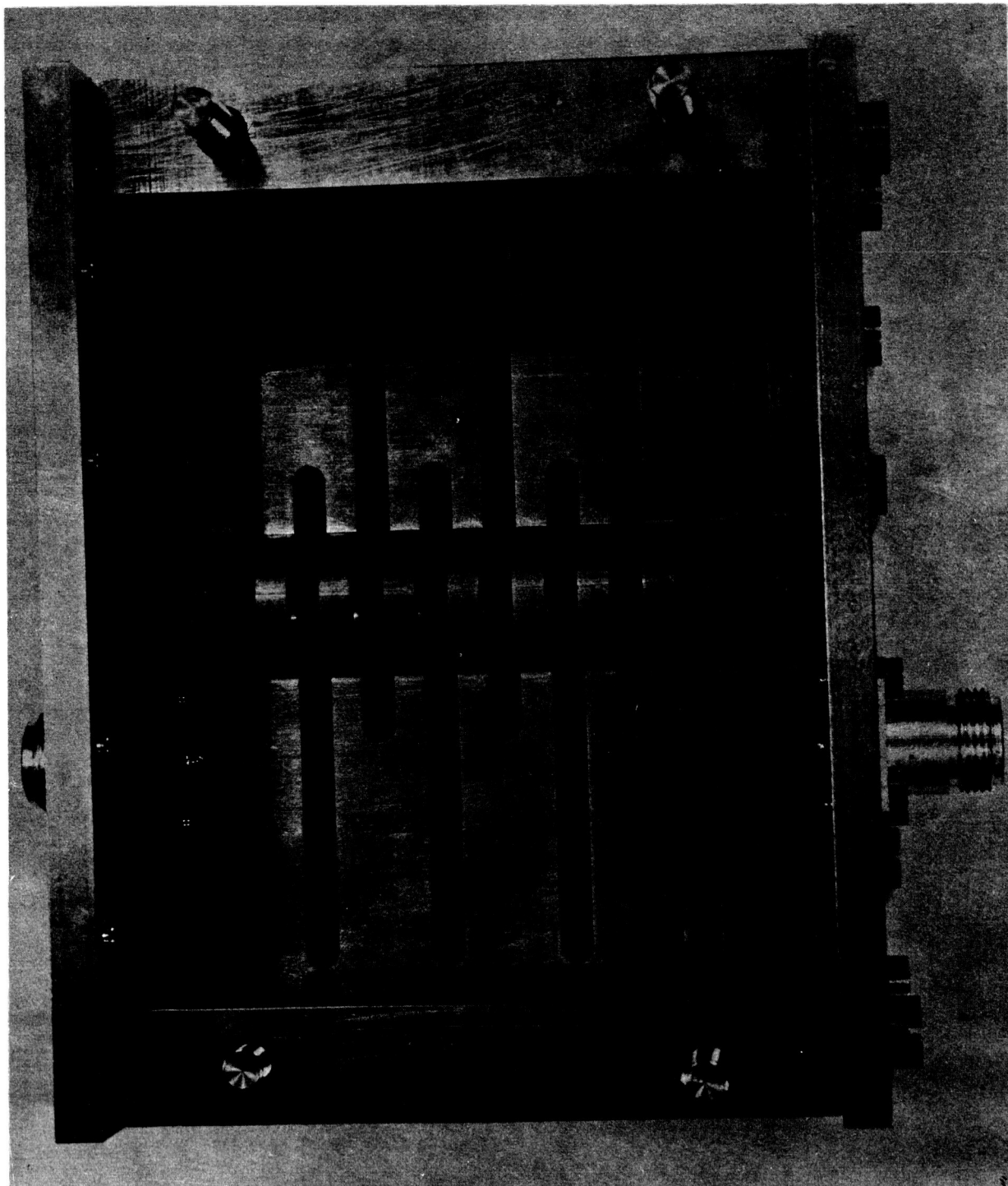
Figure 19. Type III cylindrical meander line in resonant circuit
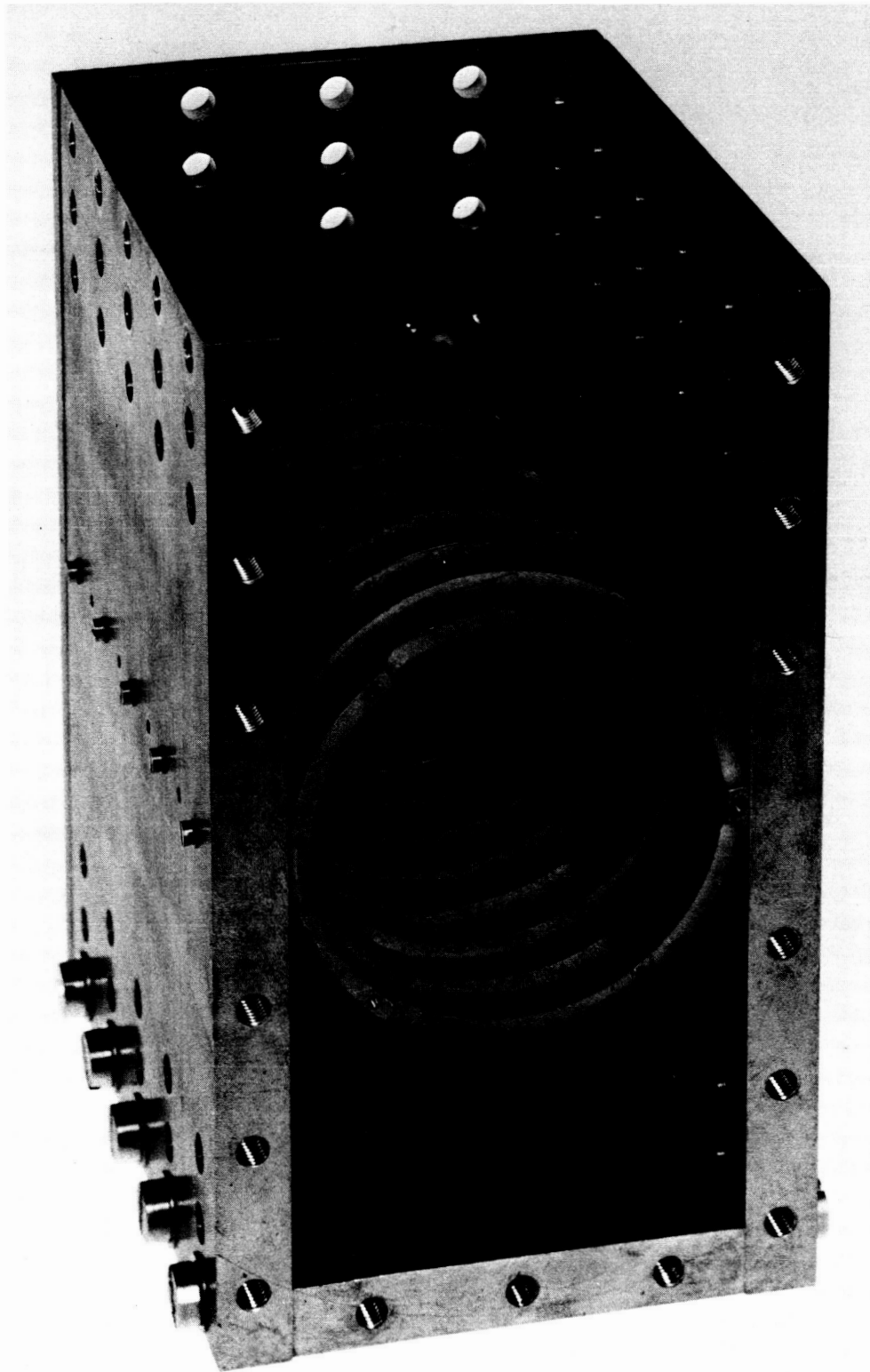
Figure 20. Type I cylindrical meander line in resonant circuit
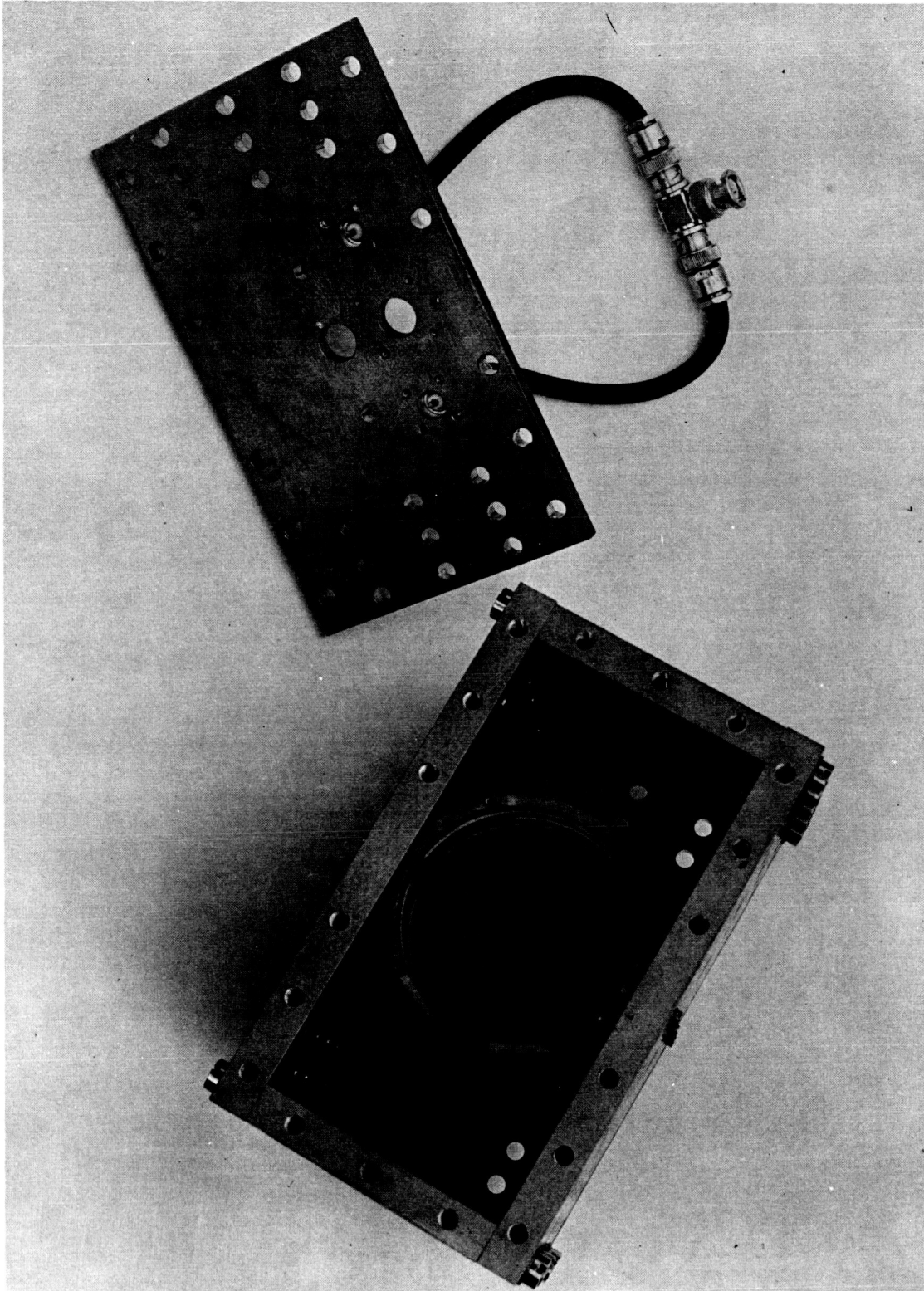
Figure 21. Type I cylindrical meander line in resonant circuit with input end plate shown
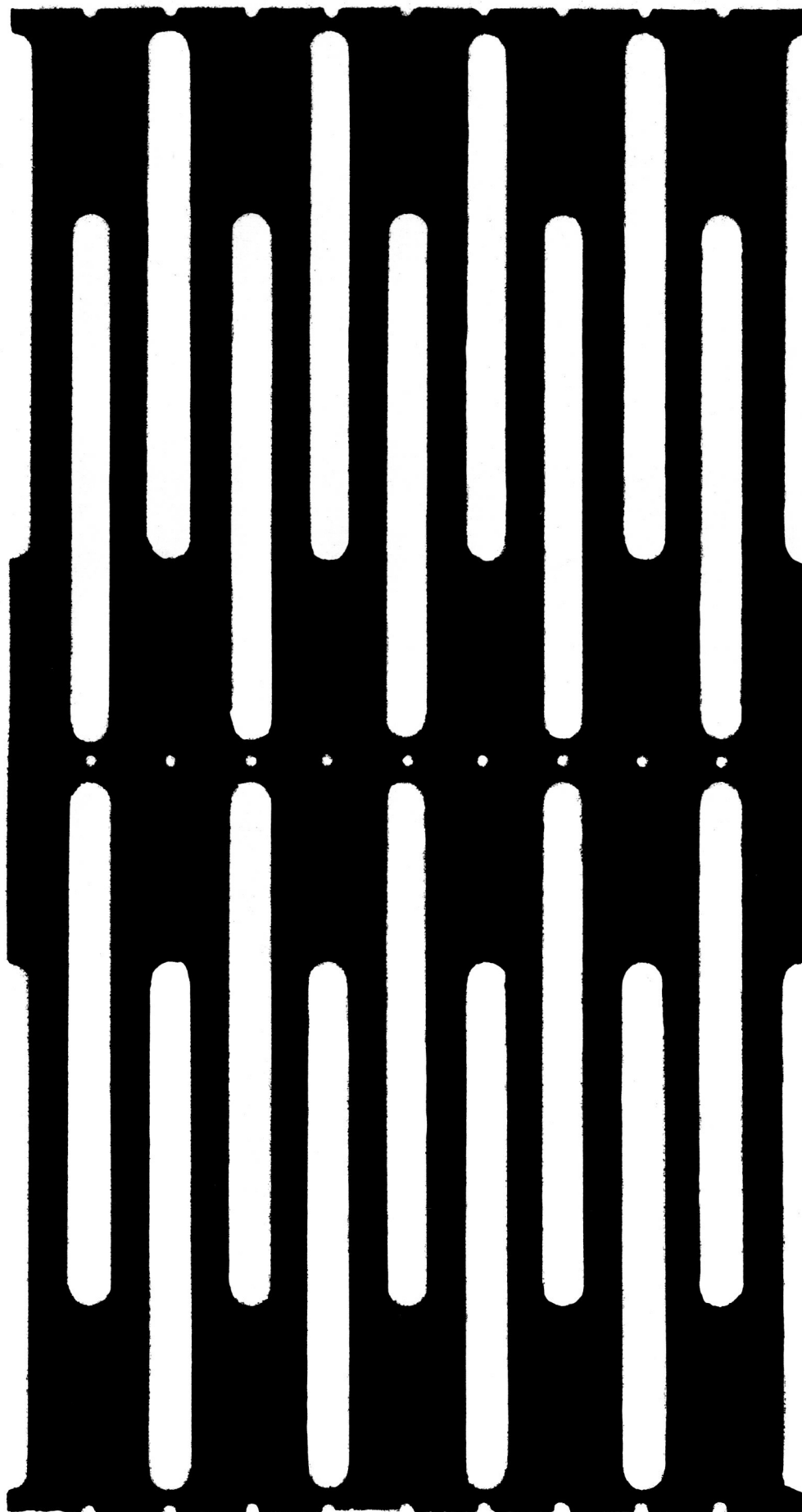
Figure 22. Developed view of Type I meander line
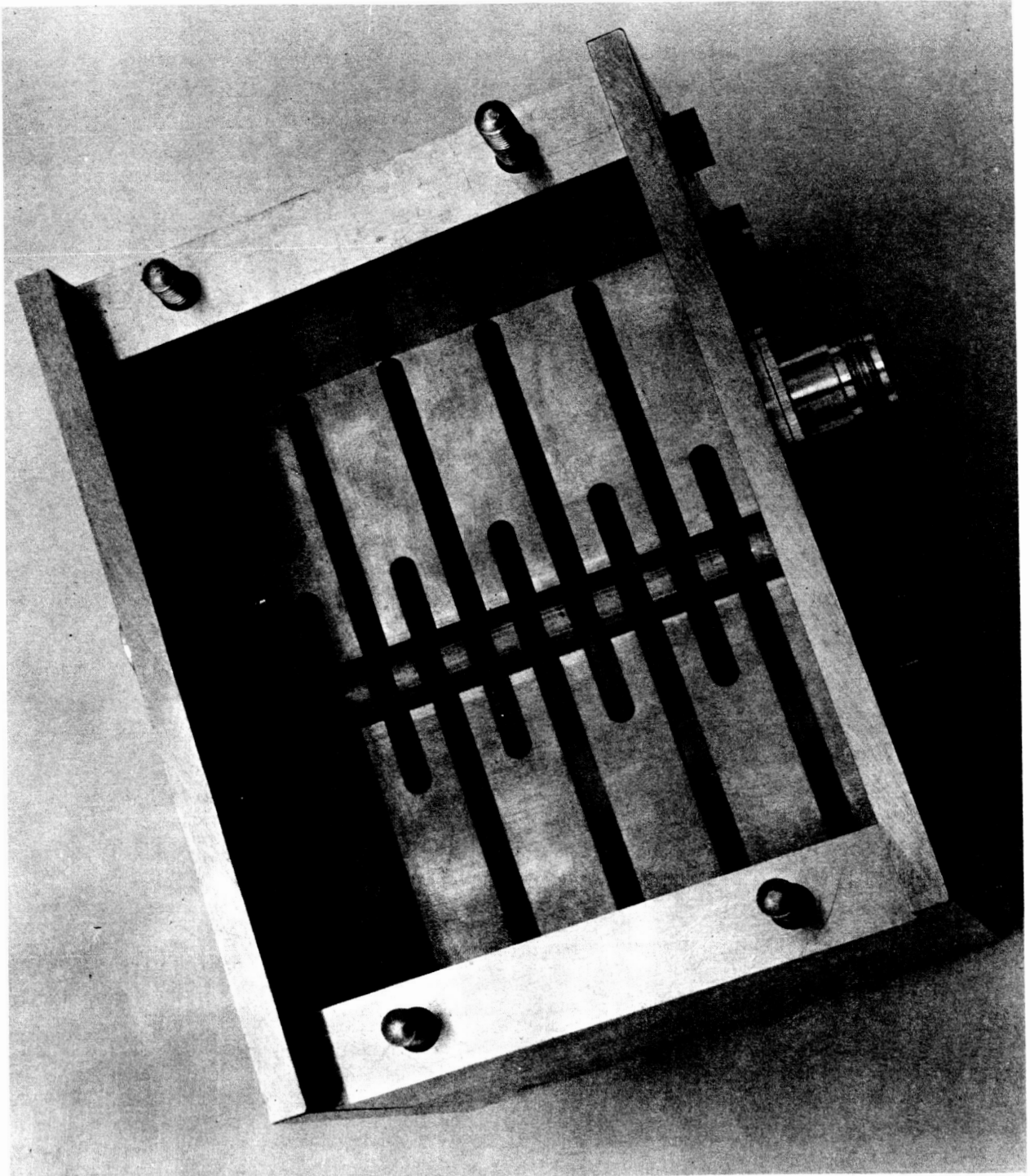
Figure 23. Type II cylindrical meander line in resonant circuit
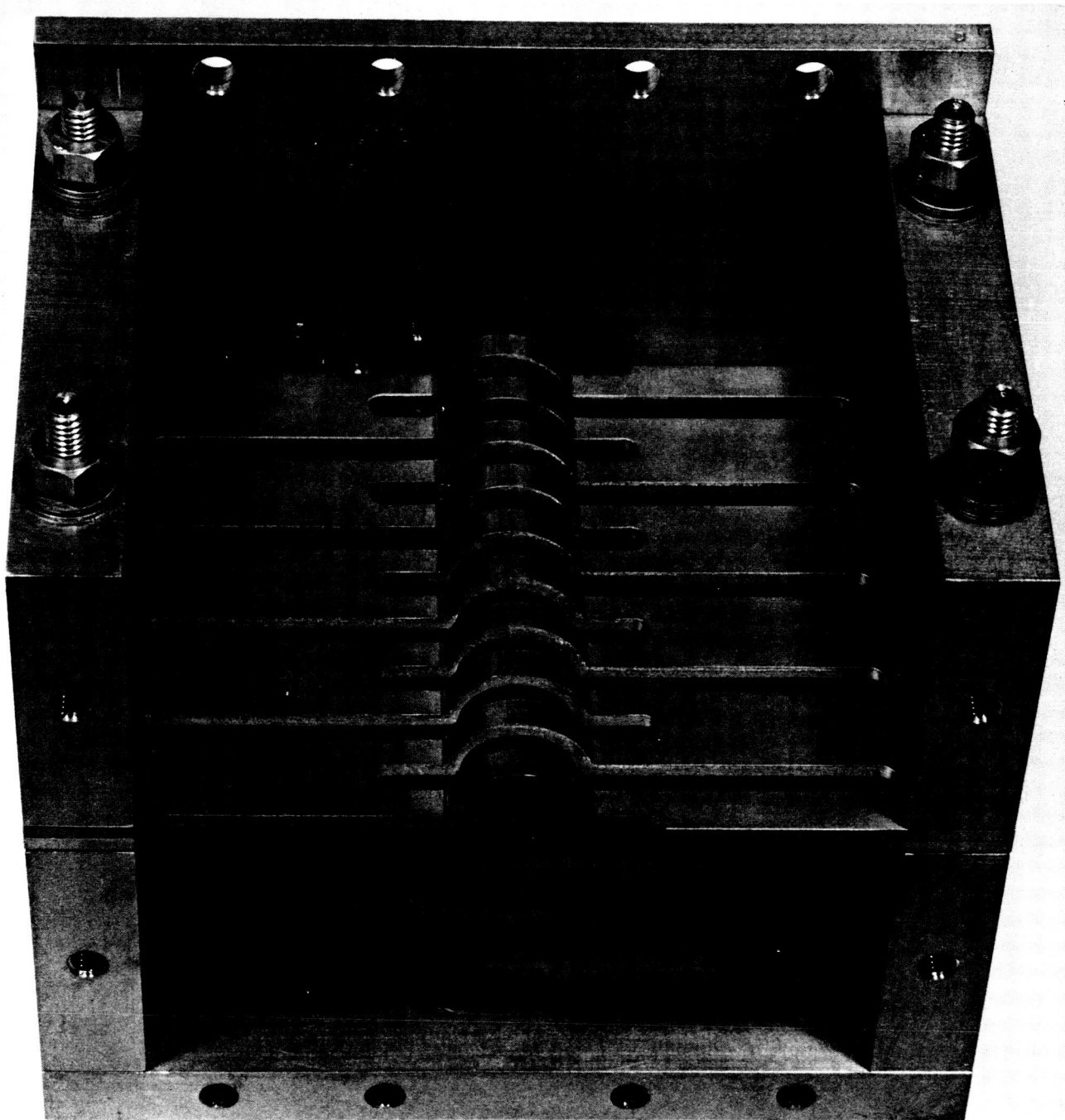
Figure 24. Type IV (semi-) cylindrical meander line in resonant circuit

The experimental program has consisted of measurements of dispersion and interaction impedance on large scale models of the various structures. The frequency range chosen was L-band (1 - 2 Gc/s). In addition, a detailed experimental study of methods to suppress the anti-symmetric mode in the Type I structure was made. These experiments were performed in S-band (2 - 4 Gc/s).

3.2 Dispersion and Impedance of Four Modified Meander Line Circuits

For determining the dispersion and interaction impedance of the modified meander line circuits, the resonance method was chosen as being the most simple and reliable. The techniques involved have been in use for a considerable time but a study of the literature suggested that so far only superficial attention has been given to assessing the limitations and accuracy of the method. A thorough theoretical study therefore was made of the factors which limit the application and affect the accuracy of this method, such as the size and dielectric constant of the perturbing element, the presence of more than one space harmonic, the presence of transverse fields, etc. This work, together with a full description of the method of measurement is presented in this section.

The four circuits studied have been labeled, for convenience, Types I, II, III and IV. Type I (Figures 20 - 22) consists of two plane meander lines joined together side by side (Figure 22) and then rolled up into a cylinder. This circuit, therefore, effectively consists of two separate lines in parallel and thus needs two input and two output couplings. The next two circuits, Type II (Figure 23) and Type III (Figure 20) are similar. In both, a plane circuit is distorted

at the center to provide a circular beam tunnel, but Type III has the beam hole radius twice that of Type II; both have bars with the same electrical length. The fourth circuit, Type IV (Figure 24) is made by cutting the circuit, Type III, in half along its mid-plane.

All circuits were ten bars long and were shorted at each end by conducting plates placed at mid-slot positions. These shorting plates, together with the side and end walls, totally enclose the circuits, forming resonators. The input and output couplers consisted of capacity probes entering through the shorting plates in the plane of the circuit.

Experience has shown the importance of having accurately machined circuits mounted in a solidly made resonator with accurately fitting joints. All these circuits were machined to 0.002 inch tolerances from a very stable (in dimensions) steel. The circuits were gold plated to reduce losses. For each resonator, a slot was cut along the length of one wall to allow entry of a resistive probe to scan the standing-wave.

3.2.1 Dispersion Characteristics

In designing a slow-wave circuit, it is necessary to have information about its propagation characteristics. These can be obtained from the dispersion curve, that is, the plot of f' as a function of (θ/π) where θ is the phase shift per bar, $f' = f_r/f_o$, $f_o = c/(4b)$, f_r is the resonant frequency and c is the speed of light in vacuo. The definitions of b and the other meander line dimensions are shown in Figure 25. For a plane symmetrical meander line, the theoretical dispersion equation can be written as[7]

$$x/\tau^2 + T/t = 0 \qquad\qquad (3-1)$$
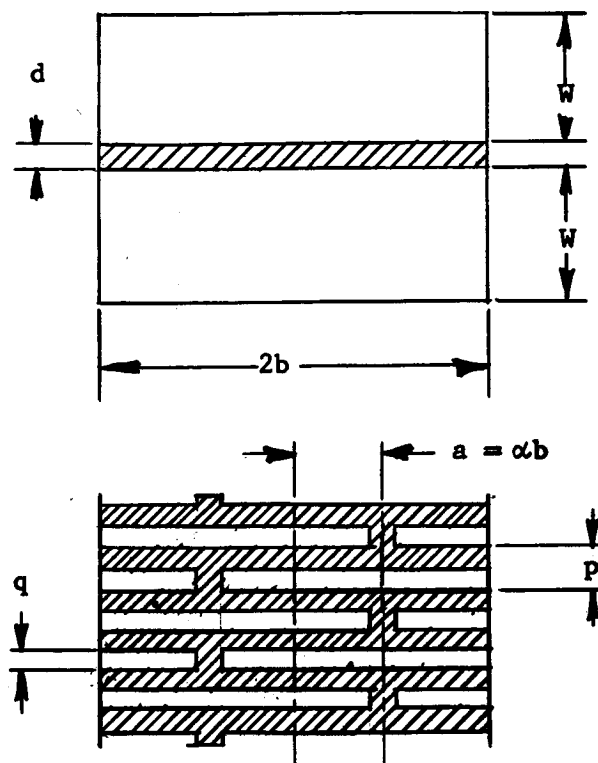
Figure 25. Definition of meander line dimensions.

where

$$x = Y(\theta)/Y(\theta + \pi)$$

$$\tau = \tan(\theta/2)$$

$$T = \tan \phi_b \ , \quad t = \tan \phi_a$$

$$\phi_b = 2\pi b/\lambda_o \ , \quad \phi_a = 2\pi a/\lambda_o$$

and $Y(\theta)$ is the Fletcher admittance function[6]. Equation (3-1) is obtained using the approximate method introduced by Fletcher which is based on assumed TEM propagation along the bars.

The dispersion curve for a circuit may be obtained by short circuiting the structure at two of its transverse planes of symmetry, and exciting the short circuited length of the structure as a cavity. Resonances exist for frequencies at which the waves associated with the circuit reflect in the short circuits to form standing waves, that is, at resonance $L/N = \lambda/2$, where L is the length of the circuit and N is the number of half wave lengths along the circuit.

The circuits are shown with the couplings in place (Figures 19 - 21, 23 and 24). The type and position of the coupling should be selected so as to couple to the slow wave rather than the fast wave. A very tight coupling is undesirable since it tends to couple to the fast wave, and also tends to pull the resonance frequency. At the resonance frequency the number of half wave lengths along the structure is counted by moving a lossy probe along the circuit and noting the number of maxima or minima on the output meter; in a plane where the transverse E field vanishes the lossy probe contributes negligible loss, whereas the loss is relatively high when the probe is at a maximum of the standing wave. For a ten-bar circuit the resonances occur at 0.1 (θ/π), 0.2 (θ/π), 0.3 (θ/π), ...(θ/π). Thus ten points on the dispersion curve may be obtained.

The experimental set up is shown in Figure 26. The method used for determining N, and f_r was as follows: the pass-band was scanned noting all but the very weak resonances. This gave an idea of the resonances which merited further exploration. Each resonance was then examined separately; the procedure adopted is given below.
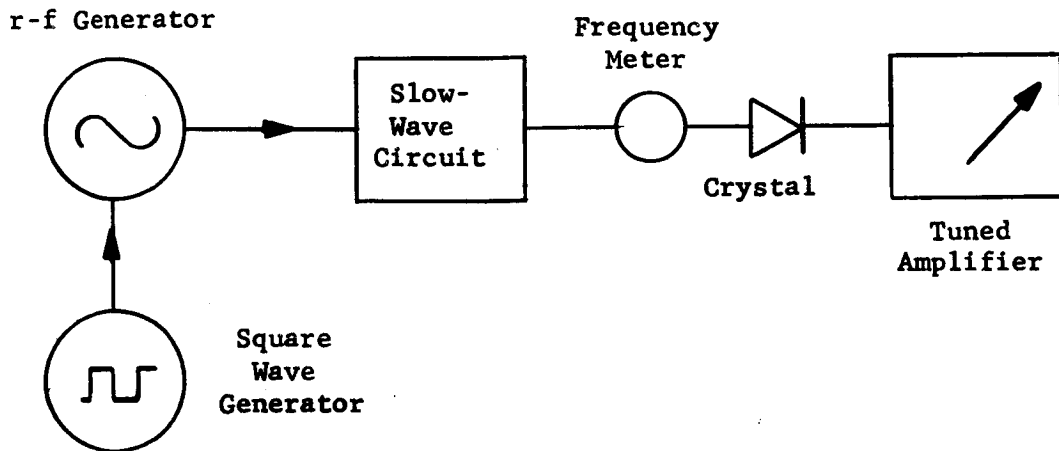
Figure 26. Experimental set up for dispersion measurements.

1. The perturbing dielectric rod was inserted through the beam holes to extend along the whole length of the circuit. With the perturbing rod in position the signal frequency was varied until the power transmitted through the circuit was a maximum. The resonance frequency f_r, corresponding to N was noted.

2. The dielectric rod was then withdrawn and the frequency was altered to obtain the same resonance N again, corresponding to a new frequency f_r'.

3. The number of half wavelengths along the circuit was counted.

This procedure was repeated for all the resonances, noting down N, f_r and $\Delta f_r = (f_r' - f_r)$ for each resonance. The resonances thus obtained were not all true resonances. But the spurious resonances could be recognized since they were usually much weaker than the true resonances and radiated more strongly. This will, for instance, be so

if the spurious resonance is due to a fast wave. The spurious reson-
ances invariably had small or zero frequency shift when perturbed.

For counting N the probe should be large enough to separate
the maxima and minima of the standing wave clearly, but not so large
as to spoil the resolution. In general the width in the axial direc-
tion should not be more than a quarter of the bar-pitch. The probe
should be moved along the circuit such that it attenuates the funda-
mental space harmonic more than the other harmonics; this can be
achieved by investigating the standing wave pattern. For these experi-
ments two probes were tried, one was made from aquadag-coated paper and
the other from a soft pencil lead. The use of the latter improved the
resolution.

It was found difficult, at times impossible, to count N at
the top end of the band. For the first six or seven resonances the
standing wave pattern was clear. At the top end of the band, however,
the pattern became very vague and it was not always possible to count
N with certainty. This was thought to be due to interference from the
-2 harmonic.

3.2.2 Interaction Impedance

Pierce[8] defined the interaction impedance for the nth space
harmonic as

$$K_n = E_n^2/2\beta_n^2 P \tag{3-2}$$

where, for the nth harmonic, E_n is the amplitude of the longitudinal
electric field, β_n is the phase change constant, and P is the power
flow down the circuit. K_n may be determined by use of zero-order
perturbation theory for a cavity. For a vanishingly small dielectric

perturbation to a cavity, Slater's perturbation theorem[9] can be written as[10]

$$\Delta f_r / f_r = - \Delta W / W \qquad (3\text{-}3)$$

where f_r is the resonance frequency, W is the total energy stored in the cavity, and Δf_r and ΔW are the increments of these quantities due to perturbation. The following assumptions are made:

1. The fields in the cavity are not changed by the introduction of the dielectric,

2. The only fields existing within the dielectric are those of the space harmonic under consideration, and

3. The transverse E-fields are vanishingly small inside the dielectric.

Assumptions (1) and (3) are reasonable if the perturbing dielectric is sufficiently thin. Assumption (2) is justified by the fact that the odd space-harmonic fields vanish on the axis of the meander line circuit, and the higher order even space harmonics are generally much weaker than the fundamental harmonic.

Let A be the cross sectional area of the dielectric cylinder, λ_g the wavelength of the fundamental harmonic, and W the stored energy per half wavelength of the cavity. When the dielectric cylinder is inserted in the cavity, there is additional stored energy, ΔW, given by

$$\Delta W = (1/4)\epsilon_o (\epsilon_r - 1) A (\lambda_g / 2)(E_{oc}{}^2 / 2) \qquad (3\text{-}4)$$

where ϵ_r is the relative dielectric constant of the perturbing dielectric. The standing wave pattern comprises two traveling-waves of amplitude $E_o (= E_{oc} / 2)$, each wave contributing a stored energy of

W/2 per half wavelength of the circuit. Therefore

$$P = (W/2)v_g(2/\lambda_g) = Wv_g/\lambda_g \tag{3-5}$$

where v_g is the group velocity.

From Equations (3-3), (3-4), and (3-5) we have

$$\Delta f_r/f_r = -(E_o^2/2P)\left[\epsilon_o(\epsilon_r-1)/2\right]Av_g \tag{3-6}$$

But from Equation (3-2) the impedance for the fundamental harmonic is

$$K_o = E_o^2/(2P\beta_o^2)$$

Therefore, substituting for $(E_o^2/2P)$ from Equation (3-6), we have

$$K_o = (2\Delta f_r/f_r)\left[\epsilon_o(\epsilon_r-1)A\beta_o^2 v_g\right]^{-1} \tag{3-7}$$

Now, $v_g = c(\lambda_g/\lambda_o)^2 (d\lambda_o/d\lambda_g)$ and $\beta_o = 2\pi/\lambda_g$, therefore

$$K_o = 2(\lambda_o/2\pi)^2(\Delta f_r/f_r)(d\lambda_g/d\lambda_o)\left[cA\epsilon_o(\epsilon_r-1)\right]^{-1} \tag{3-8}$$

Equation (3-8) gives the interaction impedance of a circuit at the center for the fundamental harmonic. We now proceed to change the variable $(d\lambda_g/d\lambda_o)$ in the equation to one that may be directly obtained in an experiment. By the chain rule

$$d\lambda_g/d\lambda_o = (d\lambda_g/df_r)(df_r/d\lambda_o) = (d\lambda_g/dN)(dN/df_r)(df_r/d\lambda_o) \tag{3-9}$$

But, since $f_r = c/\lambda_o$ and $\lambda_g = 2L/N$, where L is the length of the circuit

$$df_r/d\lambda_o = -c/\lambda_o^2$$

and

$$d\lambda_g/dN = -2L/N^2$$

Substitution of these two equations into Equation (3-9) yields

$$d\lambda_g/d\lambda_o = (2L/cN^2)f_r^2(dN/df_r)$$

Thus Equation (3-8) may be written

$$K_o = L \left[\pi^2 A N^2 \epsilon_o (\epsilon_r - 1)\right]^{-1} (dN/df_r)(\Delta f_r/f_r) \qquad (3-10)$$

Equation (3-10) gives the impedance of a circuit for the fundamental space harmonic at the perturbation. It assumes that there is no interference from other harmonics, and that the field at the center of the circuit is not affected when the dielectric is inserted. This is, of course, an ideal situation. The higher order space harmonics do interfere with the fundamental harmonic, and the perturbing dielectric invariably modifies the fields at the center of the circuit. This value of K_o must therefore be corrected for both these effects. Two factors, F and G, are determined such that the corrected value of K_o results when the uncorrected value of K_o is multiplied by the ratio of F to G, that is,

$$K_o(\text{corrected}) = K_o(\text{uncorrected})(F/G) \qquad (3-11)$$

The factor F allows for error due to the modification of the fields in the presence of a perturbing dielectric; the factor G allows for interference from the second largest harmonic.

For the special case of a circular dielectric cylinder of radius b, along the axis of a circular cylindrical structure of radius a, Lagerstrom[11] has calculated the factor F to be

$$F = \gamma b K_o(\gamma b) + (1/2)(\gamma b)^2 \epsilon_r I_o(\gamma b) \left[K_o(\gamma b)/I_o(\gamma b) - K_o(\gamma a)/I_o(\gamma a)\right] \qquad (3-12)$$

where

$$\gamma^2 = \beta^2 - \omega^2/c^2 = \beta^2 - (2\pi f_r/c)^2$$

and $I_0(x)$ and $K_0(x)$ are the zero order modified Bessel functions of the argument x of the first and second kinds respectively.

The factor G is derived in Appendix C to be

$$G = 1 + \left[S_{o,n} F_n(y)/F_o(y) \right]^2 \qquad (3\text{-}13)$$

where $S_{o,n}$ is the ratio of $E_{z,n}$ to $E_{z,o}$ at the surface of the bars, n denotes the second largest harmonic, that is, the interfering harmonic, $F_o^2(y)$ and $F_n^2(y)$ are the impedance transformation factors for the fundamental and the nth harmonic respectively, that is,

$$F_n^2(y) = K_n(y)/K_n(0)$$

and y is the distance measured from the bars. For the meander line circuit, rolled or plane, the interfering harmonic is the -2 space harmonic and

$$S_{o,-2} = -\left[\theta/(2\pi-\theta) \right] \cot(\theta/4) \qquad (3\text{-}14)$$

which is derived from approximate field analysis of a plane meander line (Appendix C).

The factor $F_n^2(y)$ is evaluated in Appendix D. $F_n^2(y)$ is a _spatial_ transformation factor but also needed is a _space harmonic_ transformation factor. The fundamental space harmonic impedance is the quantity that is measured while the -2 space harmonic impedance is the quantity that is required for evaluation of these circuits as backward-wave devices. The evaluation of this latter factor is also given in

Appendix D.

To evaluate K_o by Equation (3-8), we must obtain the recip-

rocal of the slope of the dispersion curve for each value of N. We

must also measure the resonance frequency, N and Δf_r corresponding to

each resonance. The experimental set up for measuring N and Δf_r is

shown in Figure 27. The frequency shift due to the perturbation can
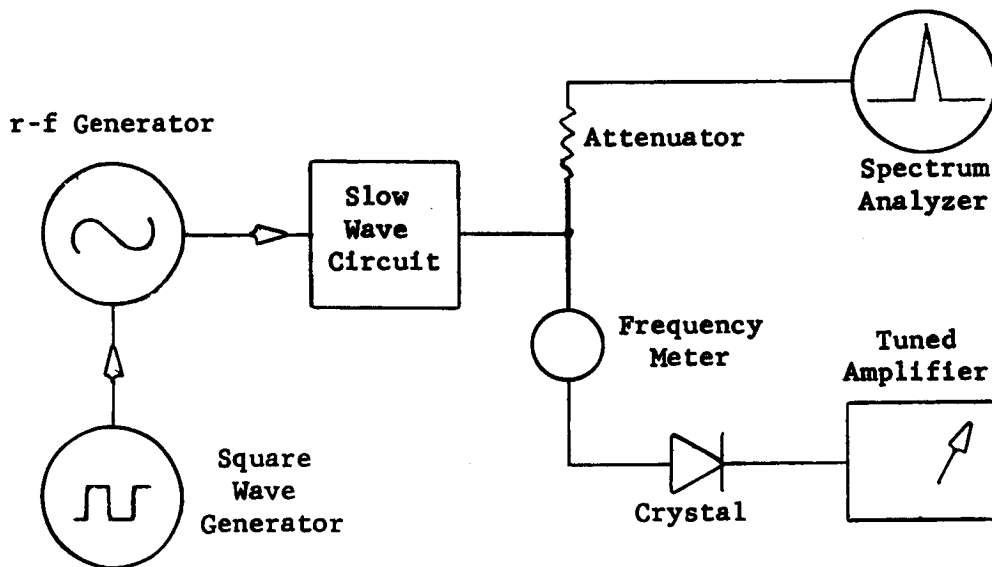
Figure 27. Experimental set up for impedance measurements.

be measured on a spectrum analyzer or on the frequency meter. The

values of K_o calculated by Equation (3-8) must be corrected for har-

monic interference and for the effect of introducing the dielectric -

unless the dielectric is very thin, in which case the error is

negligible.

All circuits except that with the very large diameter

(Type I) are suitable for use with solid cylindrical beams and for

these circuits the perturbing rod was placed along the axis and all impedances are given at this position. The large circuit would probably employ a hollow beam passing close to the structure and in order to perturb it symmetrically, two dielectric rods were placed near the circuit and diametrically opposite each other. In this circuit the impedance at the bars is of more interest than that on the axis.

3.2.3 Experimental Results

Figure 28 shows the dispersion curves for meander line Type I, driven in phase and in anti-phase. The two curves differ slightly at the bottom end but are very similar for the top half of the band. Figures 31, 33 and 35 show dispersion curves for meander lines Type II, III and IV respectively, and finally in Figure 37 dispersion curves for all circuits are shown together with the theoretical curve for the plane meander line.[+] There is reasonably close agreement between all the curves in the lower half of the band but towards the upper cut-off there are some differences. In particular, the slope of the theoretical curve is much higher than that for any of the measured curves.

The interaction impedance curves are obtained by plotting impedance K_n, normalized with respect to the impedance of free space, Z_o, as a function of the phase shift per bar, θ, normalized with respect to π. The interaction impedance curves for meander line Type I calculated for the surface of the bars at the midpoint of their length are shown in Figures 29 and 30. Figures 32 and 34 show the fundamental

[+]For all theoretical curves presented in this section, d/q (see Figure 25) has been taken as the ratio of bar thickness to gap width at the circumference of the circular section of the circuits.
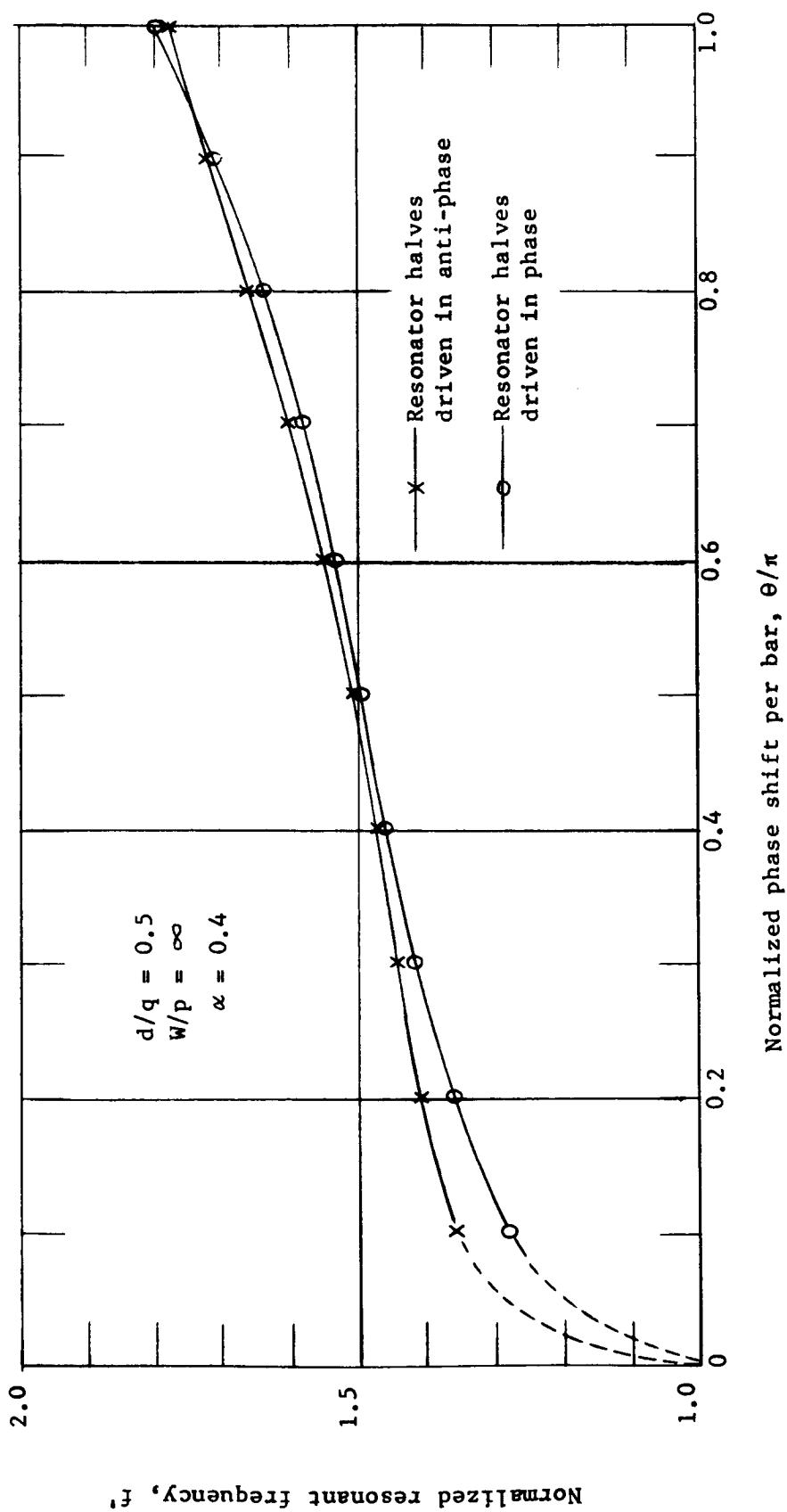
Figure 28. Dispersion characteristics of meander line Type I
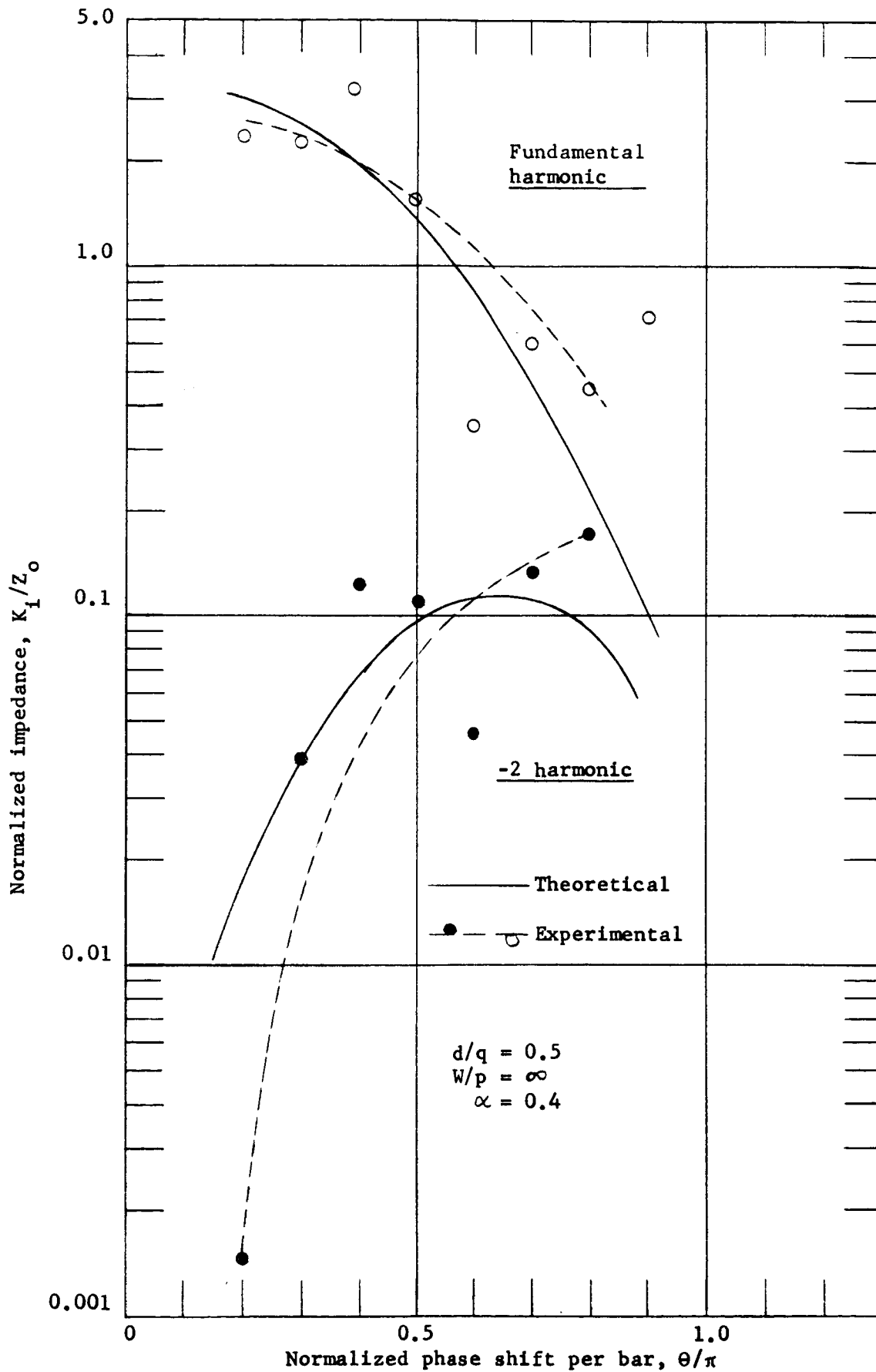
Figure 29. Interaction impedance at the bars of meander line Type I (anti-phase)
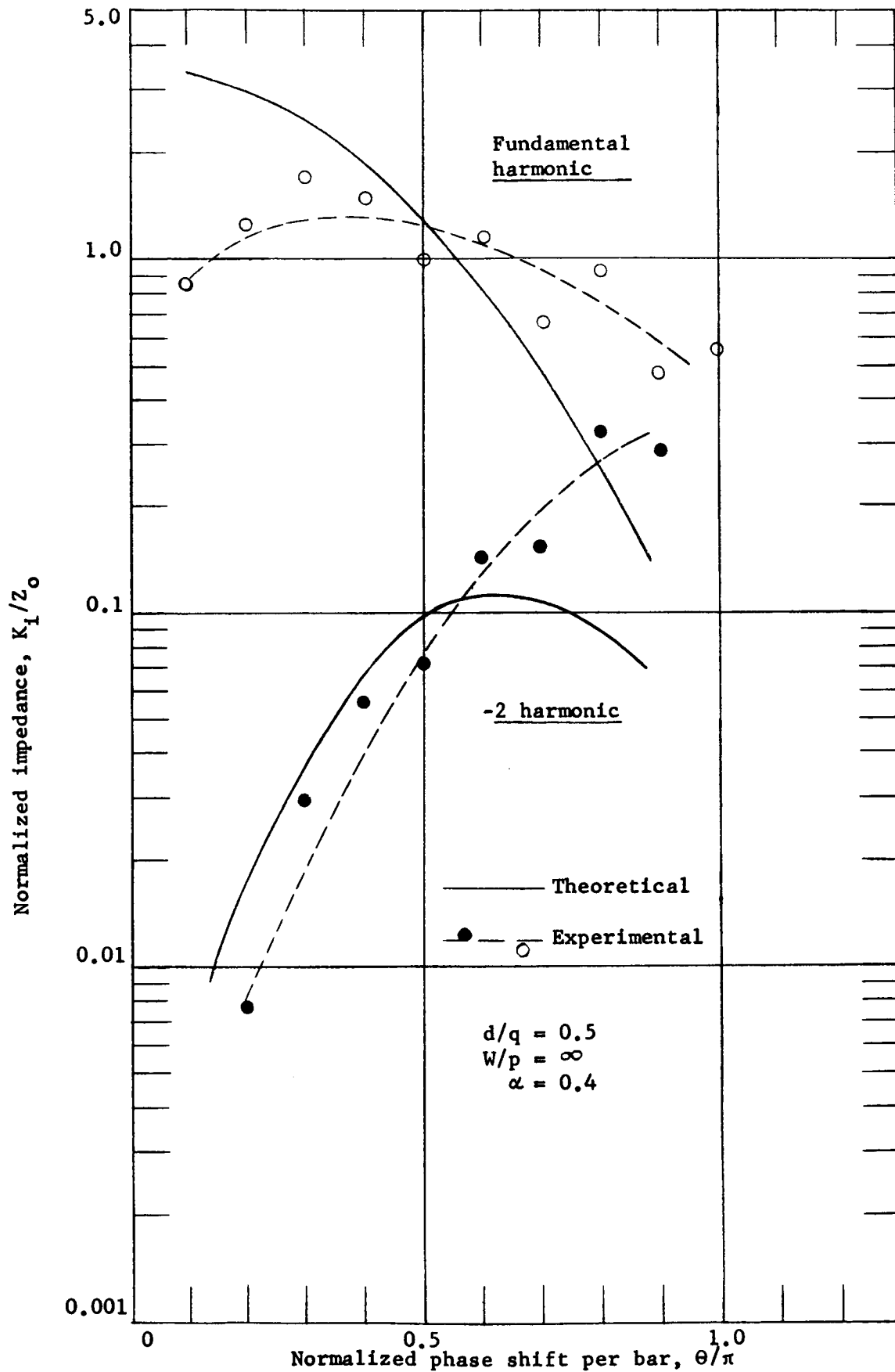
Figure 30. Interaction impedance at the bars of meander line Type I (in phase)
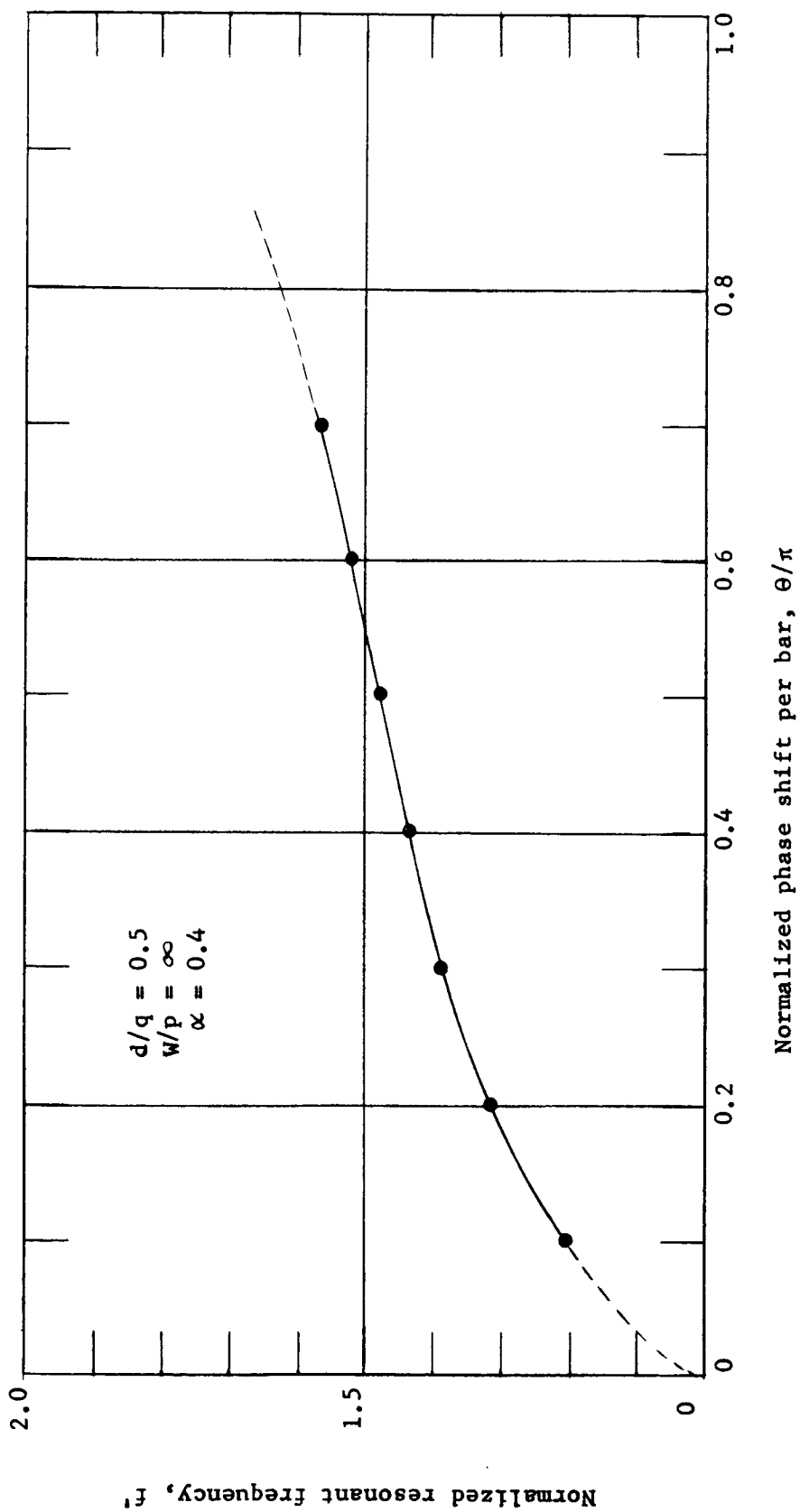
Figure 31. Dispersion characteristic of meander line Type II
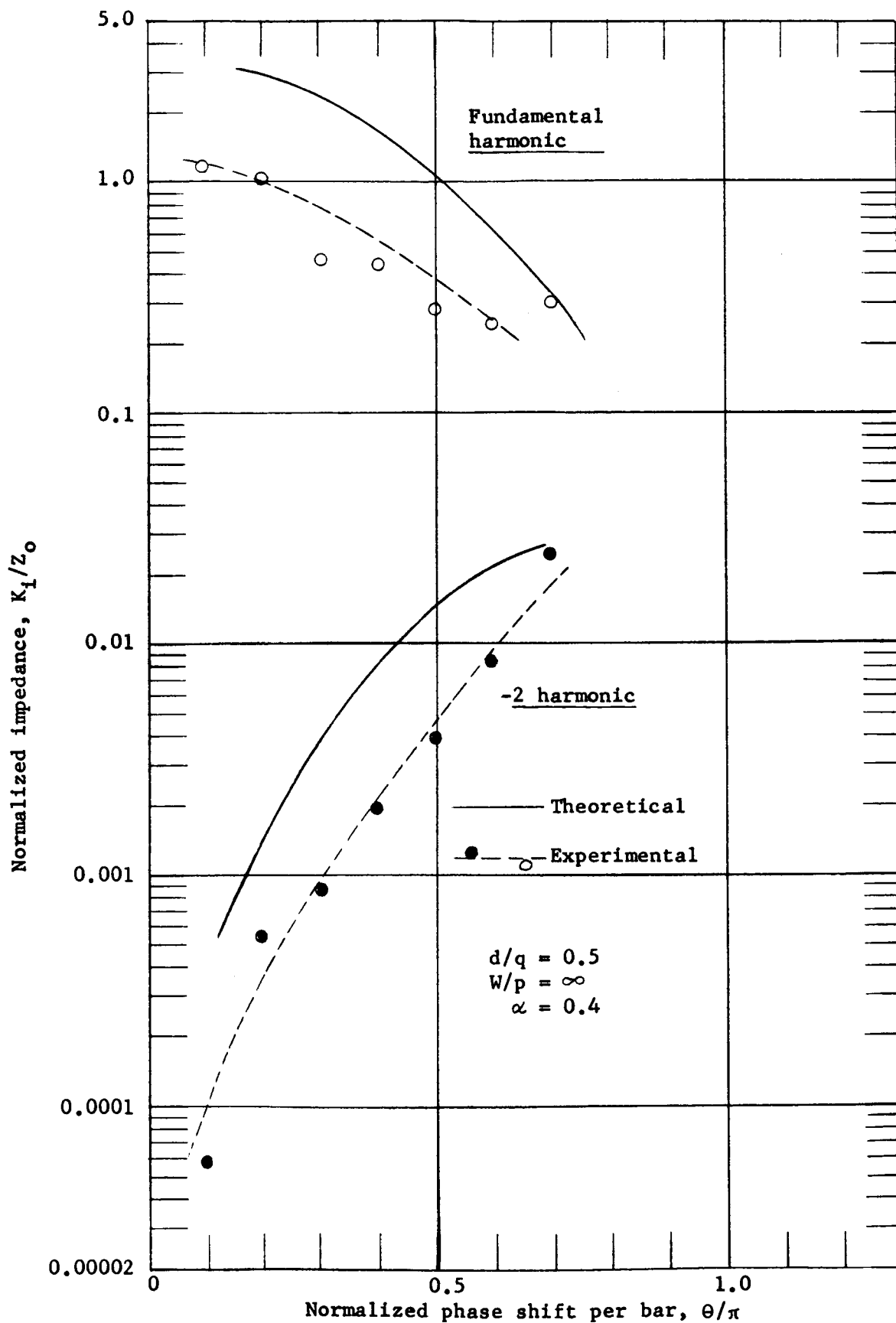
Figure 32. Interaction impedance on the axis of meander line Type II
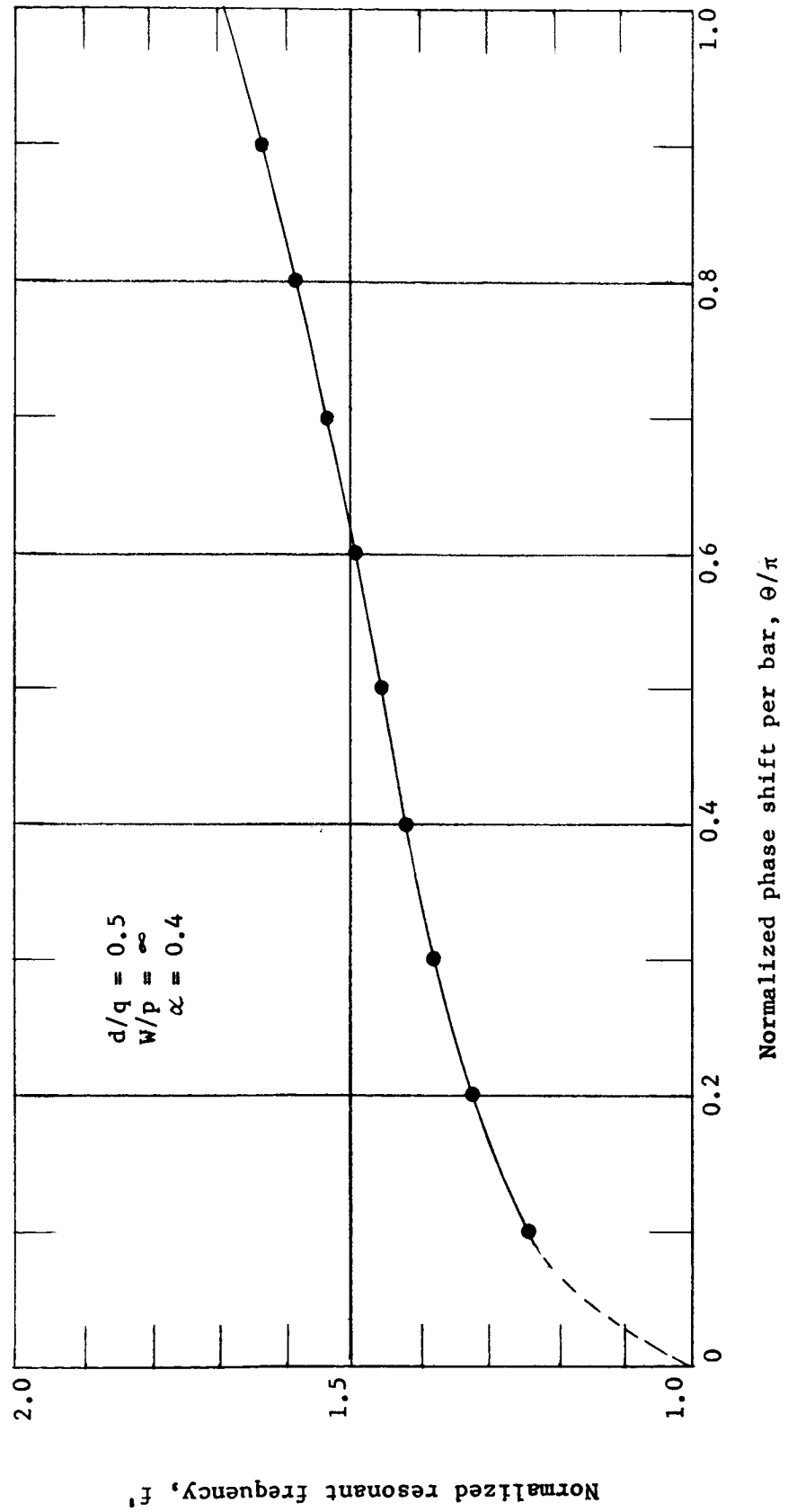
Figure 33. Dispersion characteristic of meander line Type III
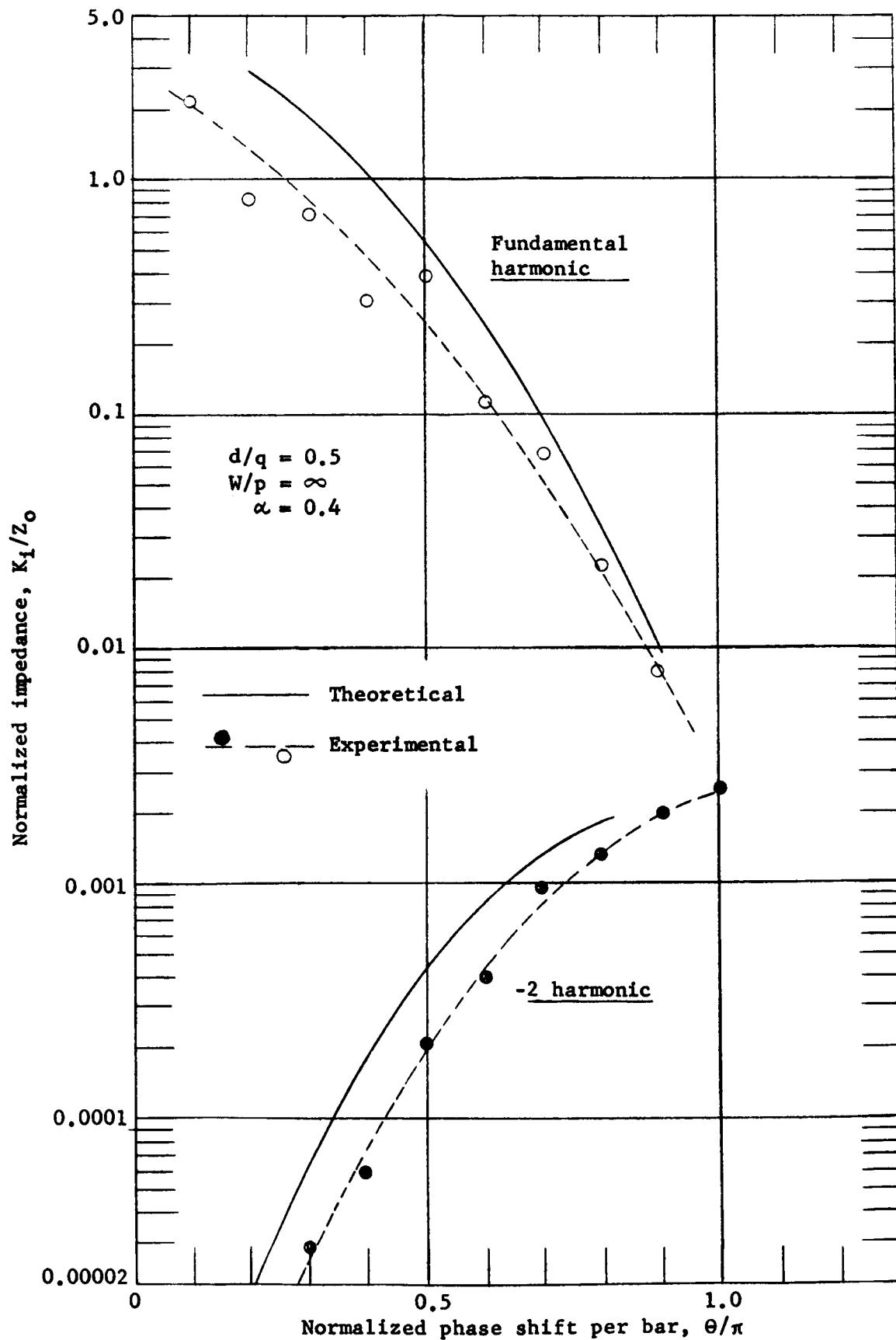
Figure 34. Interaction impedance on the axis of meander line Type III
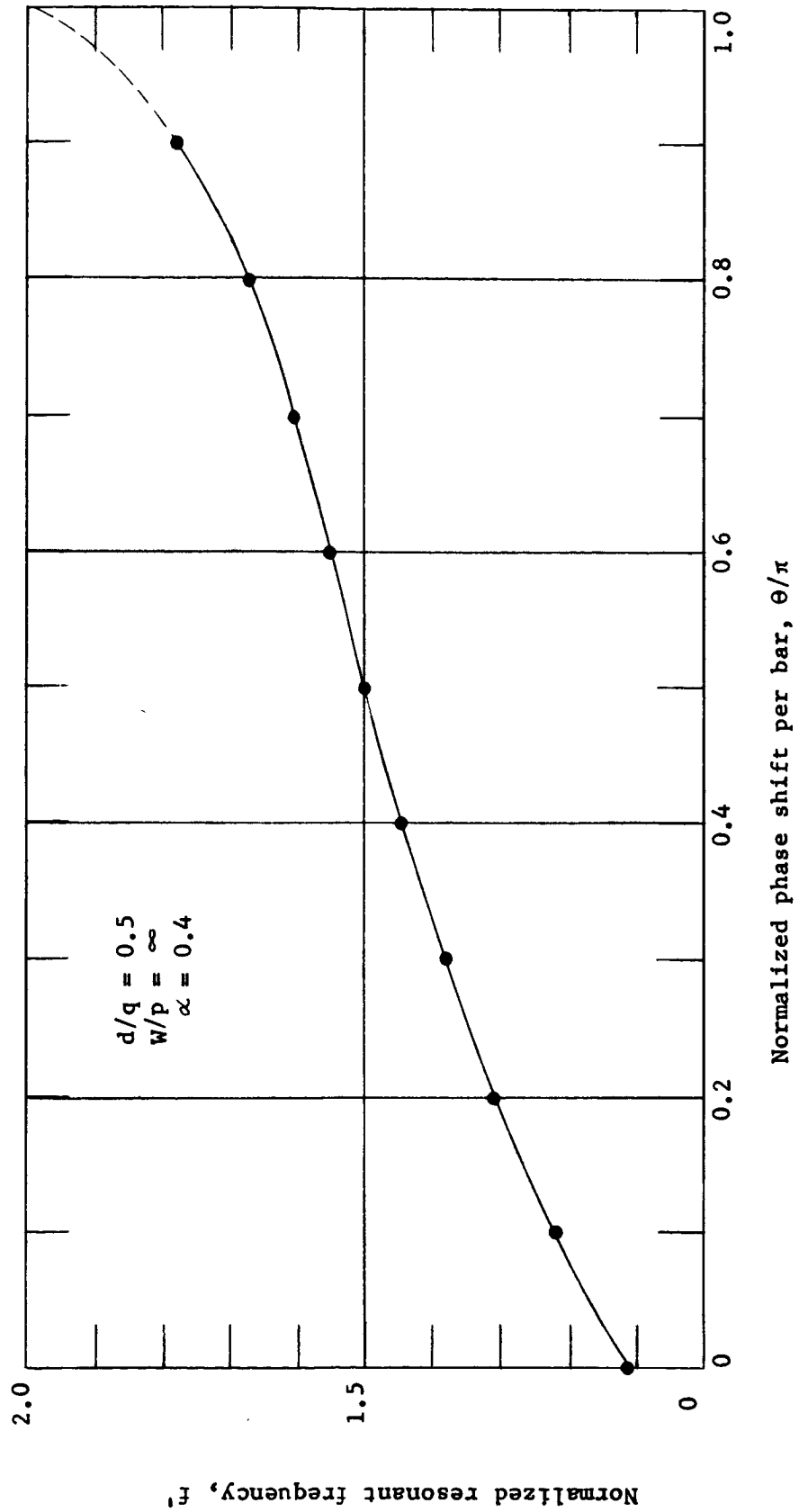
Figure 35. Dispersion characteristic of meander line Type IV
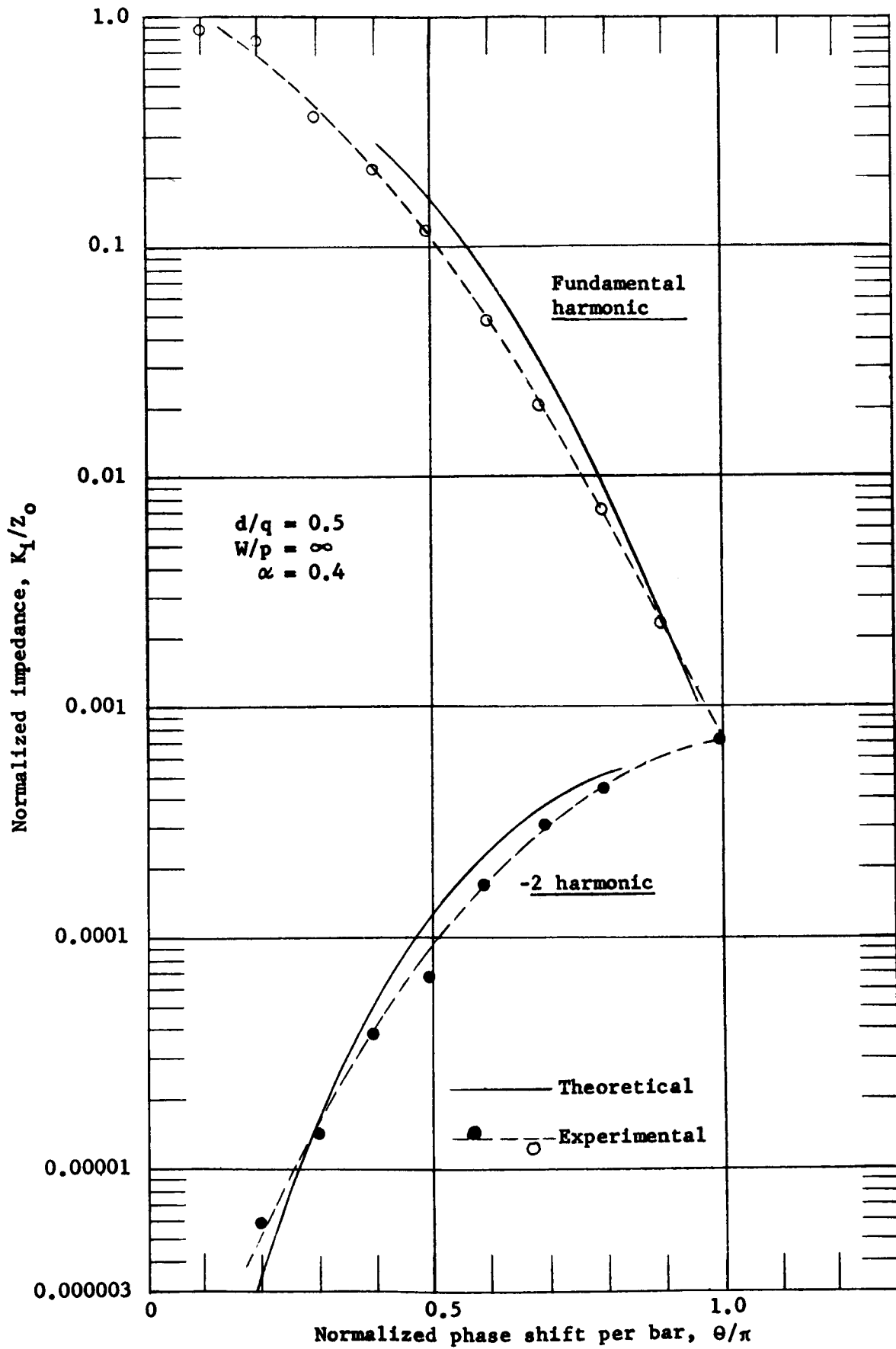
Figure 36. Interaction impedance on the axis of meander line Type IV
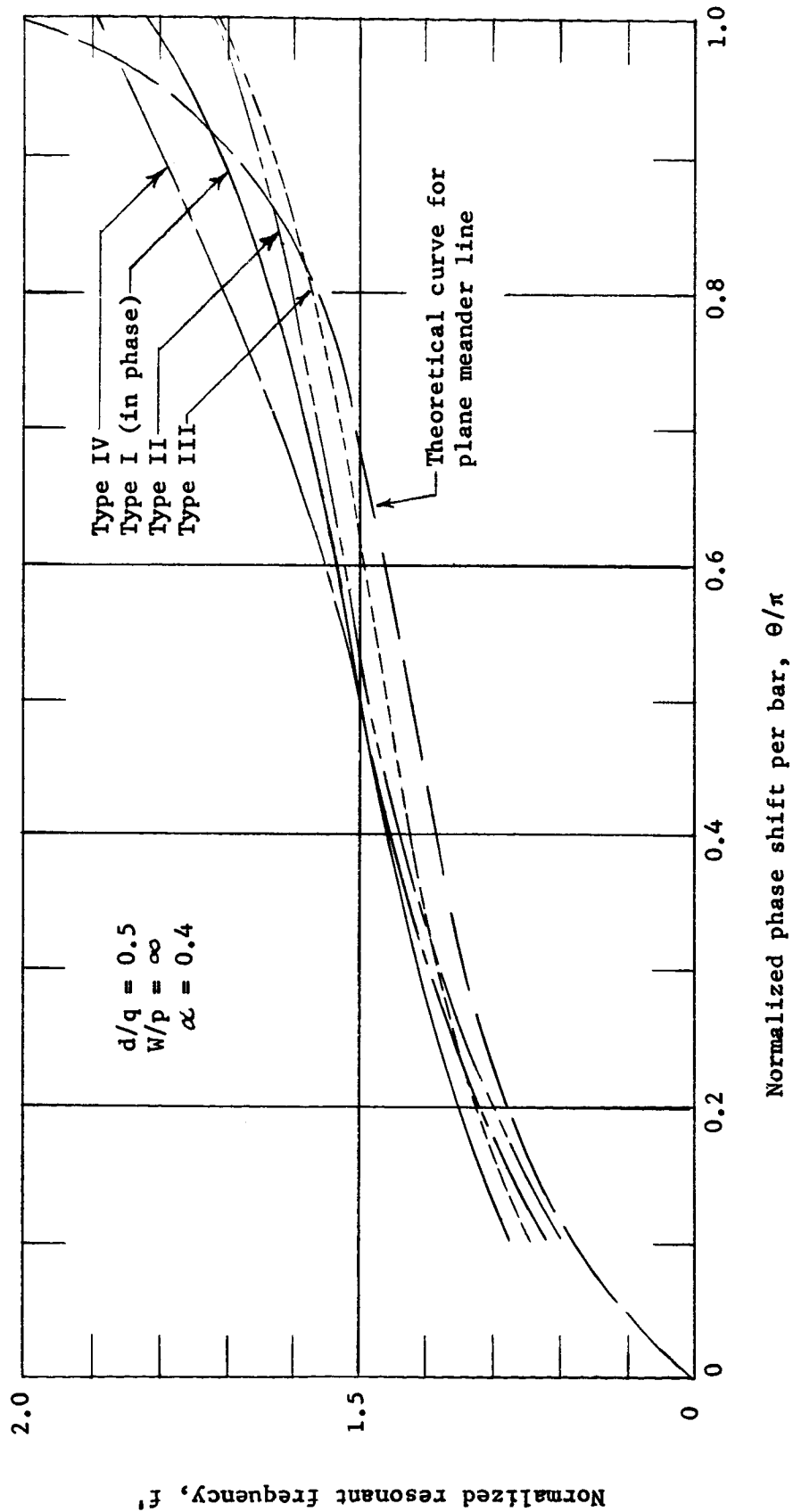
Figure 37. Dispersion characteristics for the several types of meander lines
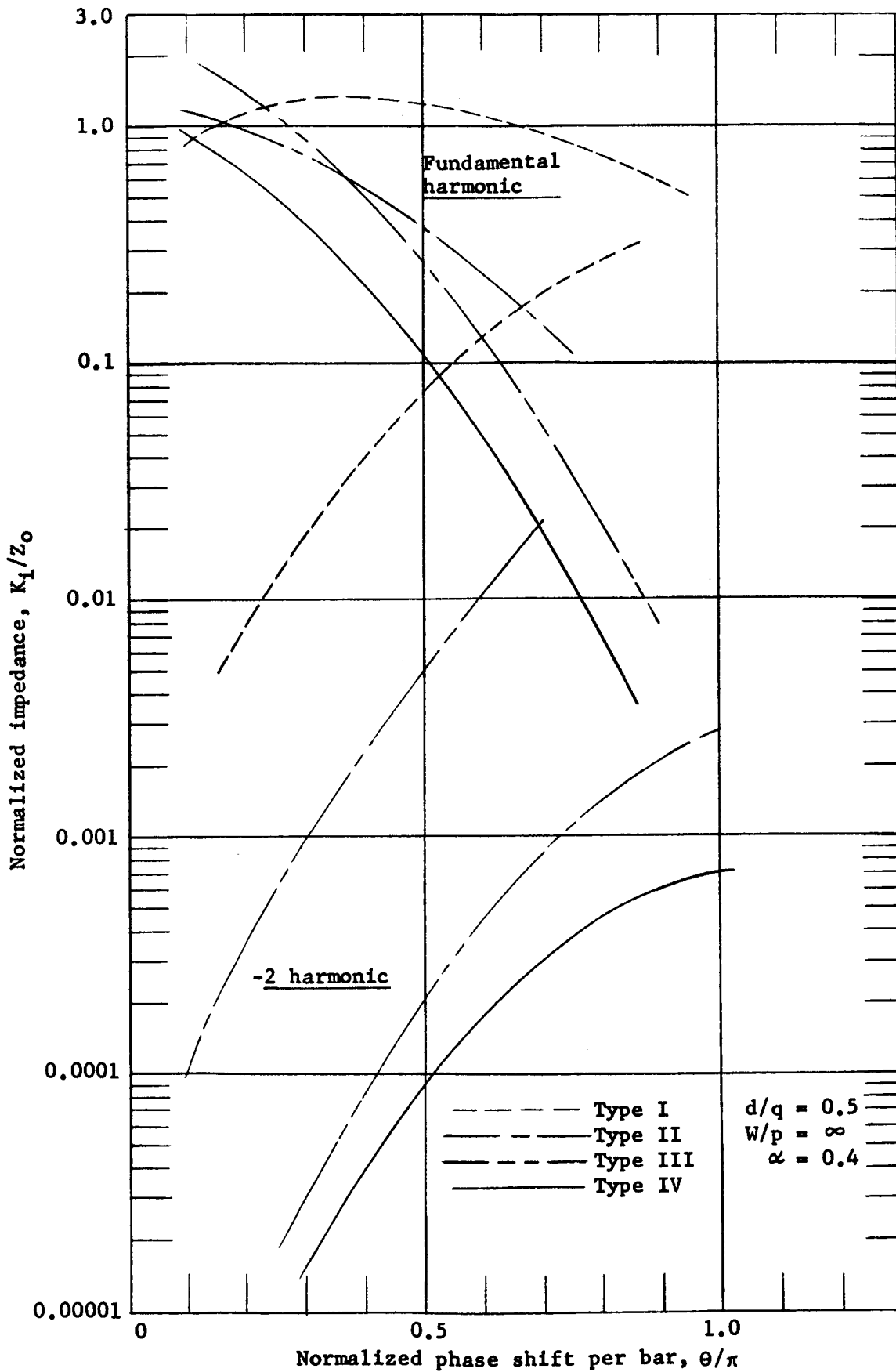
Figure 38. Interaction impedances for the several types of meander lines

and the -2 harmonic impedances at the axis of the structure for circuits Type II and Type III respectively. In each case the theoretical curves are given; these were obtained by multiplying the theoretical values for the plane meander line by the appropriate value of the Bessel function to give the impedance on the axis. Impedance curves for meander line Type IV are shown in Figure 36. Impedances are given at the center of the circle of which the half ring forms a part, and for all curves it has been assumed that the fields at the bars are $2I_0(\gamma a)$ times their value at the center.

Figure 38 shows the impedance curves for all the circuits. When comparing these results it must be realized that the plotted impedances depend upon (γa). For example, although the -2 impedance on the axis of the Type III circuit is lower than that of the Type II, the Type III circuit has a larger beam tunnel and therefore a greater interaction area.

Finally, a few brief remarks concerning the accuracy of the measurement schemes are appropriate. Errors are due mainly to inaccuracies in determining the frequency shift (Δf_r), and the slope of the dispersion curve. The first error is large where the frequency shift is very small, and the second error is large when the slope of the dispersion curve is very low. In the most unfavorable cases, these errors may be as much as ± 25% whereas in other cases errors as low as 5% can be expected. The error in measuring f_r should only be about 1%.

3.3 Anti-symmetric Mode Suppression

The intention, during the early stages of the contract period,

had been to use a Type I circuit in conjunction with a hollow beam
for the millimeter converters. The circuit shown in Figures 39 and
40 was designed for dispersion and impedance measurements in S-band.
These measurements were made by the resonance technique discussed in
the last section. The first experiments performed indicated that two
modes were present in the device. This led to a study of methods of
suppression of the undesirable anti-phase mode. This study was per-
formed concurrently with the L-band program described in Section 3.2.

The presence of two modes was detected during the measurements
when pairs of resonances were observed which were separated in frequency
by only a few percent. The two modes were labeled the symmetric or ++
mode and the anti-symmetric or +- mode. The +- mode is characterized
by out of phase voltages on diametrically opposed circuit elements,
transverse electric fields which will store useless energy, and cir-
cumferential circuit currents.

Mode suppression can be accomplished either resistively or
reactively and by either suppressing the transverse electric field
or the circumferential wall currents. Care must be taken, of course,
so that the mode suppressor does not interfere with the desired ++ mode.
Suppressing the transverse electric field is not an attractive method
because the suppressor probably would interfere with the electron beam.
Although not suppression per se, excitation by symmetrically arranged
couplings reduces the tendency to set up an anti-symmetric mode.
Suppression by resistive methods is less attractive than by reactive
methods, especially in a millimeter device where it is much more dif-
ficult to prevent the lossy material from affecting the desired mode.
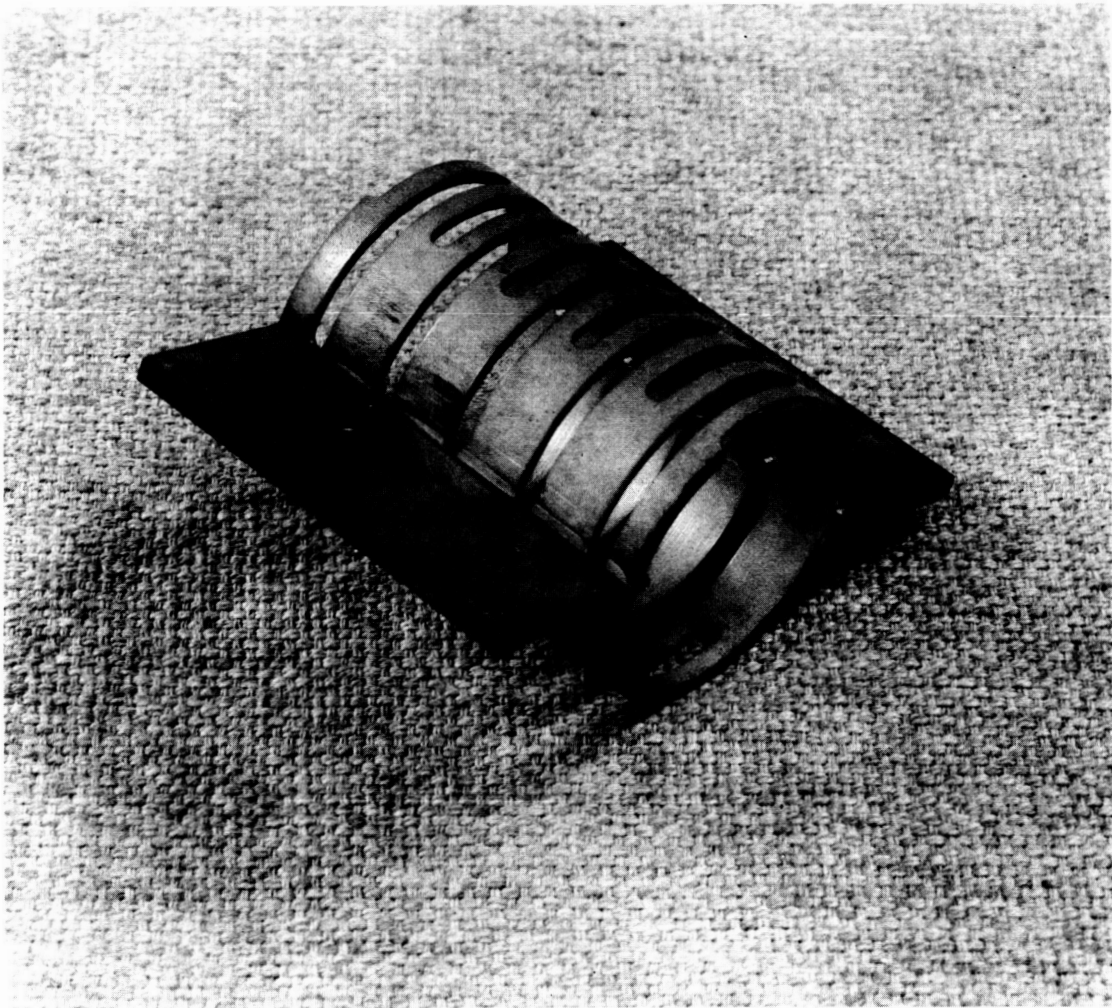
Figure 39. Type I circuit for S-band measurements
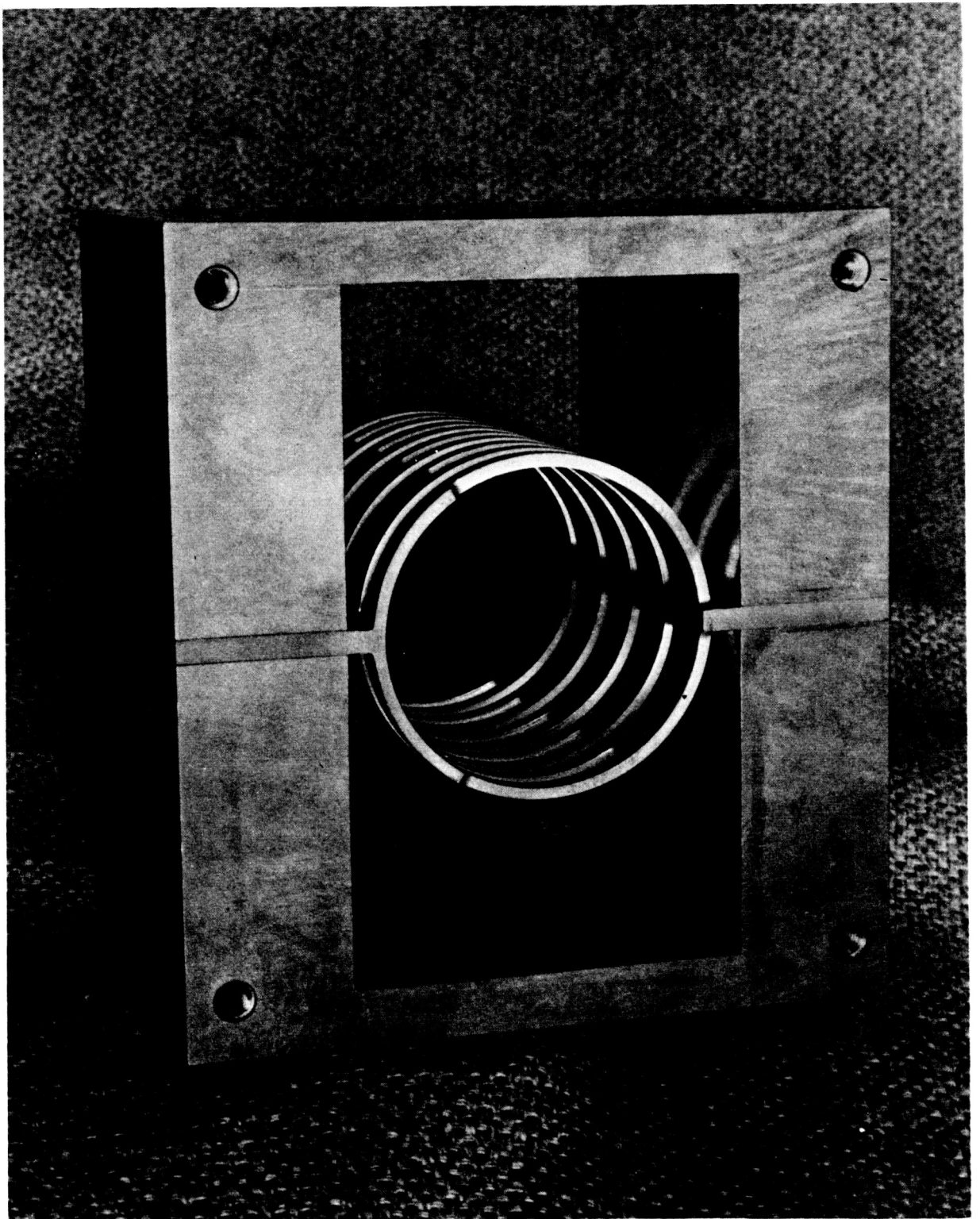
Figure 40. Type I, S-band circuit in resonant structure (end-walls removed)

Both resistive and reactive mode suppressors were investigated. Resistive suppression means providing high loss for the undesired mode but, unfortunately, does not prevent the electron beam from delivering energy to this mode. The effect of reactive suppression is to change the frequency of the undesired mode. This is done by changing the path length of the wall currents. If the frequency is changed far enough, the +- mode can be kept completely out of the range of operation. If reactive suppression is combined with symmetrical coupling, the interaction impedance presented to the beam by the +- mode should be nearly a pure reactance. The beam, therefore, cannot deliver energy to this mode.

Figure 41 shows the Type I circuit with lossy material between the two half circuits. This arrangement increased the transmission loss for the +- mode without significantly changing the transmission loss for the ++ mode. Figure 42 shows the Type I circuit which has been arranged to both increase the current path length and interrupt the transverse electric field. Not only was frequency separation noted but also increased transmission loss for the +- mode, the latter probably due to the reactive suppression of the transverse electric field. Beam interference naturally would be a problem in this device.

Finally, mode interference is not a problem in the Type II (and to a lesser extent, the Type III) and Type IV circuits. The current path for the ++ mode is determined by the slot length, which is constant in the four types, whereas the current path for the +- mode is determined by the beam tunnel circumference. These two lengths are
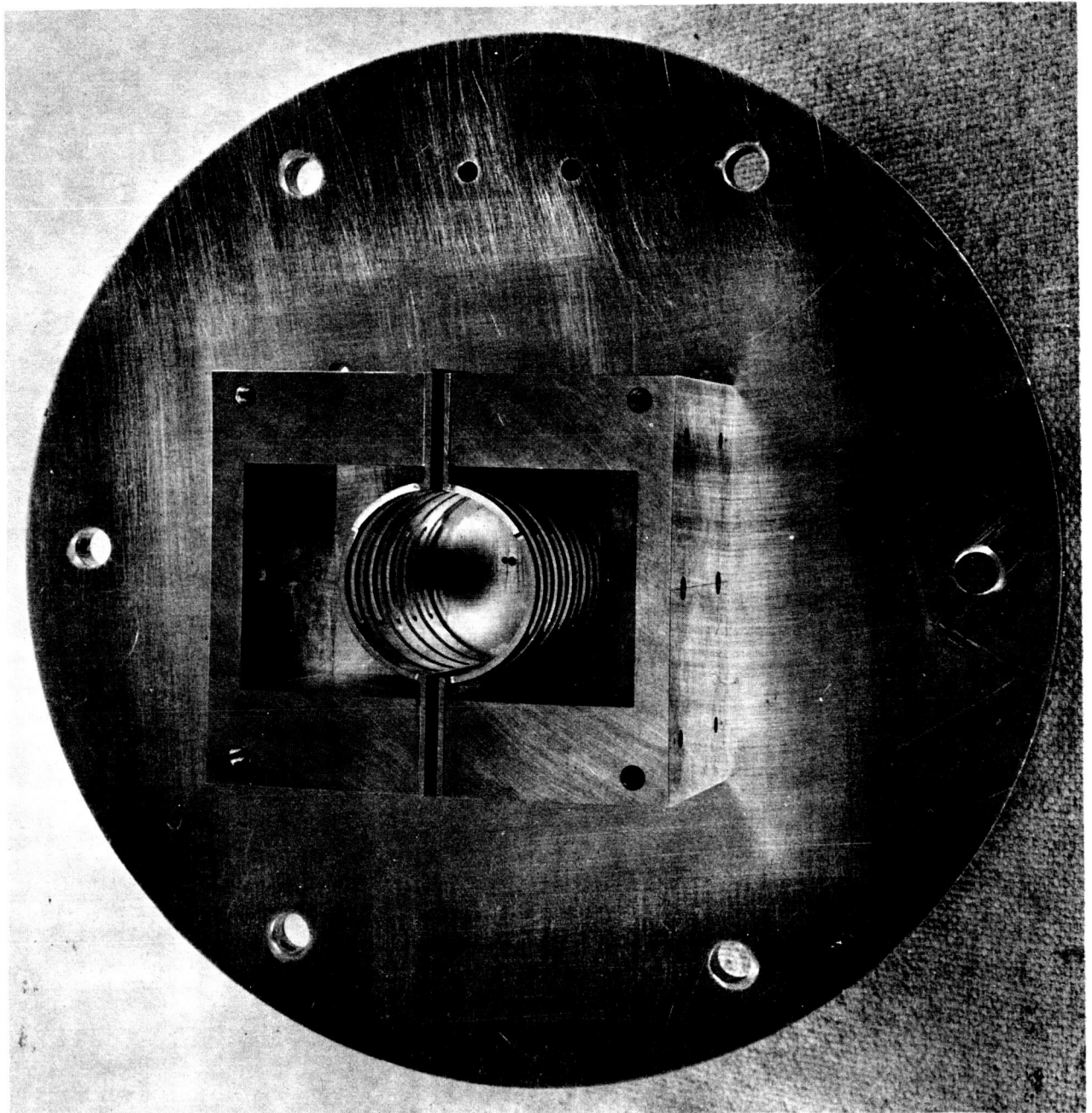
Figure 41. Type I, S-band circuit with resistive mode suppressor
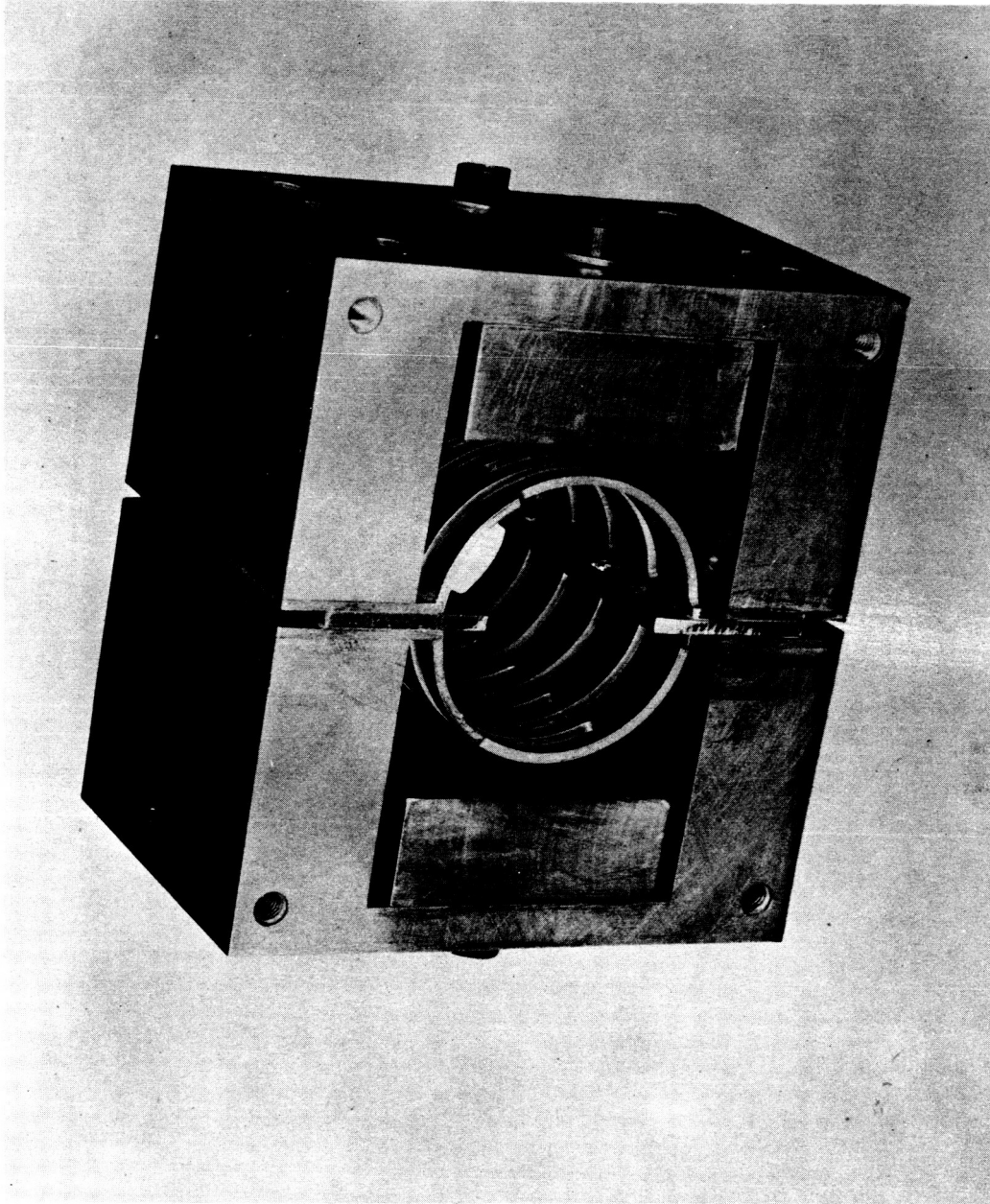
Figure 42. Type I, S-band circuit with reactive mode suppressor

vastly different for the Type II circuit and mode interference problems did not occur with this circuit. The frequency of the +- mode obviously was well outside the range of operation. The Type IV circuit, since it is only a half circuit, will not support two modes - they cannot even be defined.

4. TASK C

4.1 Introduction

This task was concerned with the design and construction of a prototype single circuit converter tube for the 50 - 75 Gc/s region of the spectrum. As stated in the introduction to this report (Section 1), the best course to follow would have been to await the results of the circuit measurements (Task B, Section 3) before beginning the design of the Task C tube. However, the time available for completion of this contract did not allow that luxury. It certainly was not feasible to design tubes based on all four types of circuits discussed in Section 3, so certain judgements, based on preliminary evidence, had to be made in order to decide which circuits to try.

If reasonable efficiency is to be attained, it is necessary to use a hollow beam with the Type I circuit. Although a hollow beam is much easier to control than a strip beam, it is more difficult than a solid beam. In addition to this problem with a hollow beam, the problem of anti-symmetric mode suppression, discussed in Section 3.3, suggested that it would be well to avoid using the Type I circuit in a tube.

There is no essential difference between the Type II and the Type III circuits. They were differentiated in Section 2 only for purposes of indicating the effect of tunnel diameter on dispersion and impedance. The starting current requirement combined with maximum available cathode current density will fix the tunnel diameter in a tube. Therefore, it will not be possible, at this point, to distinguish between a Type II and a Type III circuit. Instead, we will call either a full

circuit in contrast to the Type IV circuit which we will call a half circuit. Thus, we are left with only two circuits; the full and the half. With only preliminary results available, we felt it was necessary to build tubes using at least two different circuits.

This is not meant to imply that there is no technical justification for trying these circuits. The full circuit is an obvious one to try. It uses a solid beam and, because the tunnel diameter is less than the bar length, the anti-symmetric mode should be suppressed. Some impedance data were available for this type of circuit so estimates of starting current, for a given circuit length, could be made.

The full circuit may be thought of as two half circuits in parallel. Therefore, based on this simple model, the impedance of the half circuit should be twice that of the full circuit. Since only half the beam is effective though, Pierce's gain parameter, C, should be the same for the two circuits, providing the total beam current is the same in both cases. The electrical design, therefore, should be the same for both circuits. In addition, there is no mode problem in the half circuit and it is much simpler to construct than the full circuit. Consequently, the half circuit appeared to be a good choice for a milli-meter tube.

Tubes were designed using these two circuits. They were pursued concurrently and independently. The full circuit tube design and construction were performed in our English laboratory, Standard Tele-communications Laboratories, Ltd. (STL) in Harlow, Essex, while the half circuit tube design and construction were performed here in the Electron Tube Laboratory (ETL). The design approaches followed were quite different. The STL tube design was intended only for laboratory experimental

purposes. Since the tube was to be operated between the pole pieces of a laboratory electro-magnet, the mechanical design was not amenable for use in a solenoid or permanent magnet. Although it could be used as either a BWO or BWA, no attempt was made to optimize the design of the collector to make the tube an effective SCC. The main purpose to be served by this tube was to evaluate the performance of the slow-wave circuit.

The ETL tube, on the other hand, was designed to be a versatile, prototype SCC. It was designed for use in a solenoid so that it could later be converted to permanent magnet operation. The collector was designed for converter operation. The mechanical design was such that many parts could also be used for the Task D (DCC) tubes.

In the following sections we will discuss the electrical design which was applicable to both tubes, the mechanical design of the ETL tube, and the r-f measurements made on the STL tube.

4.2 Electrical Design

4.2.1 Gun Considerations

When we come to choose the beam parameters of a millimeter BWC the problem is dominated by two conflicting requirements. On the one hand, sufficient current must be passed down the circuit to start oscillations; on the other hand, beam noise must be reduced to a minimum, which means that interception of the beam by the circuit must be very low and, if the best noise performance is to be obtained, the beam should be launched by a low noise gun.

During the work on this project a great deal of evidence, both experimental and theoretical has accumulated to show that an SCC would

have a poor noise performance and that in all probability a DCC would be required. It was therefore decided to design the SCC gun in such a way that it could also be used for the DCC, and furthermore to choose the electrical parameters of the gun so that it could later be replaced by a low noise gun without any modification to the circuit. This would mean that eventually full advantage could be taken of the double circuit in getting the best noise performance possible.

Not all of the factors which determine the performance of very low noise guns are yet understood. It is, however, quite certain that the use of a convergent gun will add to the noise in the beam - very low noise guns are invariably slightly divergent in the region immediately in front of the cathode. Many factors such as high cathode loading, beam interception and circuit loss make the attainment of the best noise factors prohibitively difficult at millimeter wavelengths but even taking these into account the disadvantages of a convergent gun were considered to be too great and it was decided to design the tube around a rectilinear beam.

The decision to use a rectilinear beam raises the question of cathode loading. It immediately became clear that it would not be possible to obtain the required current densities from an oxide cathode and that some form of dispenser cathode would be required. Such cathodes have a higher operating temperature than oxide cathodes and this fact, in itself, will degrade the noise performance of the tube. However, published data on the impregnated cathode[12] suggest that a current density of 4 Amps/cm^2 can be obtained at a temperature of 1030°C. At this temperature the theoretical noise figure would be increased by only 1 db and hence this should not be a limiting factor in the noise performance of a millimeter wavelength tube.

4.2.2 Beam-Circuit Considerations

Having decided to use a rectilinear gun with a current density of 4 Amps/cm^2 it only remains to determine the smallest diameter beam with which the tube will oscillate. To use an unnecessarily large beam will not only mean an unnecessarily high beam power but will probably make the attainment of a low noise gun more difficult.

The starting current was therefore calculated at various points in the frequency range for a tube employing a full circuit. The frequency limits of 50 to 75 Gc/s were to correspond to beam voltage limits of 600 to 4500 volts respectively. The calculations were based on the plots of CN at start of oscillation against Q/N given by Johnson[13], where Q is the Pierce space charge parameter and N the number of beam wavelengths. The dispersion curve for the circuit was taken from the measured voltage frequency plot of a BWO employing a single plane circuit,$^+$ while the impedances were taken to be the measured impedances of the full circuit form, with a tunnel diameter of 0.010 in. (Type II). Calculations were made for circuits of various tunnel diameters, assuming the circuit length to be 90 bars and the corresponding circuit loss to be 15 db, an average value measured for plane circuits. One calculation also was done for a circuit 120 bars long. In all cases the beam diameter was assumed to be 0.003 in. less than the tunnel diameter. The results are shown in Table 3.

$^+$This tube was mentioned on page 6 of the final report for Contract NASw-430. Since the completion of that contract, extensive measurements have been made on this tube and they can be used to advantage here.

Tunnel diameter (in.)	Circuit length (no. bars)	Beam current (mAmp.)	Ratio of beam current to calculated starting current				
			50 Gc/s	51.7 Gc/s	55 Gc/s	62.5 Gc/s	75 Gc/s
0.020	90	5.8	?	0.11	0.95	3.1	3.2
0.025	90	9.8	0.09	0.41	1.5	5.	4.2
0.030	90	14.72	0.091	0.405	1.49	4.9	3.1
0.020	120	5.8	0.075	0.34	2.2	6.1	4.4

Table 3. Starting currents for various beam tunnel diameters.

One important factor emerged during these calculations. In TWT design the dominant parameter is the Pierce parameter, C, in which the interaction impedance, K, appears as $K^{1/3}$. However, in a BWO we find that the starting current at best varies as $1/K$ while if Q/N rises above about 0.1 the variation is rather more rapid than this. Hence, with a BWO, it is important to keep K as high as possible over the whole band.

It is clear from Table 3 that the frequency range of the BWC is likely to be limited to 55 - 75 Gc/s. An increase in tunnel diameter from 0.02 to 0.025 in. might only increase the bandwidth marginally at the cost of almost doubling the beam power. Increasing the circuit length from 90 to 120 bars might give some increase of bandwidth but at a cost in magnet weight. These figures were based on the only measurements available at the time, which were on a circuit of slightly different proportions. Taking all these factors into account it was decided to use a 90 bar circuit with a tunnel diameter of 0.02 in. with the reservation that the circuit length might have to be increased subsequently to meet the full bandwidth requirement.

4.2.3 Gun Design

Although it would be desirable to use a low noise gun in this tube, the design and test of such a gun is a minor project in itself (see Section 5). Therefore, it was decided to use a simpler gun but to arrange the mechanical design of the tube to be versatile enough to accommodate a low noise gun when it became available.

The gun that was designed was a "half-cycle, full-cycle" gun.[14] It is shown schematically in Figure 43. The voltages shown
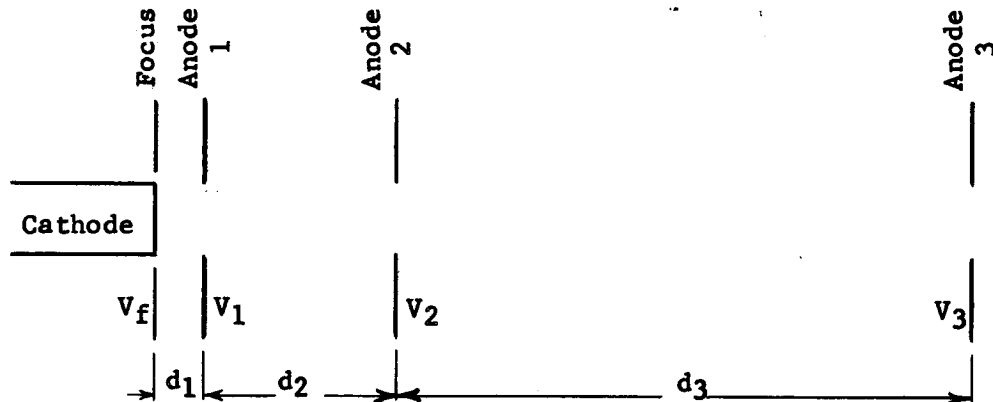
Figure 43.   Schematic representation of the electron gun for the SCC.

are given with respect to the cathode. The voltage on anode 3 should be the circuit voltage. For convenience, the focus will be kept at cathode potential, that is, $V_f = 0$.

One more quantity must be specified for a design based on Reference 14. The most convenient one to specify, for design purposes, is V_1. Designs were made for three values of V_1:   300, 400, and 500 volts.

In summary, the specifications are:

$$J_o = 4 \text{ amp/cm}^2$$

$$V_f = 0$$

$$V_1 = 300, \ 400, \text{ and } 500 \text{ volts}$$

$$600 \lessapprox V_3 \lessapprox 4500 \text{ volts}$$

The design leads to the values given in Table 4.

V_1 (volts)	V_2 (volts)	d_1 (in.)	d_2 (in.)	d_3 (in.)	B (gauss)
300	1640	0.0218	0.104	0.292	1155
400	1640	0.027	0.094	0.252	1340
500	1640	0.032	0.085	0.219	1540

Table 4. Design values for SCC electron gun.

The values for $V_1 = 300$ volts were chosen for the gun. This yielded the lowest magnetic field of the three designs. A lower value of V_1 would give a lower magnetic field, but d_1 would begin to be inconveniently small.

4.2.4 Circuit Design

The physical dimensions of the circuit chosen are (see Figure 44)

Bar length (2b)	0.136 in.
Circuit pitch (2p)	0.022 in.
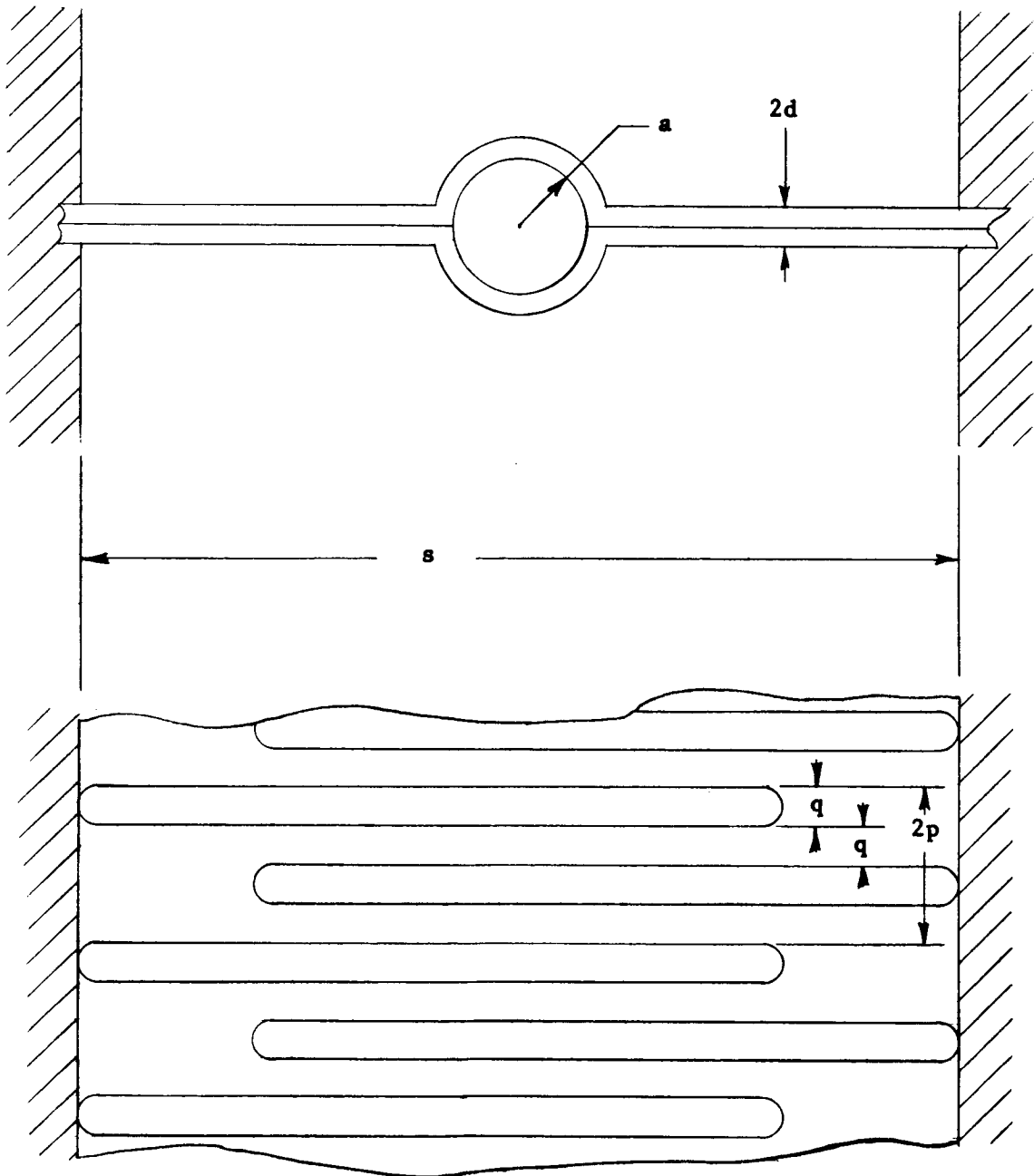
Figure 44. Definition of Type III circuit dimensions

Bar and gap width (q)	0.0055 in.
Circuit thickness (d)	0.0025 in.
Tunnel diameter (2a)	0.020 in.
Sidewall separation (s)	0.1256 in.
Number of bars	90

The sidewall separation is determined from the bar length, tunnel diameter and circuit thickness. If the bar length is assumed to be the mean distance through a half circuit from sidewall to sidewall, then

$$s \approx 2b - \pi(a + d/2) + d + (2a + d)$$

$$= 2b - a(\pi - 2) + d (2 - \pi/2)$$

This circuit was scaled up for measurements in L-band and became the Type III circuit reported on in Section 3. The performance was found to be little different from that of the Type II circuit on which the calculations were based although the interaction impedances were lower.

In the earlier work considerable stress was placed upon the ridge loading of the slow wave structure for the purpose of increasing the bandwidth. This work is still valid but, on the basis of the calculations in this section the margin of I_0 over starting current is nowhere very great. Ridge loading, while it widens the passband of the circuit, also lowers the interaction impedance to some extent. On the other hand it is relatively easy, constructionally, to add ridge loading to an existing tube design. It was therefore felt wiser not to introduce this factor into the earlier tubes.

4.2.5 Magnetic Field Requirements

The maximum Brillouin field is required at the low voltage end, that is, for a beam voltage of 600 volts. With a current density

of 4 Amps/cm^2, the value of Brillouin field is calculated from

$$B = 1470 \ J^{1/2} V^{-1/4} \qquad \text{(gauss)}$$

to be 600 gauss. However, the beam diameter has been taken to be 0.003 in. less than the tunnel diameter which means that the radius of the thermal orbit of an electron on the beam edge must not exceed 0.00075 in. if it is not to strike the circuit. A magnetic field of 5620 gauss is required to attain this condition. It should be emphasized that this value is to be used as a guide; the actual value of magnetic field will be determined experimentally from beam transmission data.

4.3 Mechanical Design of the ETL Tube

The most critical problem in the mechanical design of this tube (as in all millimeter wave tubes) is alignment. There are a number of ways of achieving good alignment between beam and circuit; the one we prefer is the use of precision piece parts. This means that the piece parts are made to high tolerances (± 0.0002 in. for the critical dimensions) so that alignment is achieved automatically during assembly. This method has been applied successfully to another millimeter tube (a reflex klystron) we now have in prototype production.

In addition to the necessary alignment criterion, versatility of the design was considered desirable. This included both the gun region and the circuit region. The gun region was to be designed not only to accommodate the gun described in Section 4.2.3 but also to accommodate a low noise gun when it became available. The circuit region was to be designed to be able to accommodate either one or two

circuits so that the same shell could be used for Task C and Task D tubes. In essence, this meant making each region longer than would have been required for a standard gun, single circuit tube.

The resulting tube design is shown in cross-section in Figure 45. Figure 46 is a photograph of a tube constructed from this design. This tube design can be used with a low noise gun and with two circuits. The collector was designed for a 50Ω coaxial system. The coaxial seal has been designed to take a TNC connector. With this arrangement, an i-f load such as shown in Figure 14 (Section 2.3.2), but with R_1 and the switch removed, can be used.

The details of the slow-wave structure have not been indicated in Figure 45. The dimensions of the structure were given in Section 4.2.4 and a structure made to these dimensions is shown in Figures 47 and 48. Figure 47 shows the circuit brazed into the bottom half circuit block. The two slots running the full length of the block are each half a narrow height waveguide. The two tabs across the slots, one from either end of the circuit, are the coupling antennae. Figure 48 shows the top half circuit block in place but displaced longitudinally so that part of the circuit and one coupling antenna are visible.

The circuits are fabricated from 0.0025 in. molybdenum. Attempts to fabricate circuits from copper sheet were unsuccessful; the copper was too fragile. The first step in fabrication is to form the beam tunnel from the solid sheet. The sheet with the tunnel is then brazed to the bottom half circuit block. Following this, the circuit is cut into the sheet by spark erosion techniques. Finally,
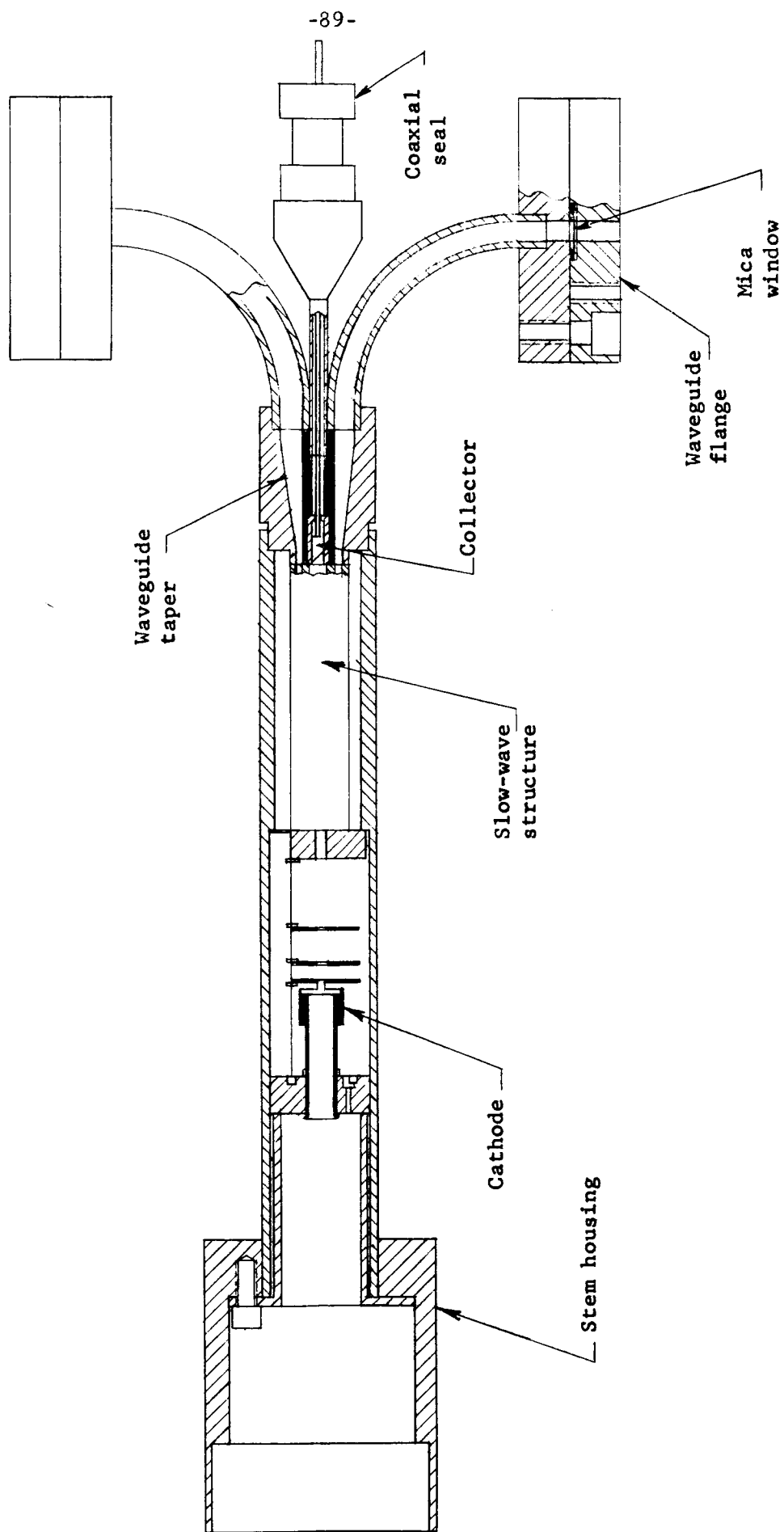
Figure 45. Cross-section of Task C tube

Figure 46. Task C tube
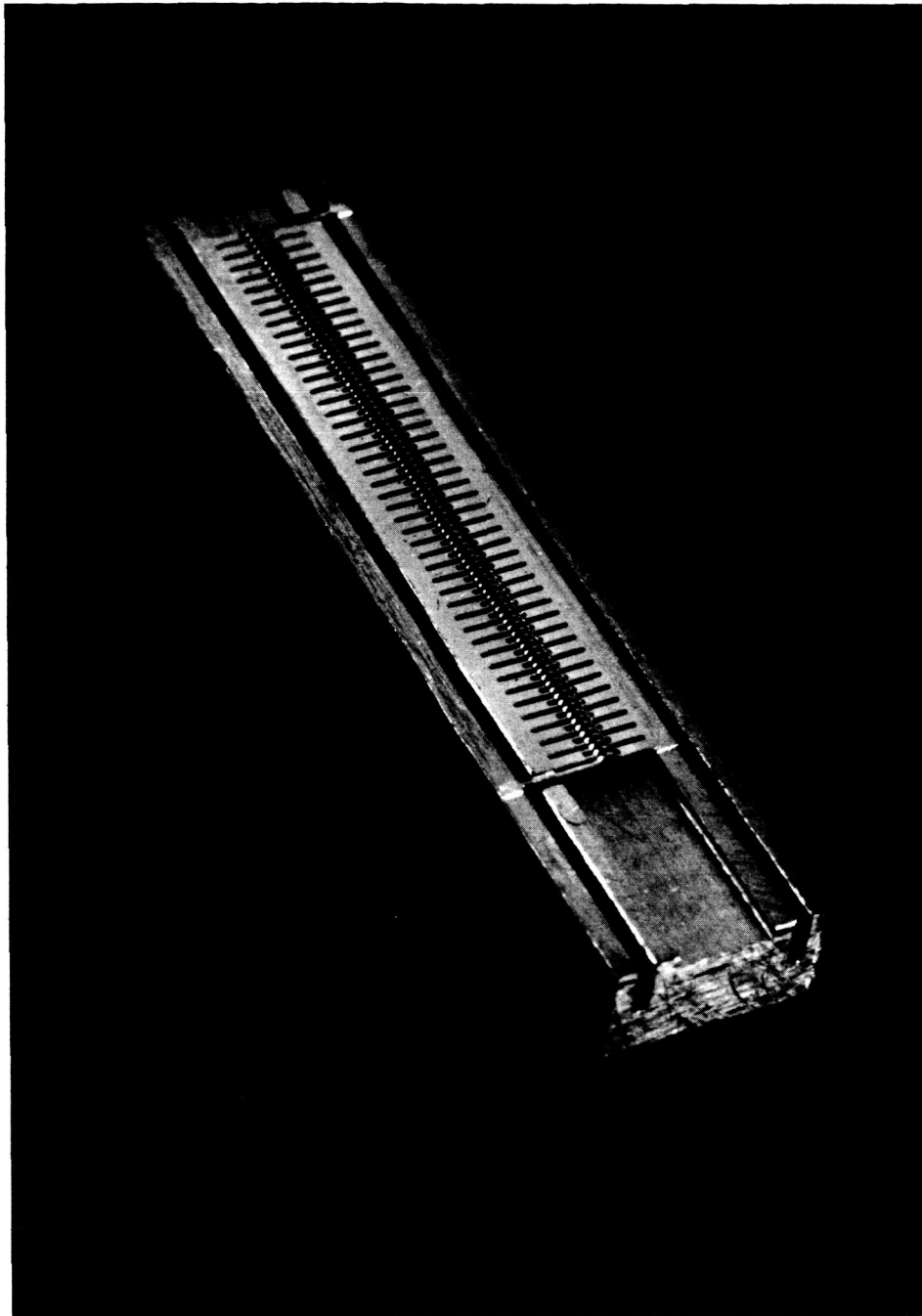
Figure 47. 50-75 Gc/s slow-wave structure with bottom half circuit block
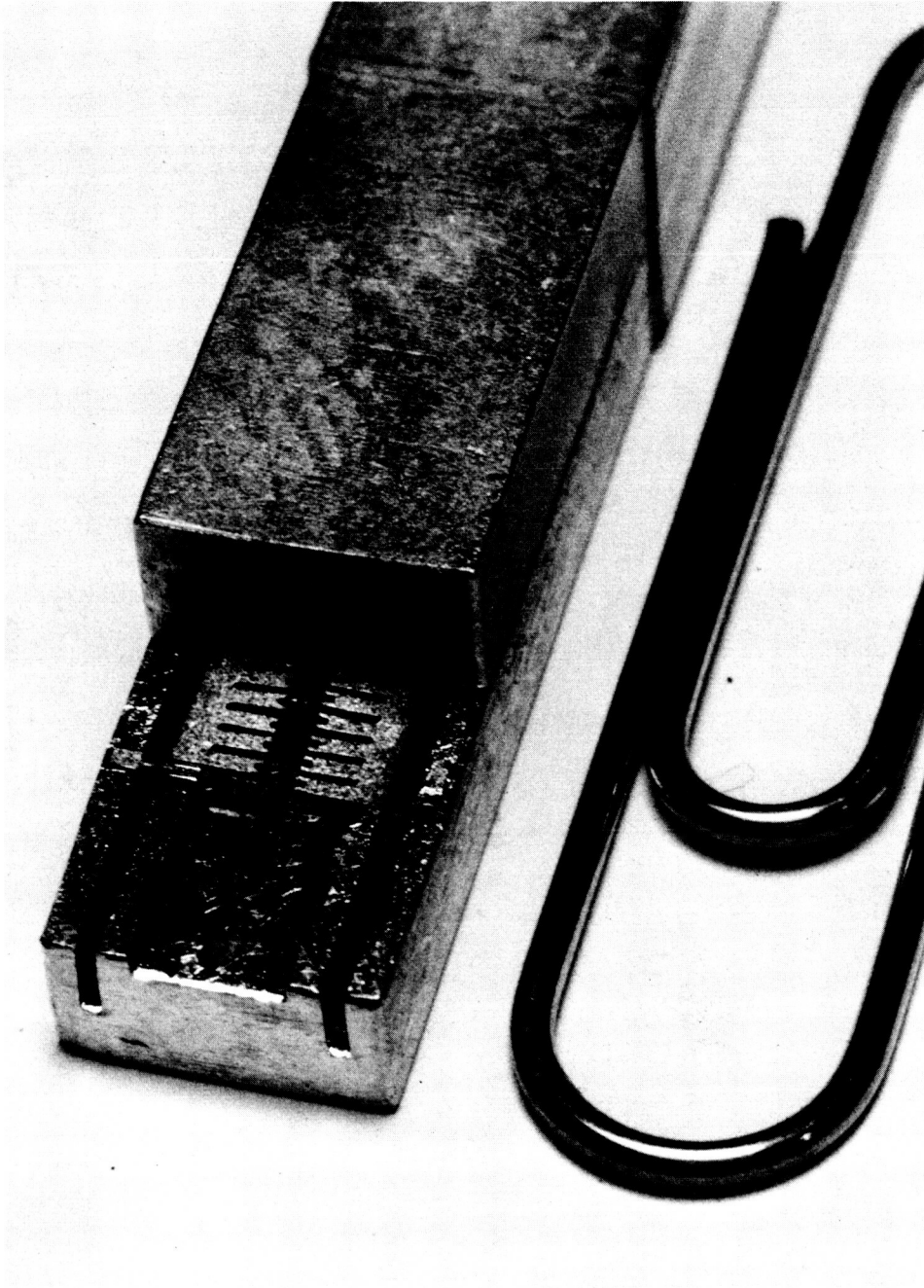
Figure 48. 50-75 Gc/s slow-wave structure with both half circuit blocks

the top half circuit block is brazed in place. Fabrication and assembly
of the remainder of the tube are straightforward.

4.4 Measurements

4.4.1 The ETL Tube

It is obvious now, with the final results available from
Task B, why none of the ETL tubes oscillated. Figure 38 (Section 3.2.3)
clearly shows that the impedance (on the axis) of a Type IV circuit (the
type used in the ETL tube) is only half that of the Type III circuit
whereas we expected it to be twice the impedance of the Type III circuit.
This means that the starting currents for the ETL tubes would be much
higher than those predicted in Table 3 (Section 4.2.2). The reasons for
this difference in impedance are not completely clear although it is
suspected that the fields fall off toward the axis more rapidly in the
Type IV circuit than indicated in Equation (D-4) (Appendix D).

We were able to obtain some evidence of backward-wave ampli-
fication in one of the ETL tubes. It was not possible to measure the
gain; it was probably less than 1/2 db above cold loss. It was possible,
however, to measure three points on the voltage tuning curve which were

V (kV)	f (Gc/s)
0.75	52.5
0.82	54.5
1.2	60.0

These are not unexpected values.

Some rough measurements of beam transmission were possible, too.
For one tube, transmission through the gun was about 50% while transmission

through the slow-wave circuit was about 75%. The low gun transmission may have been due, at least in part, to the lack of focus control on this tube.

For all the measurements, the beam was solenoid focused. The value of the axial magnetic field was about 1600 gauss.

4.4.2 The STL Tube

A more complete set of measurements is available for the STL tube. Figure 49 shows the power output as a function of frequency. A minimum of 10 mW of output power is available from about 67 Gc/s to nearly 75 Gc/s. The tube drops out of oscillation below 65 Gc/s because the required starting current has risen above the beam current (see Figure 54). Figure 50 is the experimental tuning curve.

The tube was also operated as a BWA. Figure 51 shows the electronic gain as a function of beam current for three different frequencies. Gain in the presence of oscillation also was measured and this is shown in Figure 52. The similarity between this curve and the curve for the S-band tube shown in Figure 12 (Section 2.3.2) is quite striking.

Dispersion data were taken on this tube and plotted on the dispersion curve for the L-band model of this circuit, that is, on Figure 33 (Section 3.2.3). The result is shown in Figure 53.

Starting currents as functions of circuit voltage are shown in Figure 54. Insertion loss as a function of circuit voltage is shown in Figure 55. A pronounced similarity exists between the curves of the two figures. The input VSWR as a function of frequency is shown in Figure 56 and the circuit loss as a function of frequency is shown in Figure 57.
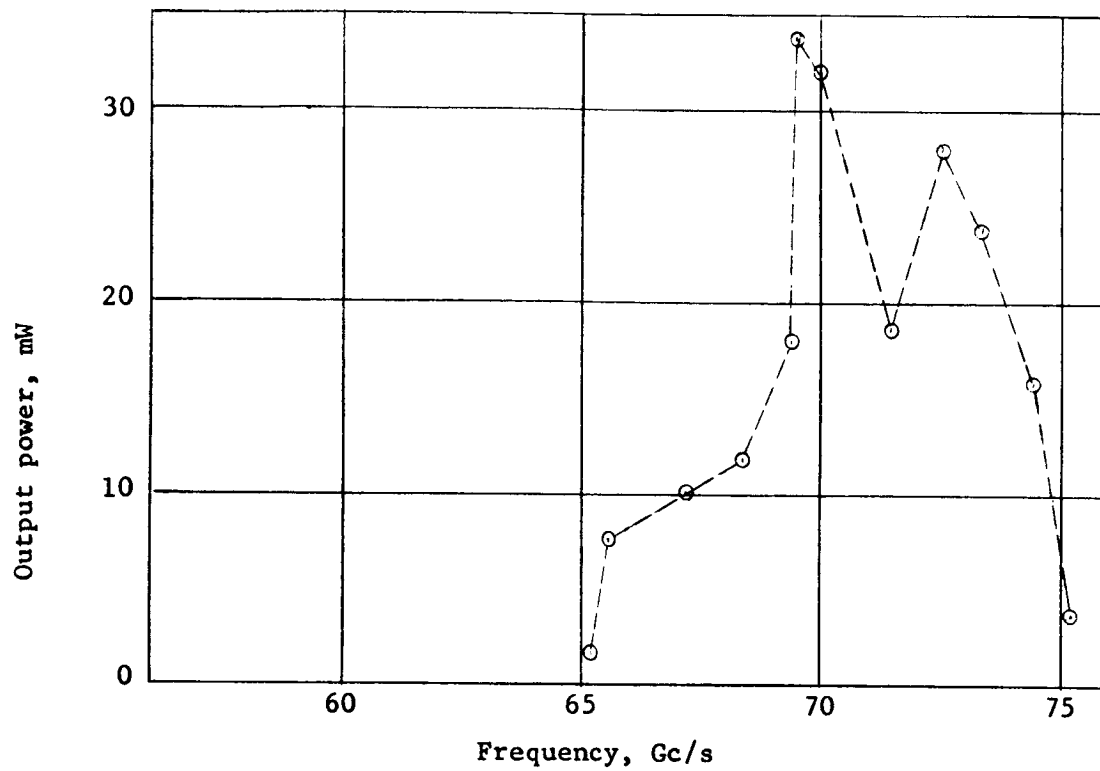
Figure 49. Output power as a function of frequency for the STL tube
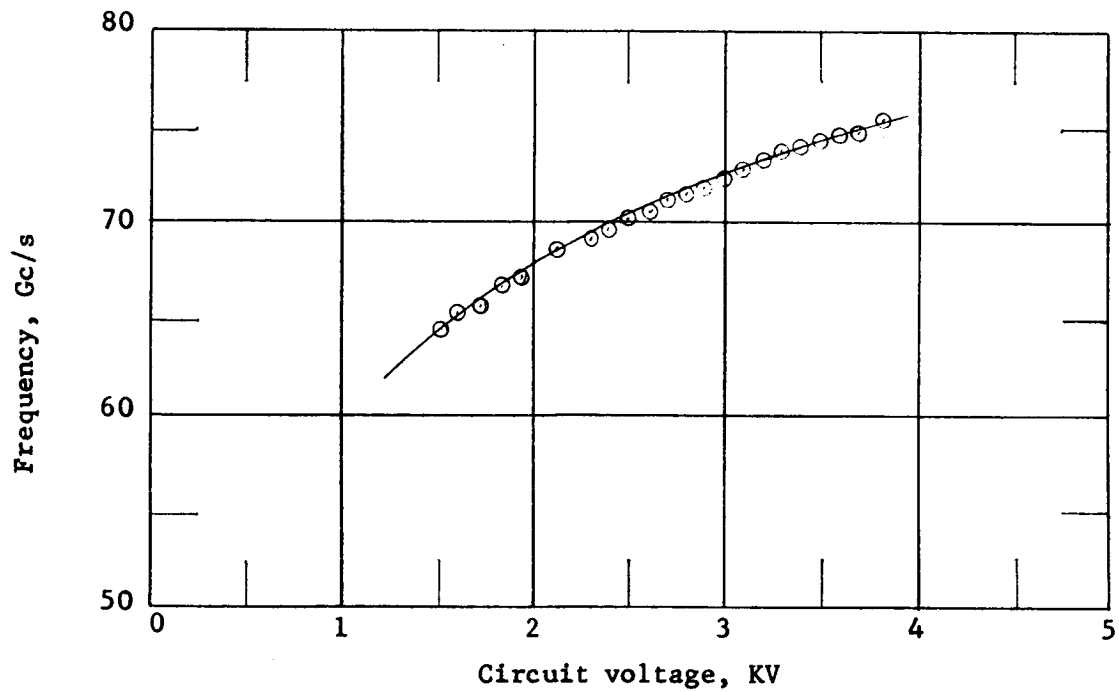
Figure 50. Experimental tuning curve for the STL tube
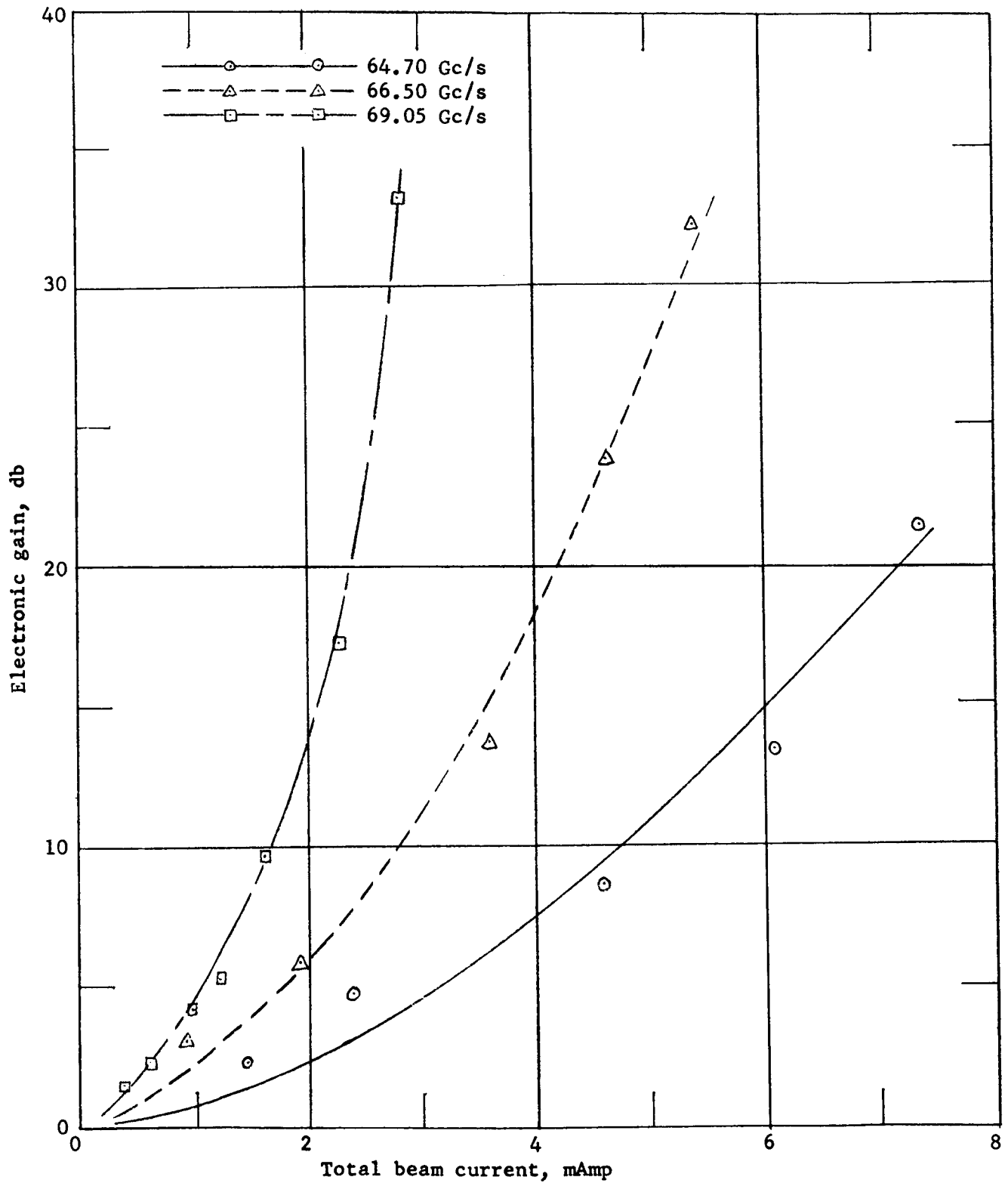
Figure 51. Electronic gain as a function of beam current for the STL tube
operating as a BWA
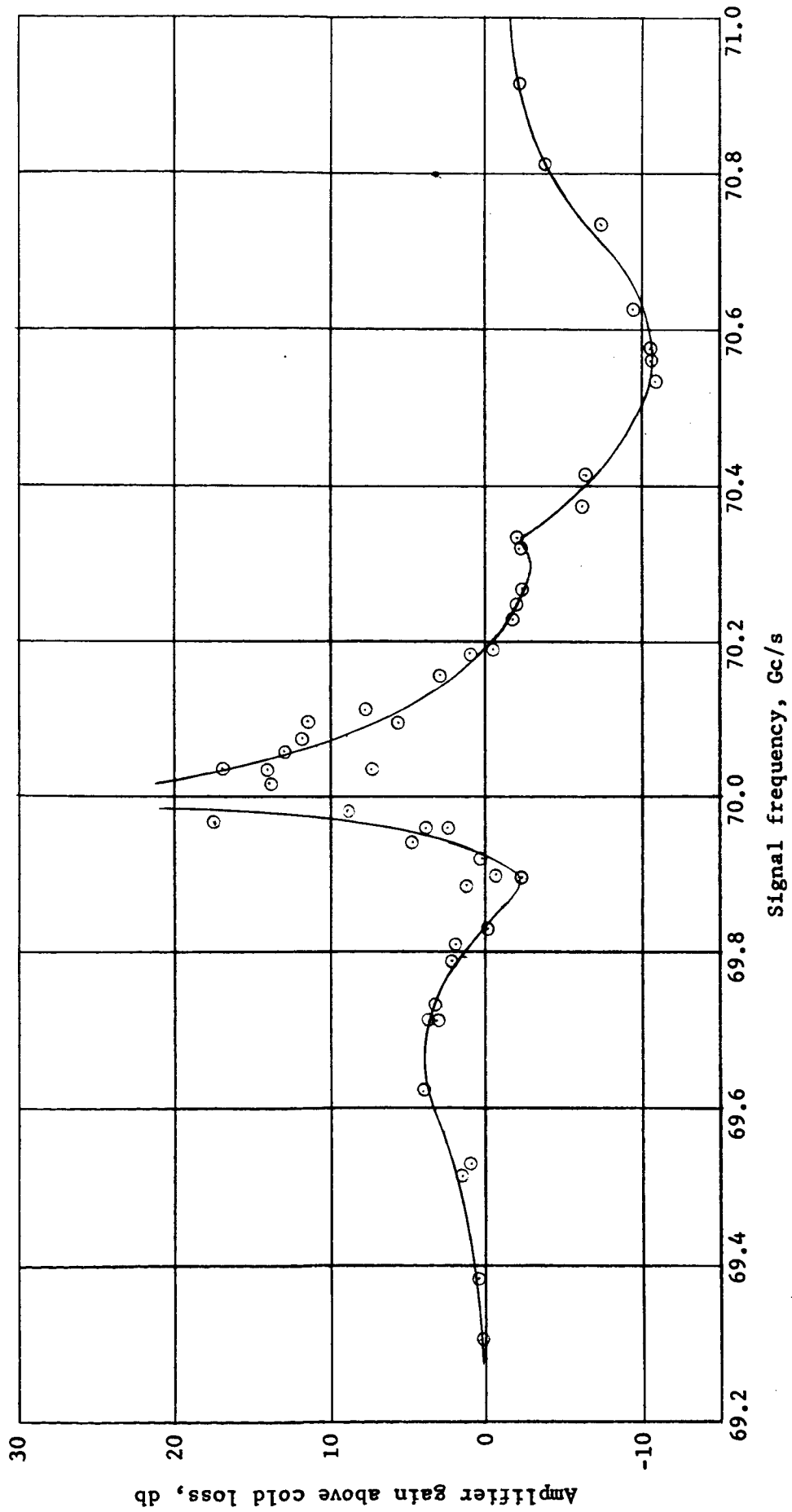
Figure 52. Gain in the presence of oscillation as a function of signal frequency for the STL tube
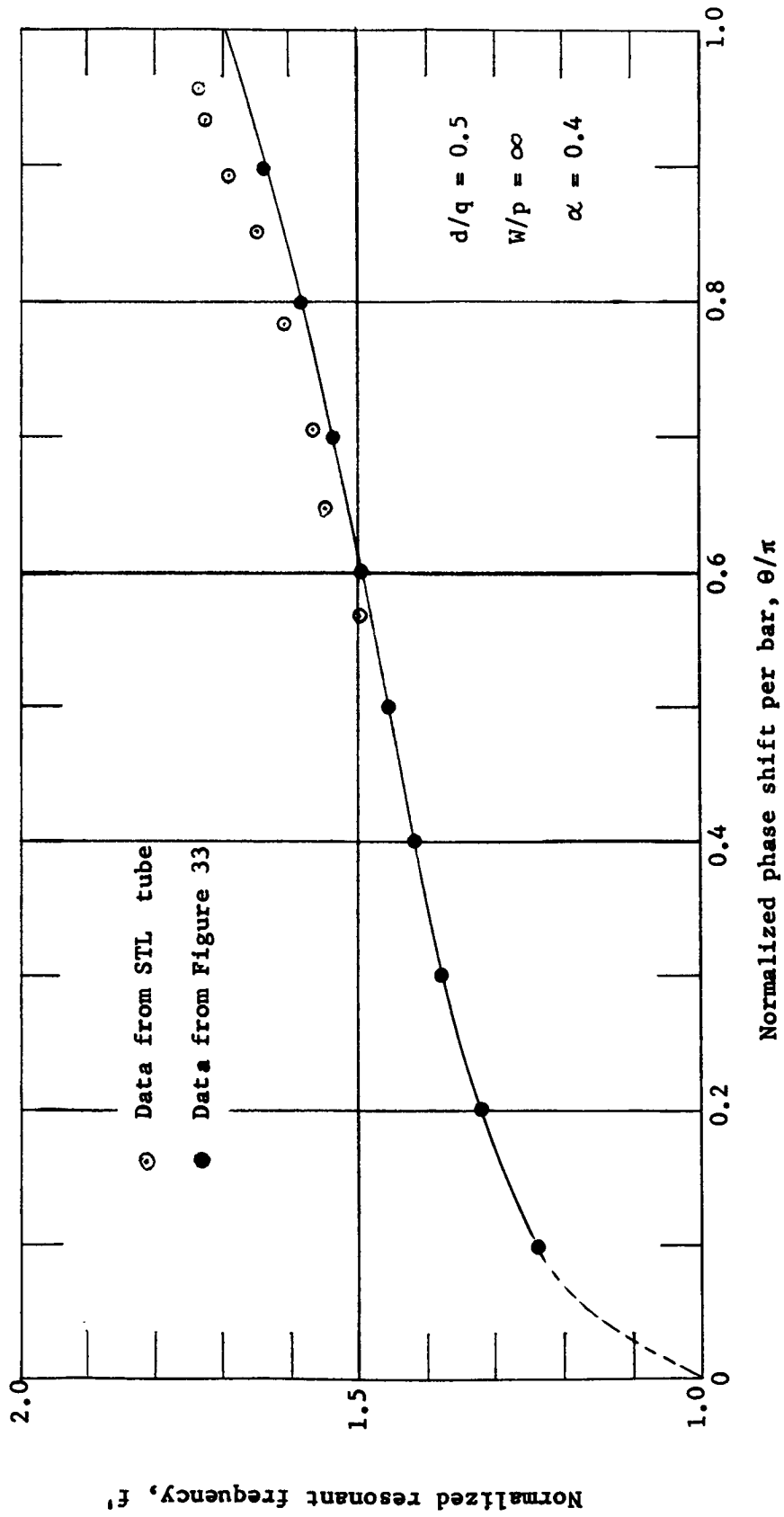
Figure 53. Dispersion data for the STL tube plotted on Figure 33
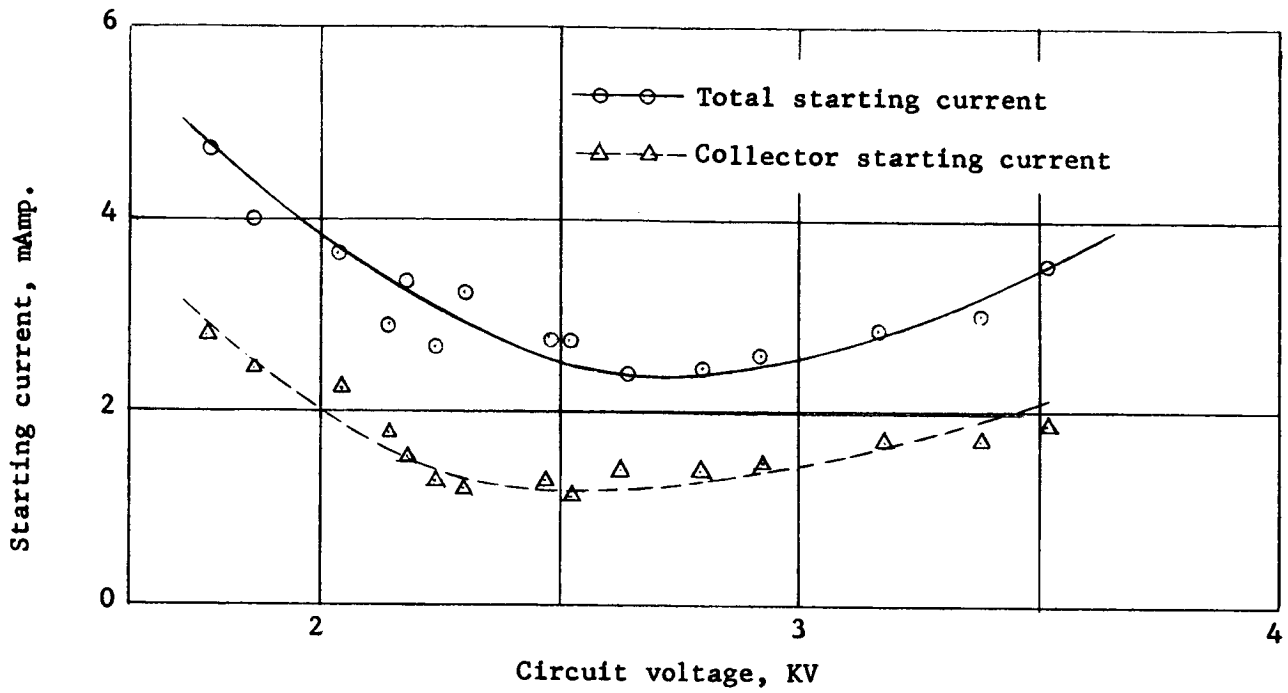
Figure 54. Total and collector starting currents as functions of circuit voltage for the STL tube
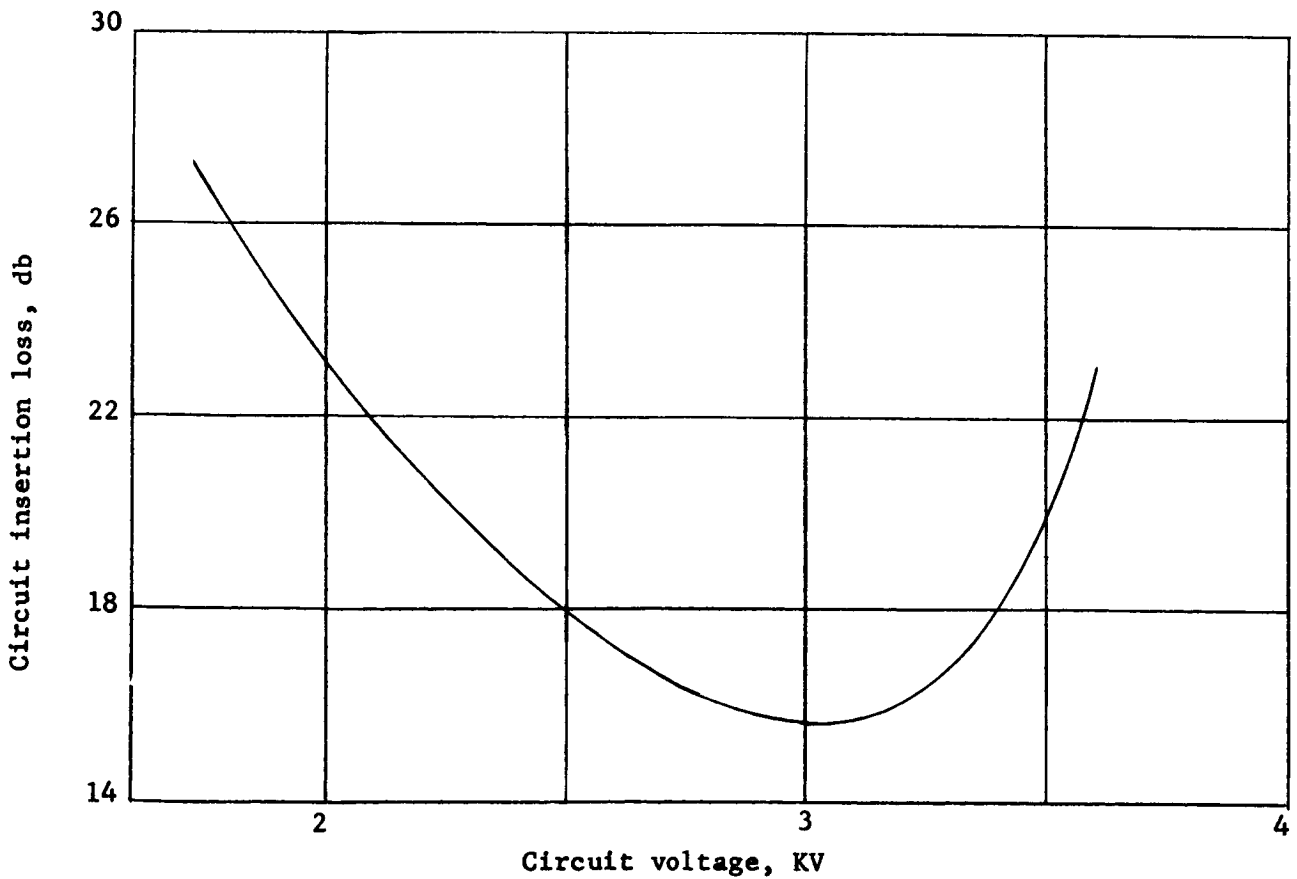
Figure 55. Insertion loss as a function of circuit voltage for the STL tube
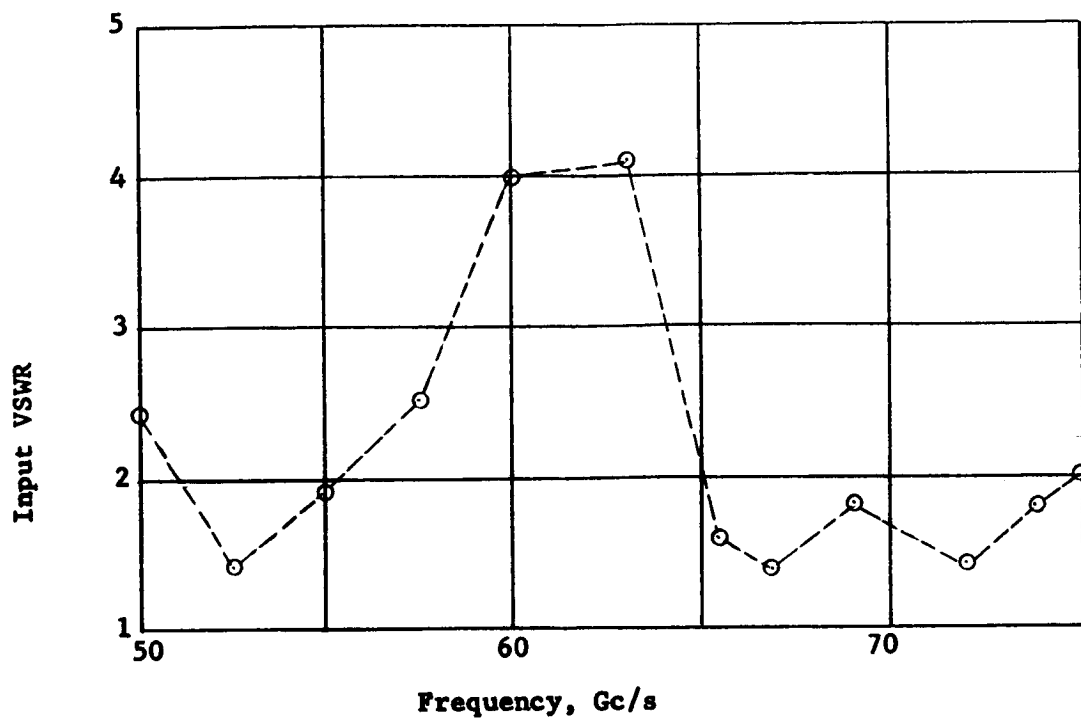
Figure 56. Input VSWR as a function of frequency for the STL tube
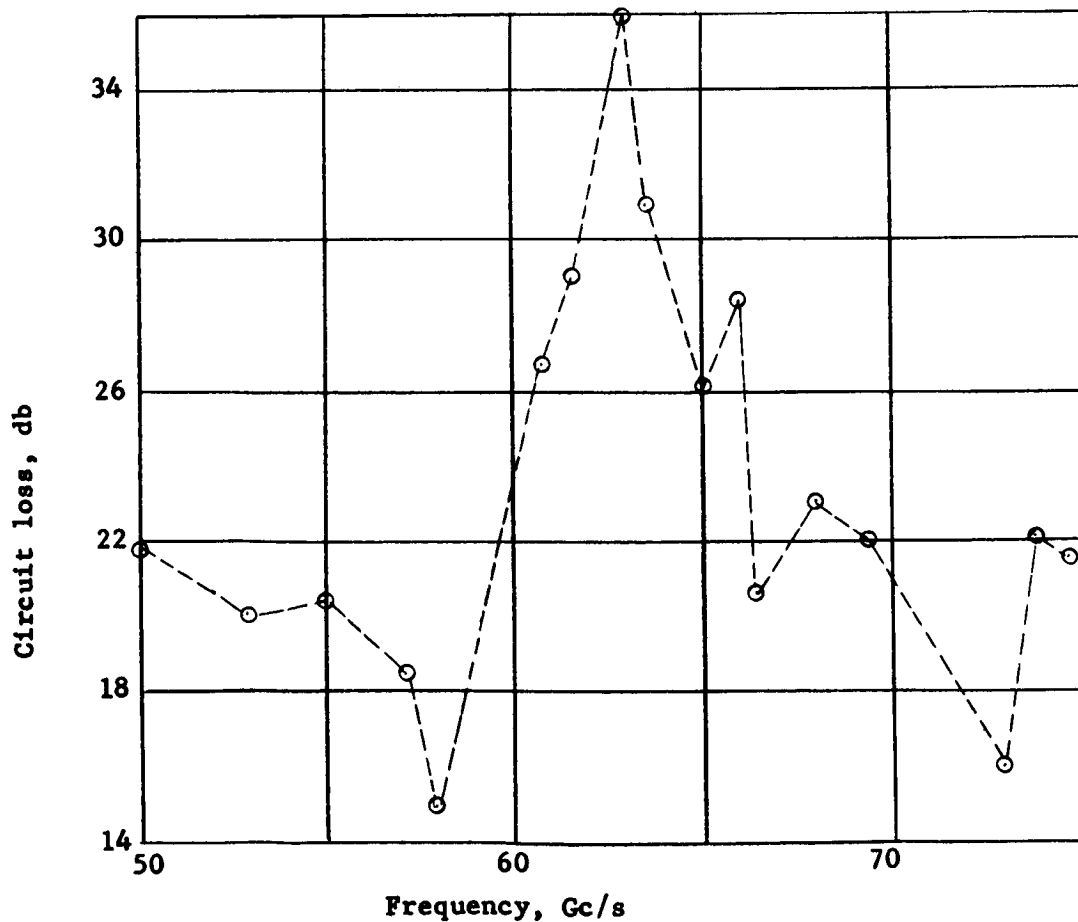
Figure 57. Circuit loss as a function of frequency for the STL tube

Finally, one measurement of conversion gain was made. It should be remembered that the i-f circuit was quite crude for this tube. A conversion gain of -90 db was obtained at f_d = 260 Mc/s (f_s = 70.26 Gc/s). By referring to Figure 52, it can be seen that this is not the most advantageous frequency at which to make a conversion gain measurement. However, no further measurements were made on this tube.

5. TASK D

5.1 Introduction

This task was concerned with the design and construction of a prototype double circuit converter tube for the 50 - 75 Gc/s region of the spectrum. As stated in the contract, this task was to be accomplished after the completion of Task C. Because Task C was not completed, Task D only reached preliminary design stages. Consideration had been given to the required changes to the ETL SCC design (Section 4.3) so that it could be made into a DCC and the necessary piece parts had been designed and fabricated. The design changes will be discussed in this section.

Theoretical and experimental evidence has conclusively demonstrated that the SCC will not be effective as a low level receiver. In particular, the noise performance of the SCC is not good, even with a low noise gun. Therefore, the work that was being done on a low noise gun design was directed toward application to the DCC. This work will be described here.

The theory of conversion gain as a function of intermediate frequency has been extended to the DCC case. It is a simpler analysis than the one described in Section 2.2 but still gives the essential behavior of the device. This also is described in this section.

Finally, a noise theory for the DDC, based upon the model described in Section 2.4 for the SCC, is presented.

5.2 Mechanical Design Considerations for the DCC

There are two changes which must be made to the basic design

of Figure 45 (Section 4.3) in order to make it into a DCC. First of all, the two circuits must be d-c isolated so that a potential difference may be maintained between them. This means that one of the circuits also must be isolated from the shell. This can be done most conveniently with the amplifier circuit which is closer to the gun (and the stem), than the oscillator circuit. Figure 58 shows a transverse cross-section of the shell and circuit (with circuit block). Four square notches have been broached the length of the shell and these notches accurately position the square cross-section circuit block. This is the method used for the SCC and for the oscillator section of the DCC. It is shown in Figure 58a. Figure 58b shows the method for the amplifier section of the DCC. The corners of the circuit block have been cut with square notches the full length of the block. Four ceramic rods with square cross-sections align and isolate the amplifier circuit. Isolation at either end of the amplifier circuit block can be done with mica shims. Only small spacings are required as the potential difference between amplifier and oscillator (or shell) should never exceed a few hundred volts.

The second change in design is with regard to the waveguides; four are needed now instead of two. This means the output block must be changed to accommodate a waveguide every $90°$ around a circle instead of every $180°$. In addition, the oscillator circuit block must have two more narrow height waveguides cut its full length in order to carry the r-f energy to and from the amplifier circuit block. A possibility for mismatch exists because of the gap required for d-c isolation between the oscillator and amplifier circuit blocks. Some tests were made at 35 Gc/s using quartz wedges to couple across a gap. It was

(a) Non-isolated
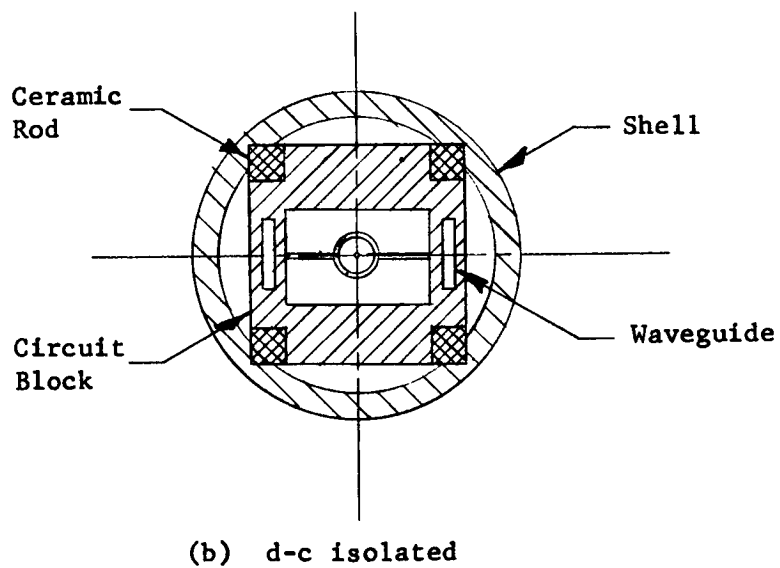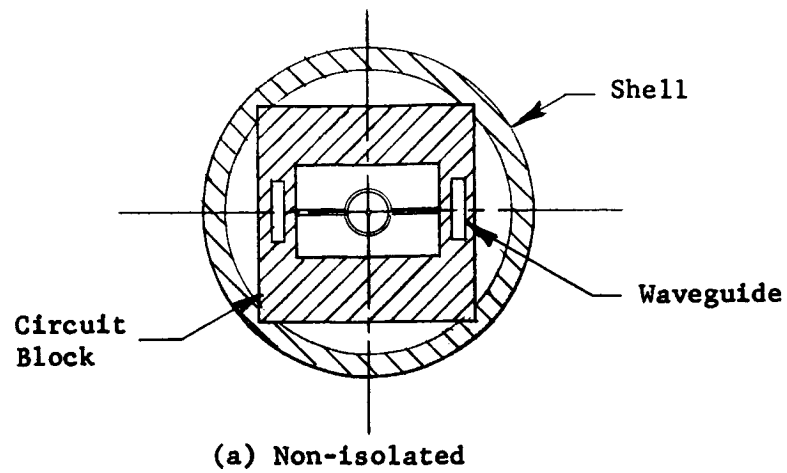
(b) d-c isolated

Figure 58. Transverse cross-section of shell and circuit showing
d-c isolated and non-isolated circuit mountings

discovered that, with the short gaps of interest here, no wedges are needed and effective coupling still can be maintained.

5.3 Low Noise Gun Design

5.3.1 Theoretical Considerations

Noise figure is defined as the ratio of signal power to noise power at the input divided by the ratio of signal power to noise power at the output, that is

$$F = (S_i/N_i)/(S_o/N_o)$$

$$= 1 + P_n/(GkT\Delta f) \qquad (5-1)$$

where G is the power gain, k is Boltzmann's constant, T is the absolute temperature, Δf is the bandwidth, and P_n is the output noise power due to noise sources within the tube.

Considering only noise due to the beam, the noise figure may be expressed as

$$F = 1 + \left[I_o/(G4C^3 V_o kT\Delta f) \right] \sum_i \left| V_{ci} \right|^2 \qquad (5-2)$$

where V_o and I_o are the d-c beam voltage and current, respectively, C is Pierce's gain parameter and V_{ci} is the output circuit voltage due to the ith source of noise on the beam. Currie and Forster[15] write Equation (5-2) in the form

$$F = 1 + \left[I_o/(4V_o CkT\Delta f) \right] \sum_i \left| A\hat{V}_{bi} - j\ WB\hat{I}_{bi} \right|^2 \qquad (5-3)$$

where W is the characteristic beam impedance, $(\omega_q 2 V_o)/(\omega I_o)$, A and B are complex functions of QC and d, and $\hat{V}_{bi}$ and $\hat{I}_{bi}$ are the rms noise voltage and current, respectively, on the beam at the circuit entrance,

due to the ith source of noise at the potential minimum.

There are assumed to be two uncorrelated sources of noise at the potential minimum: shot noise, which, if smoothing is ignored, is given by

$$\overline{\left|I_a\right|^2} = 2eI_0\Delta f \tag{5-4}$$

and velocity fluctuations which are given by Rack[16] as

$$\overline{\left|v_a\right|^2} = (4-\pi)(e/m)kT_c\Delta f/I_0 \tag{5-5}$$

where T_c is the cathode temperature. These sources give rise to a standing-wave of noise current along the beam having a standing-wave ratio, η, and a plasma angle, γ, between the standing-wave minimum and the circuit entrance.

It can be shown that Equation (5-3) has a minimum value given by

$$F_{min} = 1 + \sqrt{\pi(4-\pi)}(T_c/T)\sqrt{QC}\left|I_m(AB^*)\right| \tag{5-6}$$

when

$$\eta = \eta_{opt} = (1/2)\left[|A|^2 + |B|^2 + |A^2 + B^2|\right]/\left|I_m(AB^*)\right|$$

and

$$\gamma = \gamma_{opt} = (1/2)\left[\gamma + (2n+1)\pi\right], \qquad n = 0, \pm 1, \pm 2, \ldots.$$

where

$$\gamma = \tan^{-1}\left[2\ Re(AB^*)\right]/(|A|^2 - |B|^2)$$

Currie and Forster give curves for F_{min}, $\eta_{opt.}$, and $\psi_{opt.}$ in terms of QC and circuit loss. Values of QC at the start of oscillation have been calculated and it is assumed that QC for the BWA will not be far from these. The maximum value of circuit loss considered in Reference 15 is 10 db and extrapolation has been used to obtain figures for the assumed 15 db loss of the proposed circuit. The calculated values are given in Table 5. The cathode temperature has been taken as 1100°C

f (Gc/s)	QC -	$\eta_{opt.}$ -	$\psi_{opt.}$ (degrees)	$F_{min.}$ (db)
55	0.94	1.1	?	13.3
62.5	0.20	1.8	-75	13.8
75	0.06	5.	-32	14.6

Table 5. Minimum noise figure values over the frequency band.

(T_c = 1373). The small values of $\eta_{opt.}$ at the low frequency end of the band indicate that the phase of the standing-wave in this region will not be important.

5.3.2 Design Considerations

The basic low noise gun is shown in Figure 59. Its purpose is to transform the noise standing-wave excited at the potential minimum in the diode region to the desired values of ψ and η at the circuit entrance (the end of the drift tube). The three main regions of the gun may be considered separately.
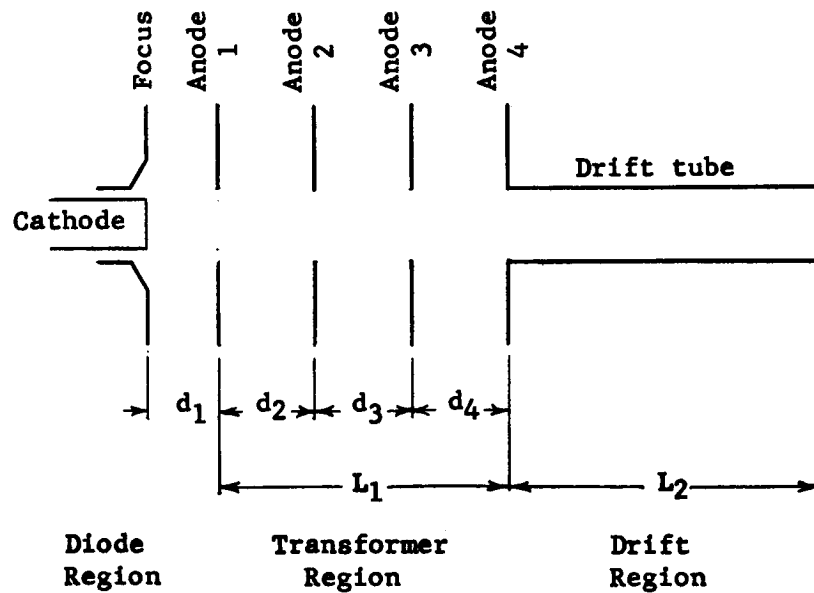
Figure 59. Basic low noise gun.

The diode region is considered first. The cathode specifications were evolved in Section 4. The cathode diameter is 0.017 inches. The cathode current density is 4 Amp/cm^2 giving a total beam current of 5.85 mAmp.

The grid is designed for Pierce parallel flow but in practice the potential usually is increased to give conditions of 'quasidivergent' flow. The reasons for this are explained in detail by Knechtli and Beam[17], the idea being to reduce the rapid rate of change of beam impedance in the diode region. By allowing the cathode to protrude through the grid, greater control over the fields at the cathode surface is obtained. For the same reason the grid taper angle is often decreased but it has been kept at 67-1/2° for this gun.

The first anode distance, d_1, should be as small as possible in order to keep the diode region at low potential and to give a large

voltage change between the first anode and the circuit. This allows voltage changes on later anodes to have more effect on the standing wave. A recommended minimum value for d_1 is twice the cathode diameter.

With the diode spacing and cathode current density specified, the first anode voltage, V_1, is fixed by the Child-Langmuir law,

$$J_o = 2.335 \times 10^{-6}(V_1)^{3/2}/(d_1)^2$$

If d_1 is chosen as 0.030 in., then $V_1 = 460$ volts. For quasi-divergent flow, this value usually is reduced by 20% and 350 volts may be taken as a typical value.

The purpose of the transformer region is to change the beam impedance at the diode to that required at the circuit. An empirical expression for the overall length of this region, L_1, is given in Reference 17. It corresponds to an exponential increase in beam impedance between the first anode and the drift tube. For this case, L_1 is given by

$$L_1 = \ln\left[(p_4/p_1)(V_4/V_1)^{3/4}\right]/\bar{\beta} \tag{5-7}$$

where p is the plasma frequency reduction factor and

$$\bar{\beta} = 2\pi(\lambda_{q1} - \lambda_{q4})^{-1/2}$$

where λ_q is the reduced plasma wavelength. For a BWA, V_4 varies over a wide range. In the present case the required value of L_1 varies over the band as shown in Table 6. L_1 has been fixed at 0.130 in. and it is hoped that it will be possible to optimize the noise performance at the band edges by adjustment of the voltages on the second and third anodes. In fact, L_1 is not too critical and the value given by Equation (5-7)

f (Gc/s)	V_4 (volts)	L_1 (inches)
50	600	0.025
65	2000	0.126
75	5000 (approx.)	0.300

Table 6. Required impedance transformer lengths over the frequency band.

represents a compromise between two contradictory requirements:

1. The transformer region should be long, for flexibility; and

2. The transformer region should be short, to avoid an increase in noise due to higher-order space charge waves.

In designing the transformer region, the number and placement of the anodes must be considered as well as the aperture size and the anode voltages. All the papers consulted indicate that two independent anodes (between the first anode and the drift tube) are sufficient. More anodes give increased flexibility but there is a danger of increased noise due to lens effects[18]. There seems to be little or no advantage in making the anode separations anything but equal, that is, $d_2 = d_3 = d_4$. The anode apertures should not be less than twice the beam diameter, to avoid lens effects (which increase the noisiness of the beam) and not much greater than the distance of the adjacent anodes, to avoid field penetration from one region to another. The entrance to the drift tube is stepped to avoid the sharp change in potential profile which would otherwise occur at this point. The anode voltages are initially set for a linear potential rise, which

corresponds, approximately, to an exponential increase in beam impedance. In practice V_2 and V_3 are adjusted to obtain the required values of ψ and η .

The final region to be considered is the drift tube. The length of the drift tube, L_2, only affects the value of ψ which, as we have seen, is not critical over most of the band. Ideally, L_2 would be such that $\psi = \psi_{opt}$, but this can be achieved only for fixed values of the anode voltages. It seems reasonable to start by making $L_2 \approx L_1$ (cf., for example, Fank's 38 Gc/s tube[19]). Greater flexibility can be obtained by isolating the drift tube from the circuit. In this way a small voltage difference between circuit and drift tube allows coarse adjustment of ψ without much variation in η . However, to avoid the constructional difficulties, this modification will not be incorporated at this stage.

A cross-sectional view of a gun design based on these considerations is shown in Figure 60. The important dimensions also are shown in Figure 60.

5.3.3 Measurements

In order to check the beam transmission of the low noise gun three beam tester tubes have been built in which the gun was coupled to a 1-1/2 in. length of 0.020 in. diameter drift tube. To date, the maximum transmission measured has been 60%. This was for a magnetic field of 5000 gauss. For low noise operation, the beam transmission must be improved to better than 90% and further tests are planned.
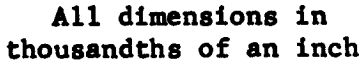
Figure 60. Cross sectional view of low noise gun design.

5.4 Conversion Gain

The derivation of the difference frequency current for the DCC, i_{d2}, is based on a simpler model than the derivation for the SCC (Section 2.2). The DCC is treated only for the case of large QC, where the fast space charge wave can be neglected, and for zero loss. As pointed out in Section 2.2, Equations (2-1) through (2-6) are applicable to both the SCC and the DCC. It is in the derivation of the space charge waves that the two devices diverge. The derivation of the space charge waves for the DCC is given in Appendix E. Also

given in Appendix E is the solution for i_{d2}. It may be written as

$$i_{d2} = \sqrt{CI_o/V_o} \; \left| B_{qs}(L_1) \right| H_2 \qquad (5-8)$$

where C is Pierce's gain parameter, I_o and V_o are the d-c beam current and voltage, respectively, $B_{qs}(L_1)$ is the amplitude of the slow space charge wave (at frequency f_s) at the end of the first (amplifier) helix, and H_2, a complicated function of the system parameters, is given by Equation (E-3). The amplitude of the space charge wave is nearly equal to the square root of the power available at the output of the amplifier. Thus, if P_s is the input power to the amplifier helix at f_s and g_a is the total r-f power gain of the amplifier, then

$$\left| B_{qs}(L_1) \right|^2 \approx P_s g_a$$

The variation of conversion gain with difference frequency can be seen in curves of normalized i-f current, H_2, as a function of normalized difference frequency, f_d/f_o. Figures 61 and 62 show the variation of H_2 with f_d/f_o for two values of ω_{qd}/ω_d: 0.01 and 0.07. The other parameters, QC, C and α_o have the same values for both curves (1, 0.01, and -1 respectively) where α_o is the ratio of the d-c velocity to the group velocity of the circuit wave, that is, $\alpha_o = U_o/v_g$. The curves show very sharp peaks for small values of f_d/f_o. The curve in Figure 63 has the same values for the parameters as Figure 62 except for QC which is now 2. The curve shows that H_2 (and hence, i_{d2}) varies only very slightly with QC. Figure 64 changes the value of C to 0.05 compared to Figure 62 and shows that H_2 does not depend markedly on C either. Finally, Figure 65, compared with Figure 62 alters α_o to -2 and the sharp peak is seen to disappear.
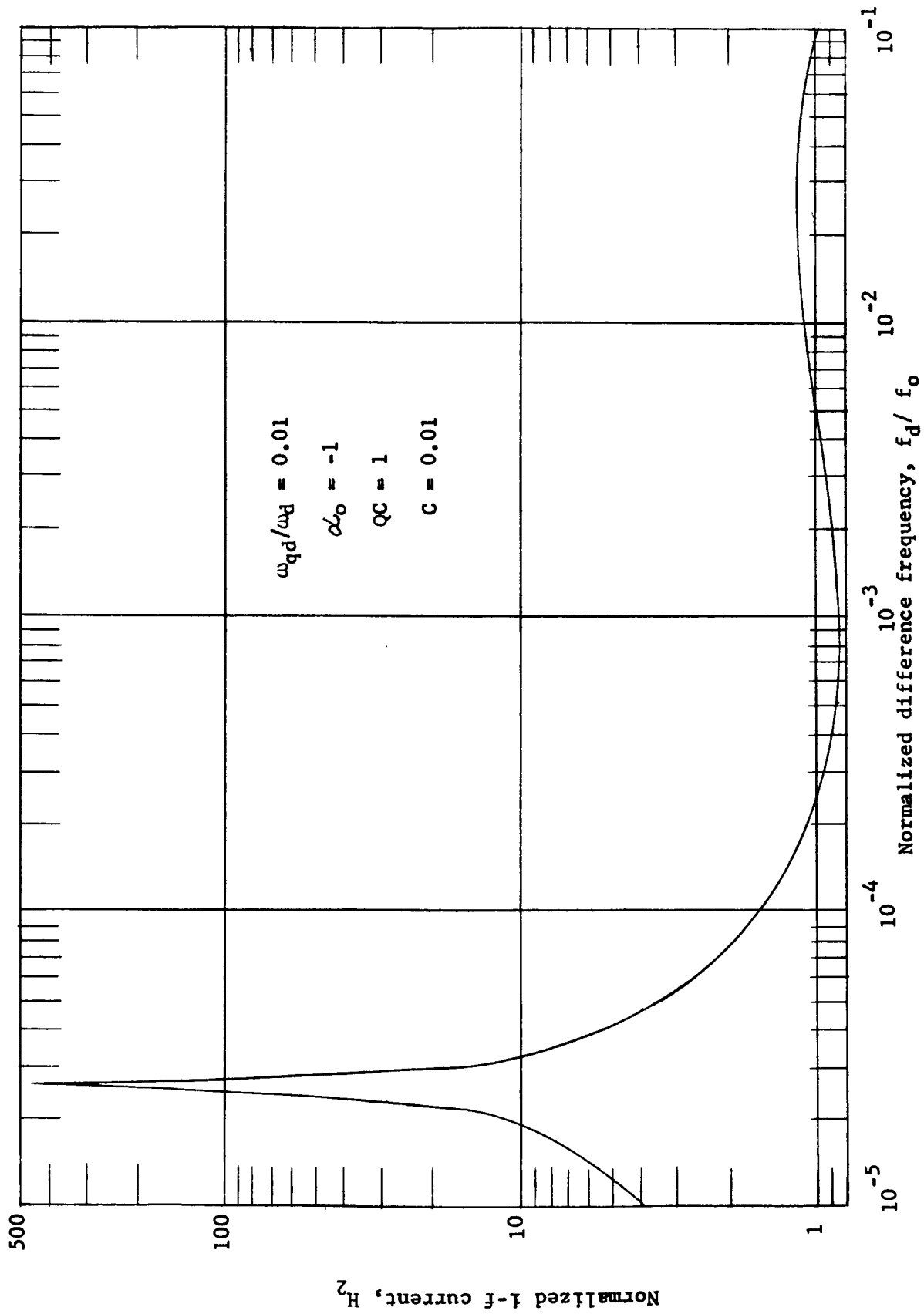
Figure 61. Normalized 1-f current as a function of normalized difference frequency for a DCC
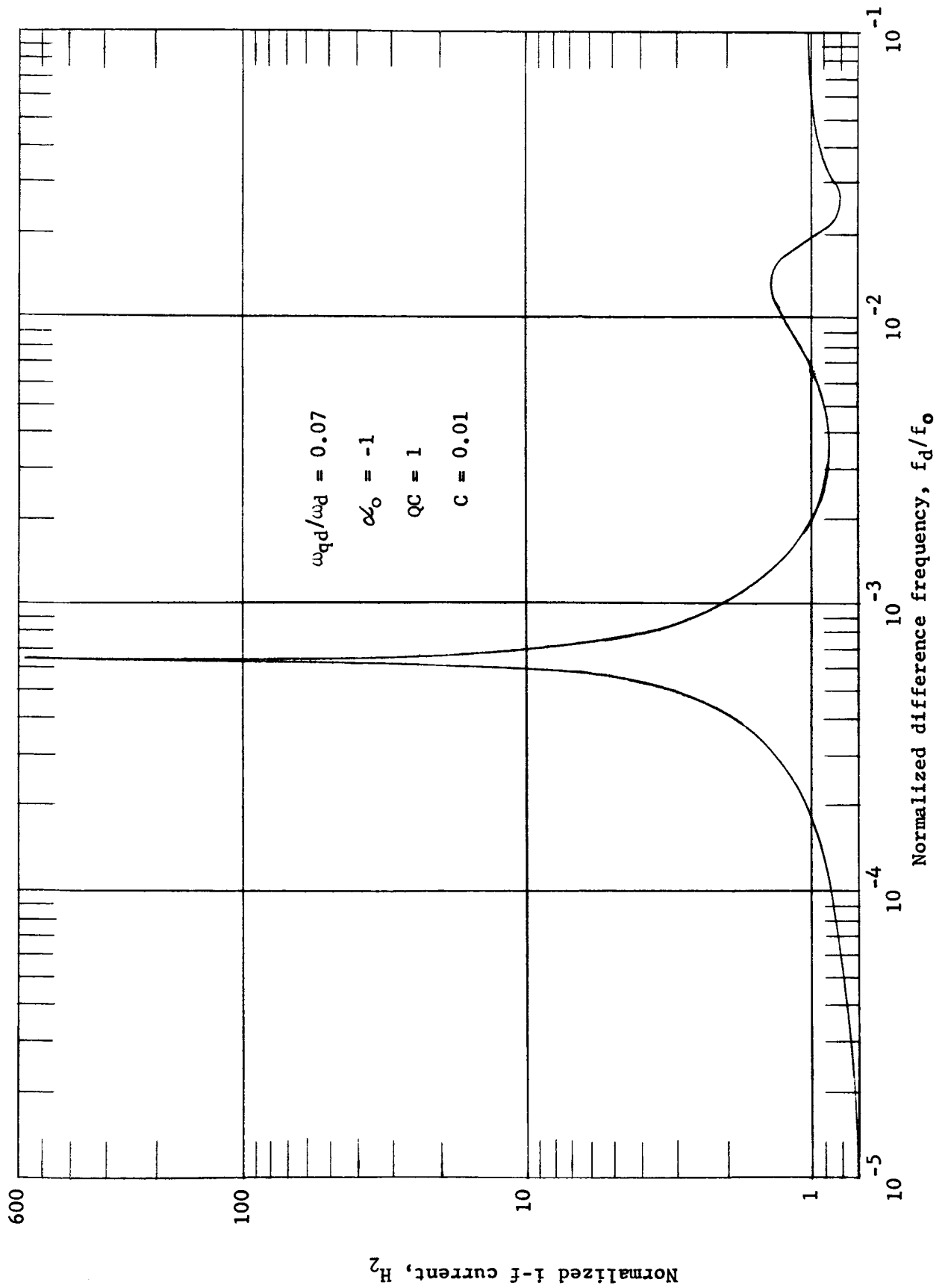
Figure 62. Normalized i-f current as a function of normalized difference frequency for a DCC

The chart shows:

Normalized i-f current, H_2 (vertical axis): 600, 100, 10, 1

Normalized difference frequency, f_d/f_0 (horizontal axis): 10^{-5}, 10^{-4}, 10^{-3}, 10^{-2}, 10^{-1}

Parameters shown on chart:

$\omega_{qd}/\omega_{qm} = 0.07$

$\alpha_0 = -1$

$QC = 1$

$C = 0.01$
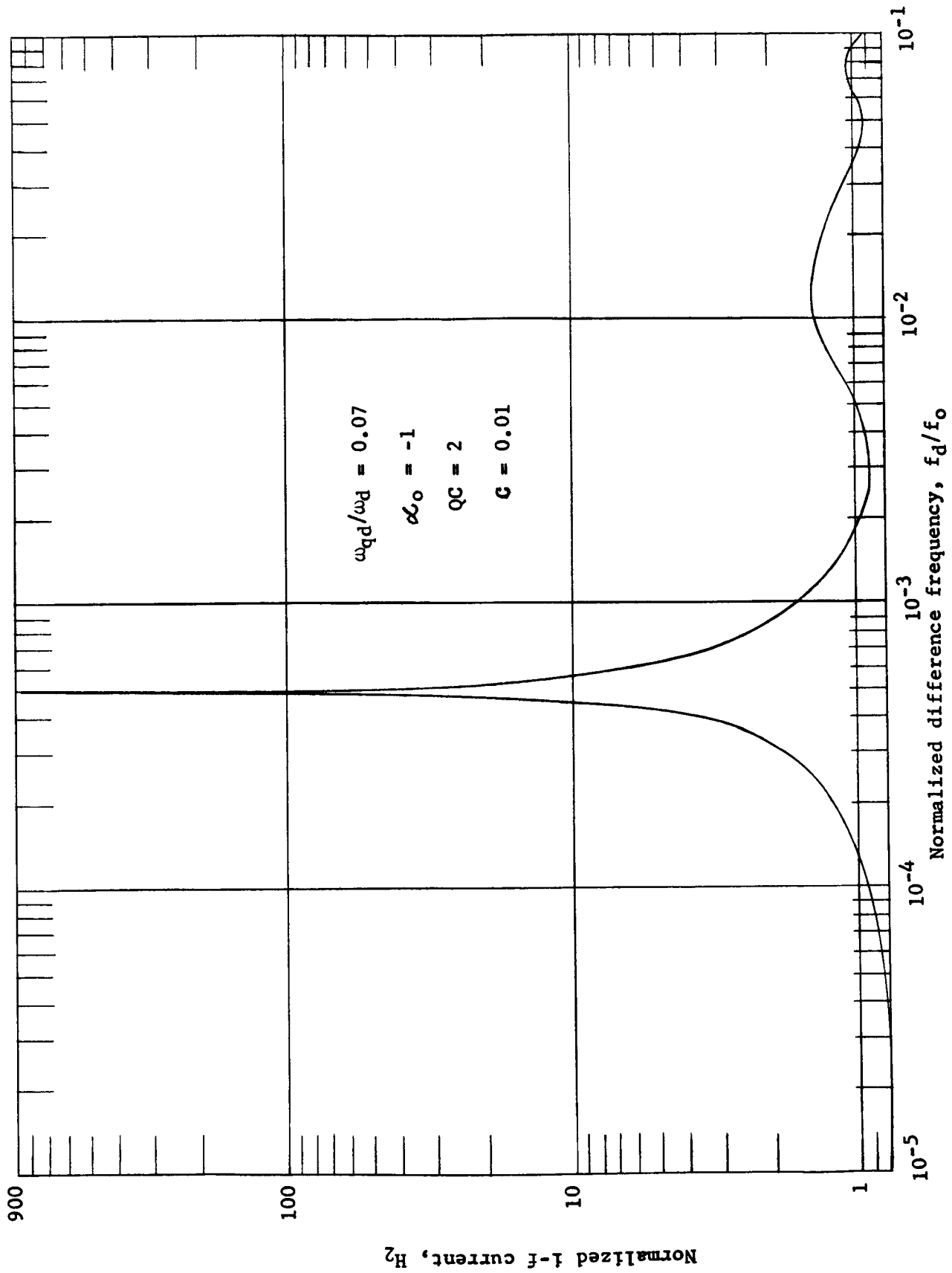
Figure 63. Normalized i-f current as a function of normalized difference frequency for a DCC

Normalized difference frequency, f_d/f_o

Normalized i-f current, H_2

$\omega_{qd}/\omega_{pd} = 0.07$

$\alpha_o = -1$

$QC = 2$

$G = 0.01$
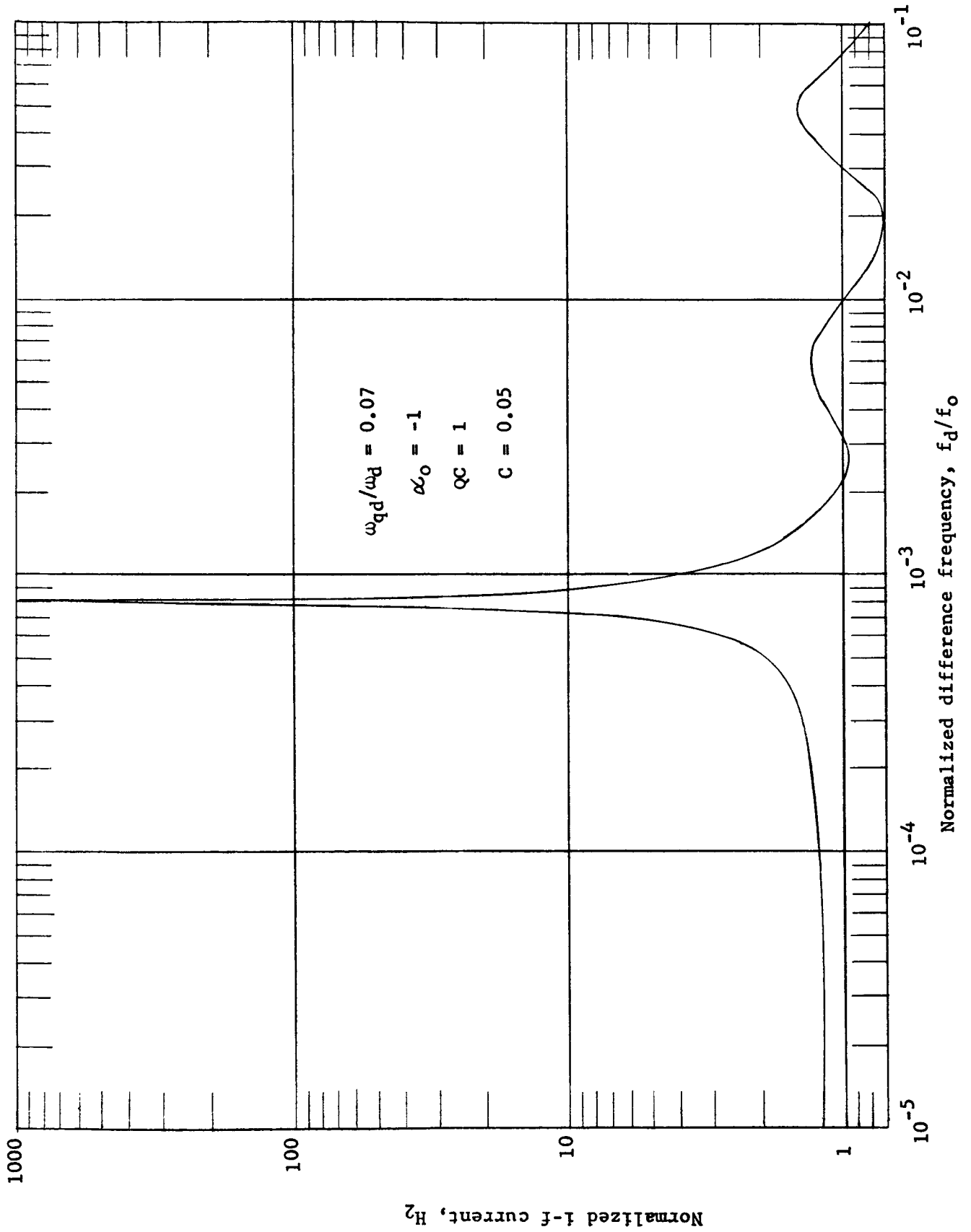
Figure 64. Normalized i-f current as a function of normalized difference frequency for a DCC

The chart shows:

$\omega_{qd}/\omega_d = 0.07$

$\alpha_o = -2$

$QC = 1$

$C = 0.01$

Y-axis: Normalized i-f current, H_2

X-axis: Normalized difference frequency, f_d/f_o
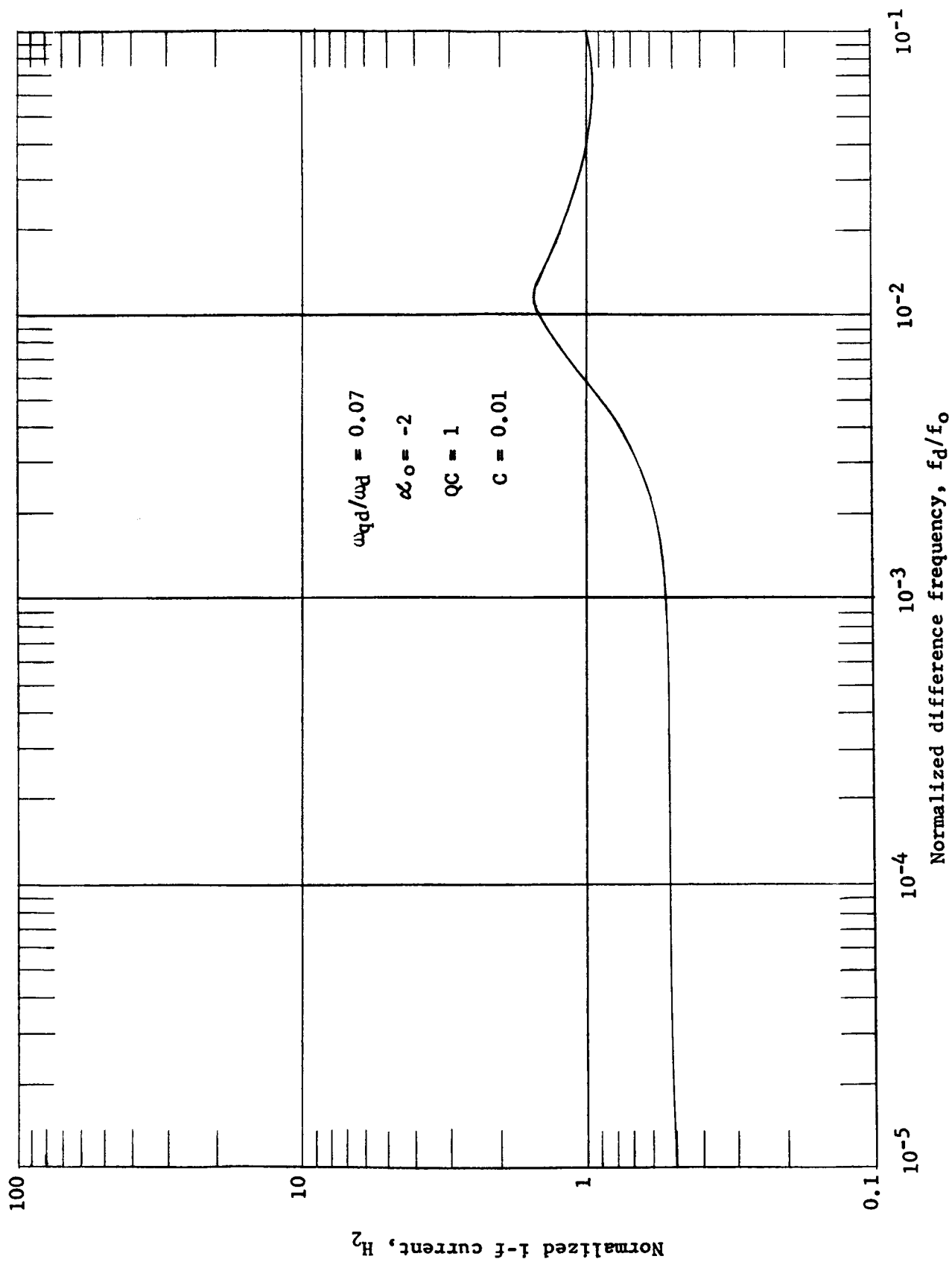
Figure 65. Normalized i-f current as a function of normalized difference frequency for a DCC

These results show a most striking behavior, where, for certain values of the parameters, very sharp peaks of H_2 occur (for small f_d). The reason for these peaks is thought to be as follows: The electron beam is a plasma which can propagate free space charge waves at the frequency f_d. These waves travel with phase velocities

$$v_p = U_0 \left[1 \pm (\omega_{qd}/\omega_d) \right]^{-1}$$

The beam will also propagate other waves at f_d - the forced solutions - due to the mixing of the signals at f_o and f_s. In fact the model shows that there are four of these forced waves, that is,

$$\sum_{i=1}^{4} \beta_i' \exp(j\xi_i z)$$

The peaks are produced when one of these waves has the same phase velocity as one of the free waves, that is,

$$\beta_d \pm \beta_{qd} = \xi_i + \beta_d$$

or

$$\pm \beta_{qd} = \xi_i \qquad (5\text{-}9)$$

Equation (5-9) shows why the peaks are so sharp since both β_{qd} and ξ_i vary at the same time so that equality will only be approached for a narrow range of the parameters. The peaks were not produced for the SCC simply because the values of the parameters were not taken in the necessary range.

Finally, as in Section 2.2, a specific example of a millimeter device is given. The same data is used, that is,

$$\Omega = 10 \text{ db} \qquad\qquad f_o = 62 \text{ Gc/s}$$

$$I_o = 2.95 \text{ mAmp} \qquad\qquad f_s = 64 \text{ Gc/s}$$

$$V_o = 1680 \text{ volts} \qquad\qquad R = 5 \times 10^5 \text{ ohms}$$

$$K_1 = 0.692 \text{ ohms} \qquad\qquad C = 0.006715$$

$$QC = 0.0253$$

The conversion gain is given by

$$g_2 = (1/8) \left| i_{d2} \right|^2 R/P_s$$

where

$$\left| i_{d2} \right|^2 / P_s = (CI_o) g_a \left| H_2 \right|^2$$

H_2 was calculated for large QC and zero loss. Assuming the dependance of H_2 on QC and Ω is similar to the behavior of H_1, we obtain

$$H_2 = 0.45$$

If the amplifier has a gain of 30 db, then

$$G_2 = -8 \text{ db}$$

5.5 Noise Theory

If we use the same noise model that was used in Section 2.4, the noise figure for the DCC may be written directly from Equation (2-21a). Two changes are required. First, the DCC has good image rejection, consequently, the 2 in the denominator of the last term in Equation (2-17) must be removed. This implies multiplying the last term of Equation(2-21a) by 2. Second, H_1^2 is replaced by $g_a H_2^2$. Therefore, the noise figure F_2, is given by

$$F_2 = F_A + 7.72(T_C/T)Vo/(V_{A1}Cg_aH_2^2) \qquad (5\text{-}10)$$

For the millimeter wave device example of Section 2.4, the noise figure was

$$F_1 = F_A + 4 \times 10^7$$

For the same example with a DCC, the noise figure is

$$F_2 = F_A + 10^2$$

If an amplifier noise figure of 15 db can be obtained, as suggested in Section 5.3.1, then

$$F_2 \approx 21 \text{ db}$$

6. CONCLUDING REMARKS

6.1 Conclusions

An exhaustive study, both theoretical and experimental, of the conversion gain of a single circuit converter was performed as Task A of this contract. Two main conclusions may be drawn from the results of this study. First, the experimental verification of the theory, as presented in Figures 17 and 18, demonstrates that this theory of the single circuit converter, based on a space charge wave analysis, satisfactorily describes the behavior of the device. Second, the single circuit converter, because it is both simple to construct and operate, is a useful swept receiver front end in high signal level applications, but, because of low conversion gain and high noise figure, cannot be used in low level applications.

The experimental results of Task B for dispersion and interaction impedance show that plane circuits can be deformed without unduly impairing their properties. The high impedance and large bandwidth of the plane meander line are not greatly diminished by the introduction of a small beam tunnel at the center of the bars; the main effect is a reduction in the interaction impedance at the low frequency end of the range by a factor of about five. The results also show that theoretical calculations for the plane meander line circuit may be used as a guide in designing the modified circuits. The large diameter circuits showed strong anti-symmetric modes which were not apparent in the circuits with smaller beam tunnels. The circuit with the small, semi-circular beam tunnel is relatively easy to make but this advantage is offset by low

impedance and reduced interaction area. The selection of a particular configuration must be determined by beam-circuit considerations.

Two tube types, which were different both in mechanical design and in the choice of slow-wave circuit, were built and tested for Task C. One type was designed as a laboratory vehicle and used a full circular, 0.020 in. beam tunnel diameter, slow-wave circuit. The tube oscillated with a minimum of 10 mW. of output power from 67 to 75 Gc/s. A maximum of 33 mW at 69 Gc/s was achieved. Meaningful conversion gain measurements were not possible with this tube but the results have demonstrated that the meander line with a circular beam tunnel can be used successfully in the 50 to 75 Gc/s region of the spectrum. Modifications to the design will be required if full band coverage is to be attained.

The other tube type built for Task C was designed as a prototype model and used a semi-circular, 0.020 in. beam tunnel diameter, slow-wave circuit. The fact that it was not possible to obtain oscillations indicated that the original estimates for the interaction impedance of this circuit were high. This was later confirmed by the final results of Task B. The good beam transmission through this tube indicates that the basic mechanical design is adequate and that alignment problems have been overcome. The obvious next step is to incorporate the full-circular circuit into the prototype mechanical design. We are doing just that under an ITT internally funded program.

Four items relating to double circuit converters were studied under Task D. The first concerned the mechanical design and the conclusion reached was that, although double circuit converters are more difficult to build than single circuit converters, there appear to be

no insuperable design problems. The second concerned the design of a low noise gun which indicated the noise figure of the amplifier section of the converter could be maintained below 15 db across the frequency band.

The third item dealt with the conversion gain of the double circuit converter. Two main features resulted from this study. First, the conversion gain of the double circuit converter, in contrast to the single circuit converter, does not approach zero for increasing difference frequency but can be maintained at relatively high values. Second, high peaks in conversion gain occur for low values of difference frequency. It is tempting to try to make use of this enhanced interaction but this is unlikely to be practicable for three reasons:

1. the peak is very narrow and may be greatly reduced when losses are taken into account,

2. it occurs at low values of f_d, and

3. the frequency at which it occurs will vary with the beam voltage, which has to be swept.

Further study would be required to see whether the phenomonon could be usefully exploited.

Finally, the noise theory predicts that an overall noise figure for the double circuit converter can be nearly 20 db. This requires an amplifier noise figure in the neighborhood of 15 db or less.

In summary, two major conclusions can be reached. First, a meander line deformed to accommodate cylindrical beams can be a useable millimeter wave slow wave circuit. Second, swept receivers for low signal levels require a double circuit rather than a single circuit converter.

6.2 Recommendations

We are continuing work on a modified Task C tube to be operated as a BWO in the 50 - 75 Gc/s frequency range. It will combine the mechanical features of the ETL design with the full circular slow-wave circuit design of the STL tube. Some design modifications to the circuit remain to be made to attain full band coverage. Based on the evidence presented in this report we recommend that work on milli-meter wave converter tubes be continued and propose that the next logical phase in this program is to build operating double circuit backward-wave converters in the 50 - 75 Gc/s frequency range.

7. REFERENCES

1. R. W. DeGrasse, "Frequency Mixing in Microwave Beam-Type Devices," Stanford Elec. Lab. Technical Rpt. No. 386-2; July 28, 1958.

2. G. M. Branch and T. G. Mihran, "Plasma Frequency Reduction Factors in Electron Beams," IRE Trans. on Electron Devices, Vol. ED-2, pp 3-11; April 1955.

3. "Nomograph for Helix Backward-Wave Oscillators with Hollow Beams," ERL Drawing No. D-26235, Stanford University, Stanford, California; December 2, 1954.

4. Aldert van der Ziel, Noise, Prentice-Hall, Inc., Englewood Cliffs, N. J., p 97; 1954.

5. Arthur Karp, "Traveling-Wave Tube Experiments at Millimeter Wave-lengths with a New, Easily Built, Space Harmonic Circuit," Proc. IRE, Vol. 43, pp 41-46; January 1955.

6. R. C. Fletcher, "A Broad Band Interdigital Circuit for Use in Traveling-Wave Type Amplifiers," Proc. IRE, Vol. 39, pp 951-958; August 1952.

7. E. A. Ash and A. C. Studd, "A Ladder Structure for Millimeter Waves," IRE Trans. on Electron Devices, Vol. ED-8, pp 294-302; July 1961.

8. J. R. Pierce, Traveling-Wave Tubes, D. Van Nostrand Co., New York, New York; 1950.

9.   J. C. Slater, <u>Microwave Electronics</u>, D. Van Nostrand Co., New York, New York, pp 80-82; 1950.

10. E. L. Ginzton, <u>Microwave Measurements</u>, McGraw-Hill Book Co., New York, New York, pp 438-440; 1957.

11. R. Lagerstrom, "Interaction Impedance Measurements by Perturbation of Traveling Waves," Stanford Electronic Laboratory Report No. TR7; February 1957.

12. "The Philips Impregnated Cathode," <u>Philips Metalonics Technical Bulletin</u>, PM 101.

13. H. R. Johnson, "Backward-Wave Oscillators," <u>Proc. IRE</u>, Vol. 43, pp 684-697; June 1955.

14. M. I. Antonion, F. E. Gifford, and A. G. Peifer, "Development of Millimeter-Wave Backward-Wave Oscillator Tubes; 35-75 KMC," WADC Technical Report 59-401, Bendix Aviation Corporation, pp 5-11; September 1959.

15. M. R. Currie and D. C. Forster, "Conditions for Minimum Noise Generation in Backward-Wave Amplifiers," <u>IRE Trans. on Electron Devices</u>, Vol. ED-5, pp 88-98; April 1958.

16. A. J. Rack, "Effect of Space Charge and Transit Time on the Shot Noise in Diodes," <u>Bell System Tech. Jour.</u>, Vol. 17, pp 592-619; October 1938.

17. R. C.Knechtli and W. R. Beam, "Performance and Design of Low-Noise Guns for Traveling-Wave Tubes," <u>RCA Review</u>, Vol. 17, pp 410-424; September 1956.

18. R. C.Knechtli, "Effect of Electron Lenses on Beam Noise," IRE Trans. on Electron Devices, Vol. ED-5, pp 84-88; April 1958.

19. F. B. Fank, "Design of Low Noise Guns for Traveling-Wave Tubes," Microwave Jour., Vol. 4, pp 55-60; February 1961.

20. L. Solymar, "Some Properties of Three Coupled Waves," IRE Trans. on Microwave Theory and Techniques, Vol. MTT-8, pp 284-291; May 1960.

21. A. W. Horsley and A. Pearson, "Measurement of Dispersion and Interaction Impedance Characteristics of Slow-Wave Structures by Resonance Methods," Standard Telecommunications Laboratories, Ltd., Technical Memo No. 400; February 1965.

APPENDIX A

Derivation of the Space Charge Waves and

the Solution of DeGrasse's Equations for the SCC

The interaction between an external electromagnetic field

and an electron beam is described by the three coupled equations[19]

$$-dA_c/dz = j\beta_c A_c + jd_{cf}A_f + jd_{cq}A_q \qquad \text{(A-1)}$$

$$-dA_f/dz = -jd_{cf}A_c + j\beta_f A_f \qquad \text{(A-2)}$$

$$-dA_q/dz = -jd_{cq}A_c + j\beta_q A_q \qquad \text{(A-3)}$$

where A_c, A_f, and A_q represent respectively the circuit wave (external

field), the fast and slow space charge waves, and β_c, β_f, and β_q are

the propagation coefficients of these waves. d_{cf} and d_{cq} are the

coupling constants between the circuit wave and the fast and slow space

charge waves respectively. In terms of Pierce's space charge (QC) and

gain (C) parameters, these quantities may be written

$$\beta_c = \beta_e(1 + Cb) + j\beta_e Cd$$

$$\beta_f = \beta_e(1 - 2C\sqrt{QC})$$

$$\beta_q = \beta_e(1 + 2C\sqrt{QC})$$

$$\beta_e = \omega/U_0$$

$$d_{cf} = d_{cq} = (1/2)\,\beta_e C(QC)^{-1/4}$$

where ω is the radian frequency of the external field and U_0 the d-c

velocity of the electron beam. b is related to the phase velocity of the structure, v_p, by the expression

$$v_p/U_o = 1/(1 + Cb)$$

d is related to the circuit losses by the expression

$$\alpha = \beta_e Cd = 0.05(\ln 10)(\Omega/L)$$

where Ω is the total cold loss of the circuit and L is its length.

The boundary conditions for the coupled equations are

$$A_c(0) = 1 \ , \quad A_q(0) = A_f(0) = 0$$

that is, initially all the energy is contained in the circuit wave. With these conditions, the solutions can be written

$$A_c = \exp(-j\beta_e z) \left[\frac{\delta_1{}^2 + 4QC}{(\delta_1 - \delta_2)(\delta_1 - \delta_3)} \right] \exp(2\pi CN\delta_1 z/L) + \text{cyclic terms} \quad \text{(A-4)}$$

$$A_f = - \frac{\exp(-j\beta_e z)}{2(QC)^{1/4}} \left[\frac{-j\delta_1 + 2\sqrt{QC}}{(\delta_1 - \delta_2)(\delta_1 - \delta_3)} \right] \exp(2\pi CN\delta_1 z/L) + \text{cyclic terms} \quad \text{(A-5)}$$

$$A_q = - \frac{\exp(-j\beta_e z)}{2(QC)^{1/4}} \left[\frac{j\delta_1 + 2\sqrt{QC}}{(\delta_1 - \delta_2)(\delta_1 - \delta_3)} \right] \exp(2\pi CN\delta_1 z/L) + \text{cyclic terms} \quad \text{(A-6)}$$

where δ_1, δ_2, and δ_3 are the roots of the cubic equation[13]

$$\delta^3 + \delta^2(jb - d) + 4QC\delta + 4QC(jb + d) - j = 0 \quad \text{(A-7)}$$

In order to solve the DeGrasse equations, Equations (2-1) and (2-2), it is necessary to write Equations (A-5) and (A-6) for both the oscillator frequency, f_o, and the signal frequency, f_s. These expressions for A_{fo}, A_{qo}, A_{fs}, and A_{qs} are substituted into Equations (2-3) through (2-6) which are used in turn to solve Equations (2-1) and (2-2) subject to the boundary conditions

$$v_d(0) = i_d(0) = 0$$

Equations (A-5) and (A-6) may be written more conveniently as[+]

$$A_{fo} = D_1 \exp\left[2\pi(CN)_o \delta_1 z/L\right] + D_2 \exp\left[2\pi(CN)_o \delta_2 z/L\right] + D_3 \exp\left[2\pi(CN)_o \delta_3 z/L\right] \quad \text{(A-8)}$$

$$A_{qo} = E_1 \exp\left[2\pi(CN)_o \delta_1 z/L\right] + E_2 \exp\left[2\pi(CN)_o \delta_2 z/L\right] + E_3 \exp\left[2\pi(CN)_o \delta_3 z/L\right] \quad \text{(A-9)}$$

$$A_{fs} = F_1 \exp\left[2\pi(CN)_s \Delta_1 z/L\right] + F_2 \exp\left[2\pi(CN)_s \Delta_2 z/L\right] + F_3 \exp\left[2\pi(CN)_s \Delta_3 z/L\right] \quad \text{(A-10)}$$

$$A_{qs} = G_1 \exp\left[2\pi(CN)_s \Delta_1 z/L\right] + G_2 \exp\left[2\pi(CN)_s \Delta_2 z/L\right] + G_3 \exp\left[2\pi(CN)_s \Delta_3 z/L\right] \quad \text{(A-11)}$$

where the amplitude coefficients can be determined from Equations (A-5) and (A-6). For example

$$D_1 = -(1/2)(QC)_o^{-1/4} \exp(-j\beta_{es}z)\left\{\left[-j\delta_1 + 2\sqrt{(QC)_o}\right] / \left[(\delta_1 - \delta_2)(\delta_1 - \delta_3)\right]\right\}$$

and

$$G_2 = -(1/2)(QC)_s^{-1/4} \exp(-j\beta_{es}z)\left\{\left[-j\Delta_2 + 2\sqrt{(QC)_s}\right] / \left[(\Delta_2 - \Delta_3)(\Delta_2 - \Delta_1)\right]\right\}$$

where δ_1, δ_2, and δ_3 refer to the roots of the cubic

[+] b, QC, and CN are frequency sensitive and must be evaluated at f_s and f_o - hence the subscripts. C and d are not very frequency sensitive so that $C_s \approx C_o = C$ and $d_s \approx d_o = d$.

$$\delta^3 + \delta^2(jb_o - d) + 4(QC)_o\delta + 4(QC)_o(jb_o + d) - j = 0$$

under oscillation conditions, that is, $A_c(L) = 0$; Δ_1, Δ_2, and Δ_3 refer to the roots of the cubic

$$\Delta^3 + \Delta^2(jb_s - d) + 4(QC)_s\Delta + 4(QC)_s(jb_s + d) - j = 0$$

under amplification conditions, that is, $|A_c(L)|^2 = P_s$; and P_s is the input power to the circuit at f_s. The solution for i_{d1}, is

$$i_{d1} = g_s \sqrt{P_s P_o}/V_o \left\{ A'\exp(j\omega_{qd}z/U_o) + B'\exp(-j\omega_{qd}z/U_o) \right.$$
$$\left. + \sum_{m,n=1}^{3} (1/2)g_{mn} \exp\left[2\pi(CN)_o\xi_{mn}z/L\right] \right\} \quad (A-12)$$

where

$$A' = -(1/4) \sum_{m,n=1}^{3} \left\{ (\omega_d/\omega_o) \left[j(\omega_{qd}/\omega_o)(1/C\xi_{mn}) + 1 \right] g_{mn} \right.$$
$$\left. + (\omega_d/\omega_{qd}) \alpha_{mn} \left[1 - j(\omega_d/\omega_o)(1/C\xi_{mn}) \right] \right\}$$

$$B' = (1/4) \sum_{m,n=1}^{3} \left\{ (\omega_d/\omega_o) \left[j(\omega_{qd}/\omega_o)(1/C\xi_{mn}) - 1 \right] g_{mn} \right.$$
$$\left. + (\omega_d/\omega_{qd}) \alpha_{mn} \left[1 - j(\omega_d/\omega_o)(1/C\xi_{mn}) \right] \right\}$$

$$g_{mn} = \left[j3C\xi_{mn}\alpha_{mn} + (\omega_d/\omega_o) \alpha_{mn} + jC\xi_{mn}\beta_{mn} \right] \left[C^2\xi_{mn}^2 + (\omega_{qd}/\omega_o)^2 \right]^{-1}$$

$$\alpha_{mn} = (k_o k_s)^{-1/2}(D_m + E_m)(F_n + G_n)^*$$

$$\beta_{mn} = (k_o/k_s)^{1/2}(D_m - E_m)(F_n + G_n)^* + (k_s/k_o)^{1/2}(D_m + E_m)(F_n - G_n)^*$$

$$\xi_{mn} = \delta_m + \Delta_n^*(CN)_s/(CN)_o - j(\omega_d/\omega_o)(1/C)$$

P_o is the oscillation output power at f_o, and g_s is the gain of the device as an amplifier at f_s.

Both P_o and g_s are measurable quantities and the measured values may be used directly in Equation (A-12). If the measured values are not available, the oscillator power may be given by

$$P_o = CI_oV_o \exp(-\alpha L) \qquad (A-13)$$

As for the amplifier gain, it would be expected to be hyperbolic about the oscillator frequency. The gain at f_o is infinite, that is, a finite output is obtained for zero input. Thus, as f_d approaches zero (f_s approaches f_o), g_s will increase beyond all bounds. It is reasonable, therefore, to expect g_s to vary inversely as f_d for values of f_s near f_o. Thus, g_s may be expressed in the form

$$g_s = (Kf_d/f_o)^{-1} \qquad (A-14)$$

For f_s close to f_o, the circuit wave for the amplifier, A_{cs}, will be given by A_{co}, the circuit wave at oscillation, plus a term to the first order in f_d/f_o. Using such an expression, the gain was evaluated from

$$g_s = A_{cs}(0)/A_{cs}(L)$$

The expression for K is found to be

$$K = \left\{\left[\delta_1^2 + 4(QC)_o\right] / \left[(\delta_1 - \delta_2)(\delta_1 - \delta_3)\right]\right\} \left\{\left[2\delta_1\nu_1 + 8(QC)_o\right] / \left[\delta_1^2 + 4(QC)_o\right]\right.$$

$$\left. -(\nu_1 - \nu_2)/(\delta_1 - \delta_2) - (\nu_1 - \nu_3)/(\delta_1 - \delta_3) + \beta_e CL(\nu_1 - \delta_1)\right\} \exp(\beta_e C\delta_1 L)$$

$$+ \text{ cyclic terms} \qquad (A-15)$$

where

$$\mathcal{V}_i = (1/C)\left\{-j\delta_i^2\left[1 + U_o/v_g + C(b_o + jd)\right] + 8C\delta_i(QC)_o\right.$$

$$\left. + j4(QC)_o\left[1 + U_o/v_g + 3C(b_o + jd)\right]\right\} / \left[3\delta_i^2 + j2(b_o + jd) + 4(QC)_o\right]$$

for $i = 1$, 2, or 3.

Thus, the difference frequency current for the SCC, i_{d1}, may be written as

$$i_{d1} = \sqrt{P_s CI_o/V_o}\ H_1 \qquad\qquad (A-16)$$

where H_1, the normalized difference frequency current for the SCC, is given by

$$H_1 = (Kf_d/f_o)^{-1}\exp(-\alpha L/2)\left\{A'\exp(j\omega_{qd}z/U_o) + B'\exp(-j\omega_{qd}z/U_o)\right.$$

$$\left. + \sum_{m,n=1}^{3} (1/2)g_{mn}\exp\left[2\pi(CN)_o\xi_{mn}z/L\right]\right\} \qquad\qquad (A-17)$$

The expression for H_1 can be simplified for those cases where QC is high. For high QC, A_f, the fast space charge wave can be neglected. Thus, Equations (A-1) through (A-3) are reduced to two coupled equations. Under oscillation conditions, that is, $A_{qo}(0) = A_{co}(L) = 0$, the slow space charge wave is given by

$$A_{qo} = j2A_1\exp(\alpha)\exp(-j\beta_{qo}z)\sin\left\{d_{cq}^o\left[1 - (\alpha/2d_{cq}^o)^2\right]^{1/2}z\right\}$$

where d_{cq}^o means the coupling coefficient, d_{cq}, at f_o. Under amplification conditions, that is $A_{qs}(0) = 0$ and $\left|A_{cs}(L)\right|^2 = P_s$,

$$A_{qs} = jg_s\sqrt{P_s}\exp\left[-j(1/2)(\beta_{qs} + \beta_{cs} + j\alpha)z\ \sin\left\{d_{cq}^s\left[1\right.\right.\right.$$

$$\left.\left.\left. + (\beta_{qs} - \beta_{cs} - j\alpha)^2/(2d_{cq}^s)^2\right]^{1/2}z\right\}\right.$$

The gain is determined as above, except in this case, the circuit wave may be written as

$$A_{cs} = -\sqrt{P_s} \exp(-\alpha L/2) \exp\left[-j(1/2)(\beta_{qs} + \beta_{cs} + j\alpha)z\right]\left\{\eta \sin\left[(d_{cq}^s)^2\right.\right.$$
$$\left. + (\eta/2)^2\right]^{1/2}z + \left[(d_{cq}^s)^2 + (\eta/2)^2\right]^{1/2}\cos\left[(d_{cq}^s)^2 + (\eta/2)^2\right]^{1/2}z\right\}$$

where

$$\eta = \beta_{qs} - \beta_{cs} - j\alpha$$

Thus, in the expression for g_s, the value of K becomes

$$K = \exp(\alpha L/2)\left[1 - (\alpha/2d_{cq}^o)^2\right]^{-1}\left\{(9/4)(d_{cq}^o L + \alpha/2d_{cq}^o)^2\right.$$
$$\left. + \left[\sqrt{(QC)_o}/c^2\right](1 + U_o/v_g)^2(1 + \alpha L/2)^2\right\}^{1/2} \tag{A-18}$$

The DeGrasse equations may be solved with these expressions for the space charge waves, subject to the same boundary conditions as before, and the equation for H_1 becomes

$$H_1 = (QC)_o^{1/4}\exp(-\alpha L/2)\left\{2KC\left[1 - (\alpha/2d_{cq}^o)^2\right]\right\}^{-1}\left\{(2d_{cq}^o/\alpha)\left[\exp(\alpha L) - 1\right]\right.$$
$$\left. - (\alpha/2d_{cq}^{o2})\left[(\alpha^2/d_{cq}^{o2} - 3)\exp(\alpha L) - 1\right]\right\} \tag{A-19}$$

for QC large. This expression is further reduced in the lossless case to

$$H_1 = (\pi/2)\exp(-\alpha L/2)\left[1 + 3C\sqrt{(QC)_o}\right]\left[(3\pi C/4)^2/\sqrt{(QC)_o}\right.$$
$$\left. + (1 + U_o/v_g)^2\right]^{1/2} \tag{A-20}$$

for QC large and $\alpha = 0$.

APPENDIX B

Calculation from Measured Data of Amplifier Gain in the

Presence of Oscillation for a SCC

Referring to Figure 11 in Section 2.3, an output power, P_{Ai}, of the HP oscillator is related to the dbm_{Ai} output reading by

$$dbm_{Ai} = 10 \log P_{Ai} \qquad (B-1)$$

where P_{Ai} is in mW. The subscripts have been defined in Section 2.3. With the switch in position 1, there is 26 db of attenuation between the HP oscillator and the spectrum analyzer. This corresponds to a power ratio of 2.5×10^{-3}. The analyzer deflection, D_A, depends on the power at the analyzer input which in turn depends on P_{Ai}. Thus, D_A may be related to P_{A1} by

$$D_A = 2.5 \times 10^{-3} P_{A1} \qquad (B-2)$$

With the switch in position 2, the HP oscillator is readjusted so that its output power, P_{A2}, causes the same analyzer deflection, D_A. This time though, the power leaving (P_{A2}) is dropped 5 db (0.316 ratio), part is reflected at the helix input (the power reflection coefficient is R_A), and is coupled to the analyzer by a 10 db (0.1 ratio) directional coupler. Therefore, D_A is related to P_{A2} by

$$D_A = P_{A2} (0.316) R_A (0.1) \qquad (B-3)$$

Eliminating D_A from Equations (B-2) and (B-3) and solving for R_A yields

$$R_A = 7.9 \times 10^{-2} \ (P_{A1}/P_{A2}) \qquad \text{(B-4)}$$

The transmission coefficient, T_A, is related to R_A by

$$T_A = 1 - R_A = 1 - 7.9 \times 10^{-2}(P_{A1}/P_{A2}) \qquad \text{(B-5)}$$

or, in terms of dbm_{A1},

$$T_A = 1 - 7.9 \times 10^{-2} \ \left[\text{antilog} \ (0.1 \ dbm_{A1})\right] / \left[\text{antilog} \ (0.1 \ dbm_{A2})\right] \quad \text{(B-6)}$$

Specifically

$$T_C = 1 - 7.9 \times 10^{-2} \ \left[\text{antilog} \ (0.1 \ dbm_{C1})\right] / \left[\text{antilog} \ (0.1 \ dbm_{C2})\right] \quad \text{(B-7)}$$

$$T_H = 1 - 7.9 \times 10^{-2} \ \left[\text{antilog} \ (0.1 \ dbm_{H1})\right] / \left[\text{antilog} \ (0.1 \ dbm_{H2})\right] \quad \text{(B-8)}$$

These expressions will be required for the calculation of amplifier gain.

The power gain of the helix, g_A, is the ratio of power out to power in and the db gain, G_A, is given by

$$G_A = 10 \log g_A \qquad \text{(B-9)}$$

With the switch in position 3, the HP oscillator is readjusted so that its output power, P_{A3}, causes the analyzer deflection D_A. In this case, the power leaving (P_{A3}) is dropped 5 db (0.316 ratio), is partially transmitted at the helix input (T_A), is increased by the helix gain, g_A, is dropped by 13 db (0.05 ratio) and causes the deflection, D_A. Thus, D_A is related to P_{A3} by

$$D_A = P_{A3} \ (0.316) \ T_A \ g_A \ (0.05) \qquad \text{(B-10)}$$

Eliminating D_A from Equations (B-2) and (B-10) and solving for g_A yields

$$g_A = (0.156) \ P_{A1}/(T_A P_{A3}) \qquad \text{(B-11)}$$

The amplifier gain (above cold loss) in the presence of oscillation, G_s (in db), is

$$G_A = G_H - G_C = 10 \log g_H - 10 \log g_C$$

$$= 10 \log (g_H/g_C)$$

$$= 10 \log (P_{H1}/T_H P_{H3})(T_C P_{C3})(T_C P_{C3}/P_{C1})$$

$$= (dbm_{C3} - dbm_{H3}) + (dbm_{H1} - dbm_{C1}) + 10 \log (T_C/T_H) \qquad \text{(B-12)}$$

where T_C and T_H are given by Equations (B-7) and B-8) respectively.

APPENDIX C

Derivation of the Harmonic Interference Correction Factor, G

Under the assumptions that the magnetic field and transverse electric fields are negligibly small at the perturbation, the frequency shift, $\Delta f_r'$, due to the perturbation may be given by

$$\Delta f_r' = C_1 E_z(y) E_z(y)^* \tag{C-1}$$

where C_1 is a proportionality constant and y is the distance from the structure (the origin) to the perturbation. Strictly speaking, the equation should appear as an integral over the perturbation but we assume the perturbation is small and that $E_z(y)$ represents an average value over the perturbation. $E_z(y)$ is the sum of the space harmonics, that is,

$$E_z(y) = \sum_{m=-\infty}^{\infty} E_{zm}(y) \tag{C-2}$$

so that Equation (C-1) may be written

$$\Delta f_r' = C_1 \left[\sum_{m=-\infty}^{\infty} E_{zm}(y) \right] \left[\sum_{m=-\infty}^{\infty} E_{zm}(y)^* \right] \tag{C-3}$$

The space harmonic fields are, of course, orthogonal over the whole volume of the slow-wave structure resonator but it can be shown[20] that under the conditions for which the simple perturbation theory is valid, the fields may be taken as orthogonal over the volume of the perturbation. Therefore, Equation (C-3) may be written as

$$\Delta f_r' = C_1 \sum_{m=-\infty}^{\infty} E_{zm}(y) \, E_{zm}(y)^* \tag{C-4}$$

We now assume that there are only two space harmonics of sufficient strength to perturb the frequency; the fundamental, $m = 0$, and one other, $m = n$. Therefore

$$\Delta f_r' = C_1 E_{zo}(y) E_{zo}(y)^* + C_1 E_{zn}(y) E_{zn}(y)^*$$

$$= C_1 E_{zo}(y) E_{zo}(y)^* \left[1 + E_{zn}(y) E_{zn}(y)^* / E_{zo}(y) E_{zo}(y)^* \right] \quad \text{(C-5)}$$

But $C_1 E_{zo}(y) E_{zo}(y)^*$ is just the Δf_r of Equation (3-10), therefore G is given by

$$G = 1 + E_{zn}(y) E_{zn}(y)^* / E_{zo}(y) E_{zo}(y)^* \quad \text{(C-6)}$$

We define $F_n(y)$ as the ratio $E_{zn}(y)/E_{zn}(0)$ and $S_{o,n}$ as the ratio $E_{zn}(0)/E_{zo}(0)$ where $y = 0$ implies the value at the structure. Thus Equation (C-6) may be written as

$$G = 1 + \left[S_{o,n} F_n(y) / F_o(y) \right]^2 \quad \text{(C-7)}$$

$S_{o,n}$, $F_o(y)$, and $F_n(y)$ usually are easily obtainable from the theory of the structure so evaluation of this correction factor is quite straightforward. For example, for the meander line, with or without ridge loading, the amplitude of the nth harmonic at the bars is given by

$$E_{zn}(0) = C_2(\theta + n\pi)^{-1} \cos(\theta/2) \sin \left[(\theta + n\pi)/4 \right] \cos(n\pi/2)$$

where C_2 is a constant. Thus

$$S_{o,n} = \theta \sin \left[(\theta + n\pi)/4 \right] \cos n\pi/2 \left[(\theta + n\pi) \sin (\theta/4) \right]^{-1} \quad \text{(C-8)}$$

Through Pierce's impedance equation, Equation (3-2), we see that

$$F_n^2(y) = E_{zn}(y)E_{zn}(y)^*/E_{zn}(0)E_{zn}(0)^*$$

$$= K_n(y)/K_n(0) \qquad\qquad (C-9)$$

and thus $F_n^2(y)$ is a spatial impedance transformation factor for the nth space harmonic. The factor $F_n^2(y)$ is discussed more fully in Appendix D.

APPENDIX D

Impedance Transformation Factors

The impedance transformation factor, $F_n^2(y)$, was defined in Appendix C by the relation

$$F_n(y) = E_{zn}(y)/E_{zn}(0) \tag{D-1}$$

where y is the distance measured from the structure. Thus, if we know the transverse variation of the fields, we can evaluate $F_n^2(y)$.

For a plane structure (e.g., a planar meander line) with no side walls, or with very distant side walls, E_{zn} varies as $\exp(-\beta_n y)$; therefore

$$F_n(y) = \exp(-\beta_n y); \quad n = 0, \pm 1, \pm 2, \ldots \tag{D-2}$$

where

$$\beta_n = \beta_o + n\pi/p$$

and p is the bar pitch (see Figure 25). For a full cylindrical structure (e.g., a Type I, II, or III structure) with an axial perturbation, $F(y)$ $F(a)$ for $b \ll a$ where a is the structure radius and b is the perturbing dielectric radius,

$$F_n(y) \longrightarrow 1/I_o(\alpha_n a) \tag{D-3}$$

where

$$\alpha_n^2 = \beta_n^2 - k_o^2 = \beta_n^2 - (\omega/c)^2$$

For a half cylindrical structure (e.g., a Type IV structure), it is reasonable to assume that the fields at the center relative to those at the bars are half what they would be for a full cylindrical structure. Therefore, for this structure,

$$F_n(y) \longrightarrow 1/2I_o(\alpha_n a) \qquad \text{(D-4)}$$

Not only does the value of $F_n(y)$ allow the calculation of G, but if the impedance is known at one point, then, from Equation (C-9), the impedance can be calculated anywhere. If the impedance at y_1 is known to be $K_n(y_1)$, then the impedance at y_2, $K_n(y_2)$ may be determined by writing Equation (C-9) as

$$F_n^2(y_2) = K_n(y_2)/K_n(0)$$

and

$$F_n^2(y_1) = K_n(y_1)/K_n(0)$$

Eliminating $K_n(0)$ and solving for $K_n(y_2)$ yields

$$K_n(y_2) = K_n(y_1) \left[F_n^2(y_2)/F_n^2(y_1) \right] \qquad \text{(D-5)}$$

In most cases the impedance at the center, $K_n(a)$, has been measured and we wish to calculate the impedance at the circuit, $K_n(0)$, (or vice versa). This may be obtained directly from Equation (C-9) as

$$K_n(0) = K_n(a)/F_n^2(a) \qquad \text{(D-6)}$$

A second conversion factor which is required is one which allows conversion from one space harmonic impedance to another, that is, given $K_n(y)$, find $K_m(y)$. Substituting Pierce's impedance equation

Equation (3-2), into the identity

$$K_m(y) = K_n(y) \left[K_m(y)/K_n(y) \right] \qquad \text{(D-7)}$$

yields

$$K_m(y) = K_n(y) \left[E_m(y)/E_n(y) \right]^2 / (\beta_m/\beta_n)^2 \qquad \text{(D-8)}$$

Now

$$E_m(y)/E_n(y) = \left[E_m(0)/E_n(0) \right] \left[E_m(y)/E_m(0) \right] \left[E_n(0)/E_n(y) \right]$$

$$= S_{n,m} \, F_m(y)/F_n(y) \qquad \text{(D-9)}$$

and

$$\beta_m/\beta_n = (\beta_o + m\pi/p)/(\beta_o + n\pi/p)$$

$$= (\theta + m\pi)/(\theta + n\pi) \qquad \text{(D-10)}$$

where θ, the phase shift per bar, is given by

$$\theta = \beta_o p$$

Therefore, Equation (D-8) may be written as

$$K_m(y) = K_n(y) \, S_{n,m}^2 \left[F_m(y)/F_n(y) \right]^2 (\theta + n\pi)^2/(\theta + m\pi)^2 \qquad \text{(D-11)}$$

For the structures in this report, we are interested in the -2 space harmonic impedance whereas we have measured the fundamental impedance. For these cases,

$$K_{-2}(y) = K_o(y) S_{o,-2}^2 \left[F_{-2}(y)/F_o(y) \right]^2 \theta^2/(\theta - 2\pi)^2 \qquad \text{(D-12)}$$

where $F_o(y)$ and $F_{-2}(y)$ are given by either Equation (D-3) or (D-4).

For a space harmonic transformation made at the structure, $y = 0$, $F_n(0) = 1$. Substituting Equation (3-14) for $S_{0,-2}$ and rearranging in terms of the variable θ/π yields

$$K_{-2}(0) = K_0(0) \; (\theta/\pi)^4 \; \cot^2\left[(\pi/4)(\theta/\pi)\right] \; / \; \left[(\theta/\pi)-2\right]^4 \qquad \text{(D-13)}$$

APPENDIX E

Derivation of the Space Charge Waves and

the Solution of DeGrasse's Equations for the DCC

The space charge waves for the DCC are obtained by solving the two coupled equations, Equations (A-1) and (A-3), for both helices. The first helix (amplifier) acts like an ordinary BWA so that at the end of the helix there is a slow space charge wave with a certain amplitude propagating on the beam with the frequency f_s. This wave propagates unchanged to the second (oscillator) helix. This space charge wave then induces a circuit wave on the second helix, and interacts with it along the helix. (The interaction will only be appreciable for small f_d/f_o.) The difference between the model used to describe the SCC and that used to describe the DCC is in the boundary conditions for the space charge and circuit waves at the frequency f_s for the oscillator helix. For the SCC the boundary conditions are (Appendix A),

$$A_{qs}(0) = 0 , \quad \left| A_{cs}(L) \right|^2 = P_s$$

and for the DCC, they are,

$$\left| B_{qs}(0) \right| = \left| B_{qs}(L_1) \right| , \quad B_{cs}(L_2) = 0$$

where $B_{qs}(L_1)$ is the slow space charge wave at frequency f_s at the end (L_1) of the amplifying helix.

The expression for B_{qs} is the same as given in Appendix A for A_{qs} under the assumption that QC is large. Solving the two coupled equations under the second pair of boundary conditions, the slow space charge wave at f_o is obtained as

$$B_{qo} = j2D_1 \exp(-j\beta_{qo}z) \sin(d^o_{cq}z) \qquad (E-1)$$

and at f_s as

$$B_{qs} = B_1 \left\{ \exp(jt_1z) \right.$$

$$- \left[(t_1 + \beta_{qs})/(t_2 + \beta_{qs}) \right] \exp\left[j(t_1 - t_2)L_2 \right] \exp(jt_2z) \qquad (E-2)$$

where

$$|B_1| = |A_{qs}(L_1)| \left\{ 1 - \left[(t_1 + \beta_{qs})/(t_2 + \beta_{qs}) \right] \exp j(t_1 - t_2)L_2 \right\}^{-1}$$

and

$$t_{1,2} = -(1/2)(\beta_{qs} + \beta_{cs}) \pm \sqrt{\left[(1/2)(\beta_{qs} - \beta_{cs}) \right]^2 + (d^s_{cq})^2}$$

All the parameters in these expressions, except L_1, refer to the second (oscillator) helix.

Substituting Equations (E-1) and (E-2) into Equations (2-1) through (2-6) (and changing A to B), and solving Equations (2-1) and (2-2) subject to the boundary conditions

$$i_d(0) = v_d(0) = 0$$

where $z = 0$ is the entrance to the second helix, an expression for the difference frequency current similar to Equation (A-16) is found as

$$i_{d2} = \sqrt{CI_o/V_o} \, |B_{qs}(L_1)| \, H_2 \qquad (E-3)$$

where $B_{qs}(L_1)$ is the amplitude of the slow space charge wave at the end of the first helix,

$$H_2 = M/(4 \sqrt{k_o k_s}) \sum_{i=1}^{4} \left\{ -(1/2)\left[\beta_i' - (\omega_d/\omega_{qd})\delta_i'\right] \exp\left[j(\omega_{qd}/U_o)z\right] \right.$$

$$- (1/2)\left[\beta_i' + (\omega_d/\omega_{qd})\delta_i'\right] \exp\left[-j(\omega_{qd}/U_o)z\right] + \beta_i' \exp(j\xi_i z) \Bigg\} \qquad (E-4)$$

$$\beta_i' = (f_d/f_o) \left[(k_o + k_s - 3)(\xi_i \alpha_i/\beta_{eo}) + (f_d/f_o)\alpha_i \right] / (\xi_i^2/\beta_{eo}^2 + \omega_{qd}^2/\omega_o^2)$$

$$\delta_i' = (\omega_{qd}/\omega_o)^2 \left[(k_o + k_s - 3)\alpha_i + (f_d/f_o)(\alpha_i\beta_{eo}/\xi_i)\right] / (-\xi_i^2/\beta_{eo}^2 + \omega_{qd}^2/\omega_o^2)$$

$$+ \alpha_i \left[1 - (f_d/f_o)(\beta_{eo}/\xi_i)\right]$$

$$M = \left\{ 1 - \left[(t_1 + \beta_{qs})/(t_2 + \beta_{qs})\right] \exp\left[j(t_1 - t_2)L_2\right] \right\}^{-1}$$

$$\alpha_1 = 1 \; , \quad \alpha_2 = -1 \; , \quad \alpha_3 = -\alpha_4$$

$$\alpha_4 = \left[(t_1 + \beta_{qs})/(t_2 + \beta_{qs})\right] \exp\left[-j(t_1 - t_2)L_2\right]$$

and

$$\xi_1 = d_{cq}^s - t_1 - \beta_{qs} \; , \quad \xi_3 = d_{cq}^s - t_2 - \beta_{qs}$$

$$\xi_2 = -d_{cq}^s - t_1 - \beta_{qs} \; , \quad \xi_4 = -d_{cq}^s - t_2 - \beta_{qs}$$